UNIVERSIDADE DE SÃO PAULO
Escola de Engenharia de São Carlos

Force control benchmarking of hydraulic and electrical actuation systems applied to robotics

Elisa Gamper Vergamini

EESC · USP

UNIVERSITY OF SÃO PAULO
SÃO CARLOS SCHOOL OF ENGINEERING

Elisa Gamper Vergamini

Force control benchmarking of hydraulic and electrical actuation systems applied to robotics

São Carlos

2023

Elisa Gamper Vergamini

Force control benchmarking of hydraulic and electrical actuation systems applied to robotics

Dissertation presented to the São Carlos School of Engineering of the University of São Paulo, for obtaining the title of Master of Science - Graduate Program in Mechanical Engineering.

Area of concentration: Dynamics and Mechatronics

Advisor: Prof. Dr. Thiago Boaventura Cunha
Coadvisor: Prof. Dr. Daniel Varela Magalhães

Corrected Version

This research is supported by the grants 2021/03373-9 and 2022/09306-4, São Paulo Research Foundation (FAPESP). The opinions, assumptions and conclusions or recommendations expressed in this material are those of the author and do not necessarily reflect the views of FAPESP.

São Carlos

2023

Vergamini, Elisa Gamper
V493f Force control benchmarking of hydraulic and electrical actuation systems applied to robotics / Elisa Gamper Vergamini; advisor Thiago Boaventura Cunha. São Carlos, 2023.
144 p. : il. ; 30 cm.

Dissertation (Master's) - Graduate Program in Mechanical Engineering and Area of Concentration in Dynamics and Mechatronics – São Carlos School of Engineering, University of São Paulo, 2023.

1. Force control. 2. Electric and hydraulic actuators. 3. Robotics. 4. Benchmarking. 5. Physical Interaction. I. Force control benchmarking of hydraulic and electrical actuation systems applied to robotics .

FOLHA DE JULGAMENTO

Candidata: Bacharela **ELISA GAMPER VERGAMINI**.

Título da dissertação: "Comparação de controle de força de sistemas de atuação hidráulicos e elétricos aplicados à robótica".

Data da defesa: 22/02/2024.

Comissão Julgadora	**Resultado**
Prof. Dr. Thiago Boaventura Cunha (Orientador) (Escola de Engenharia de São Carlos/EESC/USP)	Aprovada
Prof. Dr. Andrea Calanca (Università Degli Studi di Verona)	Aprovada
Prof. Tit. Marco Henrique Terra (Escola de Engenharia de São Carlos/EESC/USP)	Aprovada

Coordenador do Programa de Pós-Graduação em Engenharia Mecânica:
Prof. Associado **Adriano Almeida Gonçalves Siqueira**

Presidente da Comissão de Pós-Graduação:
Prof. Titular **Carlos De Marqui Junior**

This work is dedicated to my nephews Lara and Hugo, you're my beacon of joy, love and hope.

ACKNOWLEDGEMENTS

First of all, I would like to thank my family for being my base, my inexhaustible source of love and strength. Vovó, Mama, Papa, Fer, Dani, Bu, Giu, Curu and Pingo. Tio Diniz, Tia Silvia, Tata Tete, Victor, my cousins and forever partners, Maria Paula and Tucky, my Papy, I know that a lot of you lives in me. And also to Tia Mara, Lucas, Jana and Daniel. I love you all more than I will ever be able to explain.

To my forever friends Flora, Gabi, Carol, Marcela and Mama, may we always continue with our love as sisters.

To my advisor Professor Thiago Boaventura, for all his patience and willingness to help me, for always advising me, being an example, guiding me and encouraging me to be the best version of myself.

To my colleagues and friends at LegRo and Altair, researchers and professors with whom I had the honor of sharing knowledge and inspiring company, especially Maurício, Leonardo and Cícero.

To Equitron Automação Eletrônico Mecânica Ltda for the consultancy, especially to Prof. Dr. Eng. José Guilherme Sabe.

To the São Paulo State Research Support Foundation (FAPESP), for believing in my potential and for financing my research.

To the University of São Paulo (USP) and the São Carlos School of Engineering (EESC), for providing me with a high level of training during my master's degree.

"I'm no longer accepting the things I cannot change,
I'm changing the things I cannot accept."
Angela Davis

ABSTRACT

VERGAMINI, E. G. **Force control benchmarking of hydraulic and electrical actuation systems applied to robotics**. 2023. 144p. Dissertation (Master's) - São Carlos School of Engineering, University of São Paulo, São Carlos, 2023.

Designers have faced difficulties when it comes to the interaction between robots and humans in dynamic environments. Managing the events in such scenarios involves controlling the force and velocity of the robots. There are two approaches to achieve this: controlling only the force or indirectly controlling the relationship between force and velocity through impedance. In addition to these factors, researchers have also investigated controllers for collaborative robots, legged robots and exoskeletons. This has posed a challenge for designers in determining the appropriate drive system to use. To address this issue, it is beneficial to provide a comprehensive comparison of controller-actuator combinations, which can serve as a guide for selecting the most suitable elements based on the specific application. Hence, the objective of this master's project is to systematically compare the stability and performance of force controllers in electric and hydraulic actuators. In order to achieve this goal, an experimental setup was designed, constructed and validated, along with the development of a benchmarking methodology that includes a range of metrics to assess performance, passivity, and stability. The methodology is applicable to all types of actuators and force controllers. Its approach enables the calculation of metrics regardless of loads or environments. It was implemented on three distinct actuation systems: a DC motor, a linear electric motor (PMLSM), and a hydraulic actuator (servo valve and cylinder). Various controllers, including different variations of PIDs, load velocity compensation, and disturbance observers (DOB), were tested for each actuator. The metrics obtained from the tests provided insights into the influence of different control architectures on the performance and stability of the actuators. For instance, it was observed that the derivative gain negatively affected the linear electric motor, while load velocity compensations showed more enhancements for hydraulic actuators. Moreover, linear controllers like PID exhibited poorer performance in systems with higher levels of non-linearities, such as hydraulic systems. There are both advantages and disadvantages to using the systems identified in the methodology. On the positive side, these transfer functions allow for the inclusion of metrics that can provide a more comprehensive evaluation of the system stability. However, it is important to note that these metrics can be influenced by external variables such as friction and uncertainties in the experimental data used on the identification process. Additionally, the use of this method enabled faster calculation of metrics and the capture of the most important information regarding force control in the studied cases.

Keywords: Force Control; Physical Interaction, Benchmarking, Electric and hydraulic actuators.

RESUMO

VERGAMINI, E. G. **Comparação de controle de força de sistemas de atuação hidráulicos e elétricos aplicados à robótica**. 2023. 144p. Dissertação (Mestrado) - Escola de Engenharia de São Carlos, Universidade de São Paulo, São Carlos, 2023.

A interação entre robôs e humanos em ambientes dinâmicos tem sido desafiadora para os projetistas.O controle desses eventos é feito a partir do controle da grandezas envolvidas, força e velocidade. Para tal, pode-se escolher controlar apenas a força ou, de maneira indireta, controlar a relação entre as duas variáveis a partir da impedância. Junto a esses aspectos, controladores vêm sendo estudados para robôs colaborativos, robôs com pernas e exoesqueletos, fazendo com que projetistas tenham dificuldade quanto a qual sistema de acionamento utilizar. Neste contexto, é conveniente oferecer uma comparação sistemática dos conjuntos controladores-atuadores, de modo a disponibilizar um guia que permita adequar a seleção desses elementos conforme a aplicação. Assim, o presente projeto de mestrado tem como objetivo realizar uma comparação sistemática em estabilidade e desempenho de controladores de força em atuadores elétricos e hidráulicos. Para atingir este objetivo, foi criada, construída e validada uma bancada experimental, junto com o desenvolvimento de uma metodologia de *benchmarking* que inclui uma série de métricas para avaliar desempenho, passividade e estabilidade dos sistemas desejados. A metodologia é aplicável a todos os tipos de atuadores e controladores. Sua abordagem permite o cálculo de métricas independente de cargas/ambientes. Ela foi implementada em três sistemas de atuação distintos: um motor DC, um motor elétrico linear (PMLSM) e um atuador hidráulico (servoválvula e cilindro). Vários controladores, incluindo diferentes variações de PIDs, compensação de velocidade de carga e observadores de disturbios (DOB), foram testados para cada atuador. As métricas obtidas nos testes forneceram percepções sobre a influência de diferentes arquiteturas de controle no desempenho e estabilidade dos atuadores. Por exemplo, observou-se que o ganho derivativo afetou negativamente o motor elétrico linear, enquanto as compensações de velocidade de carga apresentaram mais melhorias para atuadores hidráulicos. Além disso, controladores lineares como o PID apresentaram desempenho inferior em sistemas com níveis mais elevados de não linearidades, como sistemas hidráulicos. Existem vantagens e desvantagens na utilização dos sistemas identificados na metodologia. Do lado positivo, estas funções de transferência permitem a inclusão de métricas que podem fornecer uma avaliação mais abrangente da estabilidade do sistema. Porém, é importante notar que essas métricas podem ser influenciadas por variáveis externas como atrito e incertezas nos dados experimentais usados nas identificações. Além disso, a utilização deste método possibilitou o cálculo mais rápido das métricas e a captura de informações importantes sobre o controle de força nos casos estudados.

Palavras-chave: Controle de força; Interação física; *Benchmarking*;Atuadores elétricos e hidráulicos.

LIST OF FIGURES

LIST OF TABLES

LIST OF ABBREVIATIONS AND ACRONYMS

IC2D	Impedance Control 2 Dimensions
FC2D	Force Control 2 Dimensions
BEPE	Bolsa de Estágio de Pesquisa no Exterior
FAPESP	Fundação de Amparo à Pesquisa do Estado de São Paulo
RTOS	Real Time Operating System
DMA	Direct Memory Access
DoF	Degrees od Freedom
SEA	Series Elastic Actuator
CAD	Computer Aided Design
HPU	Hydraulic Power Unit
BSP	British Standard Pipe
DCV	Directional Control Valve
LED	Light Emitting Diode
ADC	Analog-to-Digital Converters
PID	Proportional–Integral–Derivative control
DC	Direct Current
PMLSM	Permanent Magnet Linear Synchronous Motor
VC	Velocity Compensation
DOB	Disturbance Observer Based control
LPF	Low Pass Filter
MISO	Multiple Input Single Output
SISO	Single Input Single Output
RMSE	Root Mean-Square Error

LIST OF SYMBOLS

α	Ratio factor between piston areas
A_p	Piston area
$A_{e\oslash}$	Equivalent piston area at operating point
B	Viscous friction coefficient
B_l	Load damping
β	Bulk modulus
β_e	Effective Bulk modulus
C	Capacitance
C_d	Discharge coefficient
D_p	Piston diameter
D_r	Rod diameter
D_v	Valve spool damping
$\Delta_{pn1}, \Delta_{pn2}$	Nominal pressure drop across one control edge
f	Load force
f_h	Hydraulic force
f_d	Driving force
f_i, F_i	Interaction force
f_r, f_{ref}, F_r	Reference force
f_{ext}	External force
F_e	Electromagnetic force
F_Ω	Lumped uncertainties
f_c	Cutoff frequency
f_{max}	Highest peak force
f_s	Steady-state force value

F_t	Transparency
F_{tr}	Reference transparency
i_q	Current on the q axis
J_m	Rotor inertia
J_l	Load inertia
K_p	Proportional gain
K_i	Integrative gain
K_d	Derivative gain
K_t	Transmission stiffness
k_m	Motor opposite force constant
k_t	Motor force constant
K_{VC}	Velocity compensation gain
K_μ	Friction gain
K_v	Valve gain
K_{qe}	Equivalent flow gain
k_l	Loas stiffness
κ_B	Backdrivability gain
l_{cyl}	Cylinder stroke
m	Mass
m_p	Piston mass
M_l	Load mass
N_d	Derivative filter coefficient
o_s	Overshoot
p	Pressure
p_a	Cylinder chamber a pressure
p_b	Cylinder chamber b pressure

p_s	Supply (pump) pressure
p_t	Tank pressure
P_a	Actuator dynamics
P_b	Passivity index at frequency bandwidth
q_n	Valve nominal flow
q_a	Cylinder chamber a flow
q_a	Cylinder chamber b flow
q_{ex}	Additional desired flow
$R_{1,2,3,4,5}$	Electrical resistance
R_k	Correlation coefficient
R_m	Motor electric resistance
R_H	Passivity index
T	COupled transfer function
T_t	Blocked system Tr
T_i	Apparent impedance transfer function
t_s	Settling time
t_r	Rising time
τ_{dis}	Disturbance external inputs
τ_r	Reference torque
τ_s	Load torque
τ_m	Motor torque
U	Voltage
U_{in}	Input voltage
U_{out}	Output voltage
u_n	Valve nominal input
u_v	Valve spool position

u	Input
u_{PID}	PID control signal
u_{VC}	VC control signal
u_{DOB}	DOB control signal
v_0	Confined fluid volume
v_a	Cylinder chamber a volume
v_b	Cylinder chamber b volume
v	Volume
v_i	Interaction velocity
v_{act}	Actuator velocity
v_{pl}	Pipeline volume
x	Position
x_p	Piston position
x_l	Load position
$\dot{x_{vs}}$	Velocity source velocity
ξ	Noise external inputs
Y_a, y_a	Actuator addmitance
Y_l, y_l	Load addmitance
y	Output
ω_v	Valve frequency
ω_B	Bandwidth frequency
W	Area gradient
Z_t, z_t	Transmission impedance

CONTENTS

1 INTRODUCTION

Robots are now being used in situations where the conditions are unpredictable and changing over time, such as when they are collaborating with humans or in other contexts. Controlling the physical interaction between multiple agents is a common requirement and a difficult task for a range of robots, such as collaborative manipulators, legged robots, and wearable robots. The amount of power exchanged between two bodies during contact can be used to measure the physical interaction between them. The power of this mechanical system is determined by two factors: the force and the speed of the interaction port (HOGAN, 1984).

As illustrated in Figure 1, there are several approaches to control physical interaction (CALANCA; MURADORE; FIORINI, 2015). This type of control can be divided into two main categories: active and passive. In an active interaction, compliance is only caused by control, whereas in a passive interaction it is only a consequence of mechanics. Active control can be divided into two subcategories: direct and indirect force control. Direct force control algorithms are those that control the force and position subspaces separately, called hybrid position-force control (RAIBERT; CRAIG, 1981). It is essential to note that, as Duffy has noted, the foundation of hybrid controls is flawed, as the correct outcomes achieved are only due to the simplicity or symmetry of the problems being examined (DUFFY, 1990). Indirect force control involves regulating the relation between force and velocity by incorporating impedance and admittance controls. This approach is effective when the robot is in an open space and when it interacts with its environment/load, making it suitable for use even in unfamiliar surroundings (HOGAN; BUERGER, 2018).

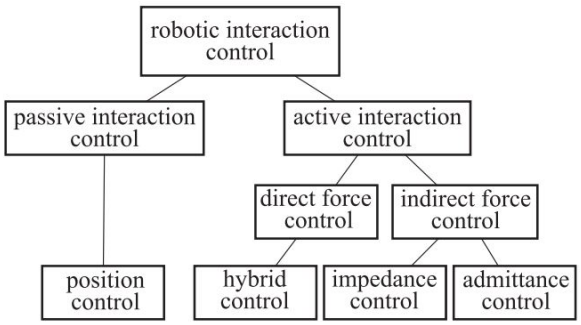

Figure 1 – Interaction control classification as proposed in (CALANCA; MURADORE; FIORINI, 2015).

The physical environment in which a robot operates can be divided as well into two categories: active and passive, depending on whether or not there is an exchange of mechanical power between the robot and the environment. Active environments involve an exchange of mechanical power between the robot and its surroundings, while passive

environments do not. It is imperative to comprehend the ideas of impedance and admittance to comprehend how robots interact with their environment.

Mechanical impedance is the dynamic relation between velocity as input and force as output, admittance is the inverse relation (HOGAN; BUERGER, 2018). It is a type of unified control best suited to handle mechanical interaction tasks in specific cases of physical interaction. The main objective of impedance control is, by controlling this relation, to guarantee the requirements for a specific manipulation task in which both the position of the robot end effector and the forces of these interactions are maintained within tolerances that guarantee the safety of the operation. Precisely because it is able to control the relationship between both magnitudes, the impedance control stands out, being able to offer better performance for various robots and safer robot-human interaction.

As said previously. impedance control aims to shape the dynamic relationship between external forces in the system interaction with an environment and the velocity or position of the actuator. The impedance control can be implemented using an inner force loop and an outer position loop, or if interchanged, i.e., an inner position loop and an outer force loop we have the so-called admittance control. In both architectures, the inner loop must be fast enough to have negligible dynamics while the desired impedance/admittance is implemented in the outer loop.

The impedance and admittance framework has a particularly prominent issue called coupled stability. When two systems are combined, they may become unstable. Nevertheless, if both systems are passive, it is enough to guarantee the stability of the combination (COLGATE; HOGAN, 1989). Since Colgate and Hogan work, the theory has been significantly advanced, even to encompass nonlinear systems (SCHAFT, 2016). Safonov demonstrated a broadening of the passivity theory, wherein the passivity condition was demonstrated to be a particular instance of a sector-separation condition (SAFONOV, 1980). Academic papers that employ sector-separation theorems are being published regularly (XIA et al., 2020; HUANG; HUANG, 2020). Additionally, passivity-based techniques based on this theorem are still being utilized in interaction controllers, particularly in the robotics domain (CALANCA; MURADORE; FIORINI, 2017; HIGA et al., 2019).

A common belief in the literature and in rigid body simulators is that "low-level" robot joint controllers have ideal force sources, meaning that the applied and desired forces at the robot joint are perfectly aligned. This assumption is the basis of several proposed impedance/admittance controllers that include an inner force control loop (KIM; KWON, et al., 2018; RHEE et al., 2023; OTT; MUKHERJEE; NAKAMURA, 2015). Designing a force controller that accurately replicates the desired behavior, especially in the highly dynamic contexts that are common in robotics, is not an easy task (BOAVENTURA; FOCCHI, et al., 2012). Therefore, it is essential to thoroughly assess the performance and stability of these inner-loop controllers.

The interaction force is also dependent on the dynamics of the load (which is not the case for position/velocity control due to zero-pole cancellation). It is often observed that a stable force controller can suffer a significant decrease in performance or even become unstable when connected to a certain environment (KURFESS, 2018). The load characteristics have a major influence on the usual performance and stability metrics, such as overshoot, settling time, bandwidth, phase, and gain margin, as well as static and dynamic error. Therefore, it is imperative to be able to evaluate the effectiveness of various controllers associated with different actuators in force control.

1.1 Motivation

In recent years, hydraulic actuated systems have become increasingly prominent in the field of robotics, particularly in legged robots such as bipeds (ATLAS, SARCOS (ATKESON et al., 2000), KenKen (HYON; EMURA; MITA, 2003)) and quadrupeds (HyQ (SEMINI; TSAGARAKIS; GUGLIELMINO, et al., 2011b), Titan XI (HODOSHIMA et al., 2007), Jinpoong (KIM; CHO; PARK, et al., 2013), SCALF (RONG et al., 2012)). Two of the most renowned hydraulic legged robots of nowadays are the updated version of Boston Dynamics' humanoid robot ATLAS, which can do somersaults and parkour maneuvers, and the IIT's quadruped robot HyQReal with highly integrated miniature hydraulics that can pull a small passenger plane (SEMINI; BARASUOL, et al., 2019), both of them are shown in Figure 2.

(a) HyQReal (b) Atlas

Figure 2 – Two of today's leading legged robots with hydraulic actuators.

Although electric actuators have made great strides over the past few decades (CAO et al., 2011), hydraulic actuators have some properties that make them attractive to applications in robotic systems. First of all, they have higher power to weight ratios, so they can meet the needs of power and speed with smaller and lighter devices, and they can achieve it without the need for additional mechanical transmission (SEOK et al.,

2012).The low compressibility of fluids makes hydraulic actuators highly efficient in terms of closed-loop gains, providing stability margins that result in improved accuracy when following references and rejecting disturbances (CLARK, 1969). Generally, robots have a strong and straightforward mechanical design that allows them to be resistant to shock and excessive loads. This feature is essential for robots with legs, as it is not possible to prevent force peaks from occurring in the robot's structure. Electric actuators typically operate at high speeds, necessitating the use of reduction gears to increase power at lower speeds. However, these gears can be a source of friction and other non-linearities, and are not always able to withstand impact forces. A way found to deal with such limitations have been to introduce springs in the transmission to filter impacts and protect the motor and gears (PRATT; WILLIAMSON, 1995), also reducing the system's bandwidth.

Despite these disadvantages, electric actuators are still widely applied because they are controlled in simpler formats than hydraulic actuators, in general. Evidence of the prevalence of electric quadruped robots is seen in the abundance of them available for purchase, including Solo (GRIMMINGER et al., 2020), Go1 from Unitree Robotics, ANYmal robot (HUTTER et al., 2016), and Spot the quadruped developed also by Boston Dynamics, all of them can be seen in Figure 3.

(a) Anymal (b) Solo (c) Go1 (d) Spot

Figure 3 – Four of today's leading legged robots with electric actuators.

When it comes to robots such as manipulators, quadrupeds, and bipeds, the chosen actuators act as the robot's "muscles". This means that when a new robot is created, the selection of actuators is a crucial step to ensure that power, inertia, and task-related requirements are met. Nevertheless, as is typical during this selection, there is a compromise that must be taken into account. The characterization of practical effects aspects on the force controllers performance and stability would therefore help mechanical and control designers to correctly select the more adequate actuation system and control architecture.

1.2 Objectives

Often the designer of a robot is in doubt about which actuation system to use. Therefore, a systematic comparison with force controllers on electric and hydraulic actuators will be made in this master's project, thus allowing a critical analysis of which system

of action would be more appropriate in a given situation or task that involves physical interaction.

The main objective of this master project is a systematic comparison in terms of the stability and performance of force controllers with electric and hydraulic actuators. As this master project is part of the Young Researcher project, many tasks are performed as a team. Therefore, the objectives can be summarized as follows:

- Design, manufacturing, assembly, and validation of the IC2D test bench.
- Develop a methodology and a set of metrics to quantify the performance of force controlled systems;
- Apply the methodology at the joint level to electric and hydraulic actuation systems and compare them.

1.3 Dissertation outline

In order to contemplate the defined objectives in a complete and fluid way, this dissertation is divided into six Chapters and an Appendix.

Chapter 1 provides a concise introduction to the subject, providing the necessary context to comprehend the various aspects of work motivation. Chapter 2 presents a review of benchmarking methodologies, discussing their advantages and limitations. In Chapter 3, a detailed description of the experimental framework is provided, including its design, assembly, and application in the methodology. Chapter 4 focuses on the theoretical review of the dynamic models of the actuation systems and force controllers used in this study. The stages of the benchmarking methodology employed in this work are described in Chapter 5. Chapter 6 presents the main findings and discusses the most influential aspects, while Chapter 7 closes the dissertation by presenting the main conclusions drawn from the research and suggesting future directions. Appendix A contains additional information to enhance understanding of the methodology presented.

2 STATE OF THE ART REVIEW

To effectively evaluate force controllers, it is crucial to develop a methodology and metrics that facilitate the comparison of these controllers across different configurations and representative actuators. Impedance and admittance controllers incorporate the force controller, making it necessary to establish a methodology and metrics for evaluating its performance. This approach ensures a logical, functional, and straightforward validation process. Despite various research studies proposing methodologies and metrics, there is currently no universally accepted approach for different force controllers and actuators.

There are many existing methods for benchmarking force/torque controllers, but they often have a narrow focus. Some of these methods specifically look at end-effector force control in manipulators, which means that they also consider factors such as link kinematics and flexibility, in addition to controlling actuator torque (BEHRENS et al., 2018; FALCO et al., 2016; BRUHM; CZINKI; LOTZ, 2015).

In their work, Behrens et al. suggested a straightforward implementation that does not require any prior understanding of the system's dynamics and control architecture. They focus on evaluating the system's ability to reject disturbances. However, they do not evaluate the tracking performance of the system, lack a stability metric, and do not consider the dynamics of the environment (BEHRENS et al., 2018). Falco et al. do not assume any prior understanding of the system dynamics and control architecture. Instead, they evaluate the tracking performance in terms of disturbance rejection using standard performance indicators in the time domain. However, they do not consider the dynamics of the environment and do not propose a stability metric. Overall, their methodology is quite complex and mainly aimed at robotic manipulators (FALCO et al., 2016). In their study, Bruhm, Czinki and Lotz assess the tracking performance and disturbance rejection capabilities, taking into account the sensor's characteristics such as range and resolution. They also introduce metrics that consider the dynamic behavior of the system, including bandwidth, force sensitivity, and spectral attenuation. However, the stability metric and the influence of environmental dynamics have not been taken into account in their analysis (BRUHM; CZINKI; LOTZ, 2015).

Certain researchers restrict their investigation to specific loading conditions, typically referred to as blocked (UGURLU et al., 2022). This approach offers a limited viewpoint of controller performance and stability because the characteristics of the connected load, such as its mass, damping, and stiffness, directly impact these parameters. Some other approaches treat the load as an unknown factor and utilize robust control techniques (NIKSEFAT; SEPEHRI, 2001). Nevertheless, these benchmarks typically assume that load fluctuations are only parametric, which restricts their wider usefulness.

The analysis of force control performance is distinct from regular control analysis due to the significant influence of the environment on the controller's performance (EPPINGER; SEERING, 1987; ALLEYNE; LIU, 1999). Some comprehensive strategies have been developed that suggest techniques to simulate different load conditions and employ statistical evaluation metrics (VICARIO et al., 2021a). In a similar vein, Vicario et al. assessed tracking performance and indirectly considered disturbance rejection by taking into account environmental dynamics. However, it lacks a stability metric and necessitates numerous diverse environments for the experimental phase, even if they are virtual.

After evaluating all the methodologies discussed above, the study conducted by Vicario et al. emerges as the most suitable that meets the requirements desired by this master project (VICARIO et al., 2021b). Therefore, the methodology and metrics proposed by them will be adopted as the basis for this study. However, it should be noted that while these approaches offer a comprehensive overview, they often encounter practical difficulties due to constraints in terms of resources and time, as the construction and testing of each load condition must be done physically.

The methodology of Vicario et al. was selected primarily because it was the only approach that explicitly took into account the impact of the environment. Another benefit was that this study did not concentrate solely on robotic manipulators, as force control on manipulators introduces additional factors related to the kinematics and dynamics of the robots, which are not directly relevant to force control.

Nevertheless, there are still notable areas for improvement in the selected methodology, with the primary issue being the requirement to utilize numerous distinct environments for metric calculations. This makes it challenging to practically execute experiments using the methodology. In contrast, the original study solely relied on simulations, which did not pose a problem. The remaining drawbacks are less significant. The absence of a stability metric can be addressed by designing appropriate metrics. Additionally, the assumption of linearity is not overly limiting, as closed-loop linearity is often preferred for controllers in the majority of cases. Therefore, the initial stage involves choosing or developing a set of metrics and a methodology that enables the classification of force controllers that account for the impact of the environment.

An alternative method entails splitting the controller into two distinct systems: one for monitoring performance and another for assessing apparent impedance (ROBINSON et al., 1999; ROOZING et al., 2017; RAMPELTSHAMMER et al., 2022). By adopting this approach, a thorough examination of the controller's performance and stability becomes possible. Nevertheless, the absence of objective criteria for determining the optimal apparent impedance poses a challenge when comparing various controllers. This study also seeks to delve deeper into this particular approach.

The lack of a consistent method for benchmarking creates difficulties in making

equitable comparisons and assessing the effectiveness and reliability of controllers directly. This dissertation presents an approach that overcomes these limitations by offering a universally applicable solution at the actuator level, which can accommodate different types of actuation systems like electrical, hydraulic, linear, and rotational actuators. The method is straightforward to implement and introduces objective metrics that are theoretically grounded and not dependent on the load, thus improving our capacity to develop and evaluate force controllers more effectively.

3 EXPERIMENTAL FRAMEWORK

To investigate benchmarking methodologies for actuators and controllers at the joint level, researchers create and build bench tests. One of those is ForceCAST, which consists of a motor module, a spring module (for SEA), a torque sensor module, and a virtual environment/load module (VICARIO et al., 2021a). The latter is a counter motor or a lever that can be excited manually. However, its capability is limited to small rotational electric actuators, typically in the range of 0 to 10 Nm. Another similar device designed for the same objective is the Metrox, which also consists of two interconnected motors with a torquemeter positioned in between (BÄHLER, 2021). The cited study by Bähler discusses a bench that can accommodate larger electric motors but is only applicable to rotational cases. Another relevant bench for this project is the FC2D (Force Control 2 Directions), which utilizes linear hydraulic and electric actuators. This bench shares a similar structure, with one motor connected to the other. However, it should be noted that while the FC2D bench supports both electric and hydraulic actuators, it does not support rotational actuators.

During the course of this work, two experimental benches were used: the ForceCAST bench made by the Altair Robotics Lab at the University of Verona, which was used during the Research Internship Abroad (BEPE - FAPESP) period; and the Impedance Control 2 Dimensions (IC2D), which was entirely designed, manufactured, assembled, and validated during this master's degree.

This chapter will discuss the ForceCAST bench, which is used to apply the methodology to rotational electric motors. Additionally, a detailed description of the IC2D construction will be provided. This bench was developed by researchers from the group and was designed to meet the exigencies of the methodology. The project begins with the structural design and the requirements to be achieved, followed by the selection of materials and manufacturing, the actuators and sensors employed in the bench, the design of the hydraulic and electric/electronic circuits, and finally, the project is validated by assessing the repeatability and accuracy of the experimental data obtained from the bench.

3.1 ForceCAST benchtest

The creation of the Forcecast testbench aimed at automating the experiments needed for benchmarking purposes. This section aims to give a thorough explanation of the experimental framework. The hardware testbed shown in Figure 4 is specifically designed for the experimental evaluation of control algorithms. The composition of the system includes multiple modules that have the capability to be reconfigured. These modules consist of the motor module, the spring module, the torque sensor module, and the virtual

environment/load module.

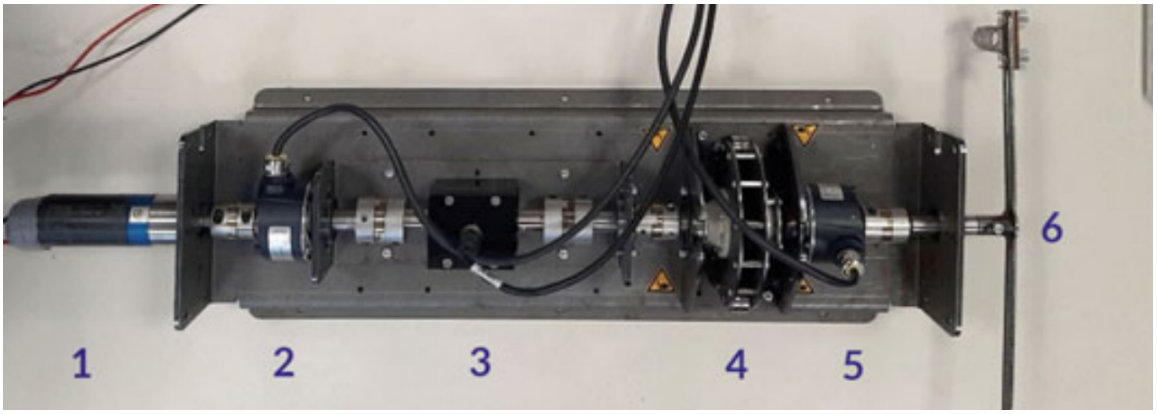

Figure 4 – Test bench where **1** is the motor, **2** the motor encoder, **3** the torque sensor, **4** the spring in series, **5** the environment encoder, **6** the environment (fixed spring)

The motor module has the capability to form either an elastic actuation system or a rigid actuation system, depending on whether it is coupled with the spring module or the torque sensor module, respectively. The spring module utilizes harmonic steel sheets with varying thicknesses, allowing for adjustments in the torsional spring stiffness by modifying the thickness or combining multiple sheets to achieve the desired outcome.

The only components at the high-end level are the encoders and the torque sensor. The encoders used are optical incremental encoders, specifically the DHO-05 model, which have a resolution of 2'000'000 pulses per revolution (Figure 5b). The torque sensor employed is a 10 Nm model called RT2A, manufactured by AEP Transducers (Figure 5a). For the virtual loads, the bench utilizes Maxon Motor DCX22L motors with GPX22UP 103:1 reducers (Figure 5c). On the other hand, the Maxon Motor EC45 with GPX22UP 86:1 reducer (Figure 5d) is used for testing purposes.

(a) Torque sensor (b) Enconders (c) Virtual load motor (d) Tested motor

Figure 5 – Forcecast components

The management of the ForceCAST Board is done through the use of a reusable embedded framework known as ForceCAST Embed. This framework is responsible for handling the hardware management tasks, allowing the user to easily create a control algorithm and execute it on the testbed. The code is executed on an STM32 Nucleo board

(F446RE), which is mounted on the ForceCAST board. This setup has the capability to power two brushed/brushless motors, two incremental encoders, two torque/force sensors, and also includes an emergency button for shutting off the power supply. The ability to interact with sensors and power electronics is made possible by internal components like analog-to-digital converters, digital-to-analog converters, and hardware circuits. To ensure the execution of tasks in a hard real-time manner, a 32-bit hardware timer is utilized within an interrupt-based system. To avoid the need for commercial RTOS licenses, custom-made firmware and software are employed. In order to achieve a quality control loop, it is crucial to close the loop at a minimum rate of 1 kHz and record the monitored variables. To attain this level of performance, extensive utilization of microprocessor Direct Memory Access (DMA) is necessary. This allows for a control loop frequency of 3 kHz while logging 4 float variables or 2 kHz while logging 10 float variables.

The software has been created using a structure based on classes, which can be easily customized to include new references, controllers, and hardware that can be controlled. The user interface of the ForceCAST embed framework shows any implemented controller, as depicted in Figure 6b. This framework provides the benefit of being able to modify the parameters of the controller and reference without the need to recompile the embedded code, which can be a time-consuming process. Furthermore, the interface enables users to execute a series of tests consecutively.

3.2 Impedance Control 2 Dimensions benchtest

The Impedance Control 2 Dimensions (IC2D) was an enhanced version of the FC2D bench mentioned earlier. Its primary objective was to create a flexible bench that could accommodate various types of actuators, including electric and hydraulic, rotational and linear ones. This would enable the construction of diverse virtual or real environments.

3.2.1 Mechanical structure

Firstly, we will provide an explanation of the bench's structure, as well as the primary mechanical and performance requirements. The IC2D test bench is a platform that possesses two degrees of freedom (DoFs) that are aligned in a colinear manner. The objective of this framework is to conduct an analysis and comparison of actuation systems and controllers at the joint level. The structure comprises of linear guides, rollers, and cars. It has the capability to test various types of actuators, including hydraulic and/or electric, as well as linear and/or rotational. Additionally, it includes a coupling system for load cells, springs, and dampers. The design of the bench is modular, meaning that the components are versatile and can be interchanged easily and quickly. This allows for the swift replacement of actuators, couplings, sensors, and setups as required. One potential setup is depicted in Figure 7.

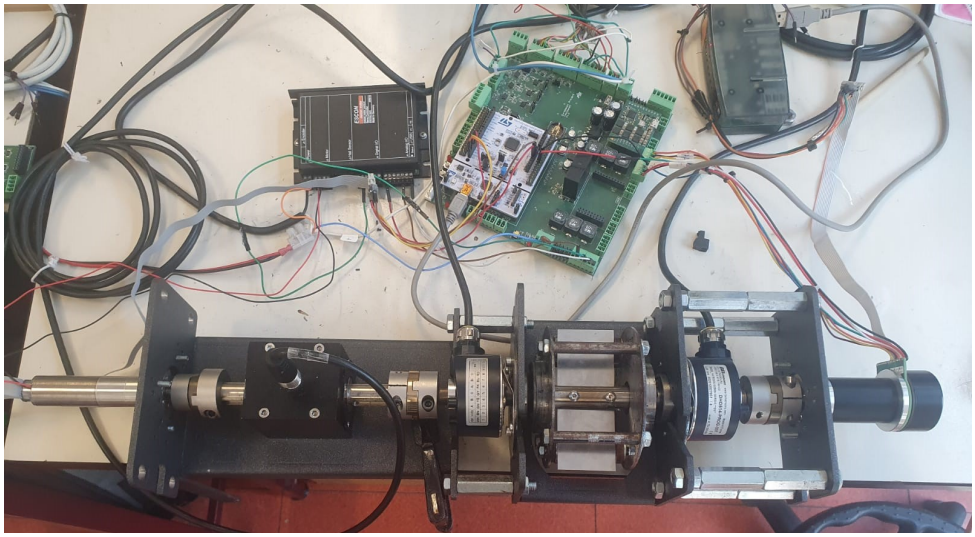

(a) Test bench experiment setup

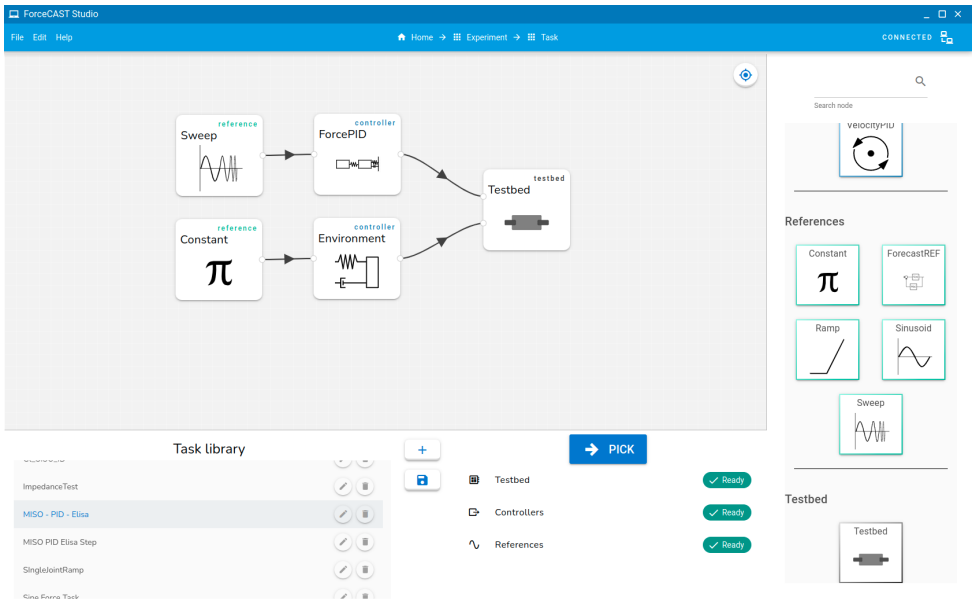

(b) Test bench user interface

Figure 6 – ForceCASt bench framework and software interface.

The objective of the project was to design a complex assembly consisting of two cars with adjustable inertia and two cars to transmit the actuator force. The assembly also needed to have easily removable springs and shock absorbers, the ability to connect encoders and force sensors, the flexibility to change actuators, and the option to block the actuator or one end of the load attached to the actuator. Additionally, the assembly needed to accommodate two actuators, which could be different models, attached simultaneously to simulate different environmental configurations. Each slider was required to endure a maximum mass of 10 kg, and the nominal force, excluding peaks, was expected to be approximately 5 kN for linear motion. For rotational motion, the nominal force would be lower. The bench needed to be robust to withstand the tests requirements and should be fixed on a breadboard to minimize mechanical vibrations. The following section provides

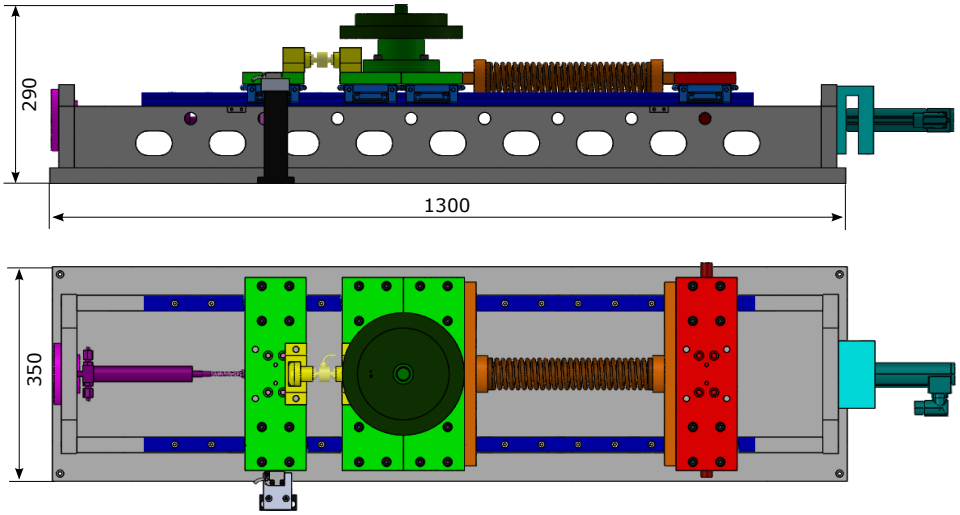

Figure 7 – Bench final assembly, its main dimensions, in mm. The parts represented in green are those that are able to move; in dark blue are the sliders and guides; in red are the parts that will be blocked; in purple and cyan are the actuation systems; in yellow the force sensor; in black on the side the position sensor; and in orange the spring assembly.

more detailed descriptions of the main components of the workbench.

3.2.1.1 Translations cars

To simplify manufacturing, the mobile part of the bench is composed of a standard platform attached to two sliders, which can be changed according to the additional parts selected. There are three categories of translation cars: the load car (Figure 8b), the transmission car (Figure 8c), and the blockage car (Figure 8d). Additionally, the standard platform can be utilized as a connection car if needed. The standard platform, depicted in Figure 8a, is suitable for all three aforementioned configurations.

3.2.1.1.1 Transmission car

The platform is connected to a hybrid block, which means it can be combined with either a nut/sleeve and spindle or a flange with angular offset compensation. The former is used for rotational actuators, while the latter is used for linear actuators. Currently, there are two possible configurations for the linear transmission car: the hydraulic actuation system (Figure 9a) and the electric actuation system (Figure 9b). Both systems are attached to the transmission block using the same angular and radial offset compensation. However, due to the distances between the actuators, their stroke, and the desired assembly setup, spacers need to be inserted to extend the actuator rods. To achieve this, the threaded bars were cut to the required dimensions to ensure a backlash-free assembly.

In the case of the rotational transmission car, a similar approach to the linear transmission was adopted. The existing block was utilized, and a socket was specially

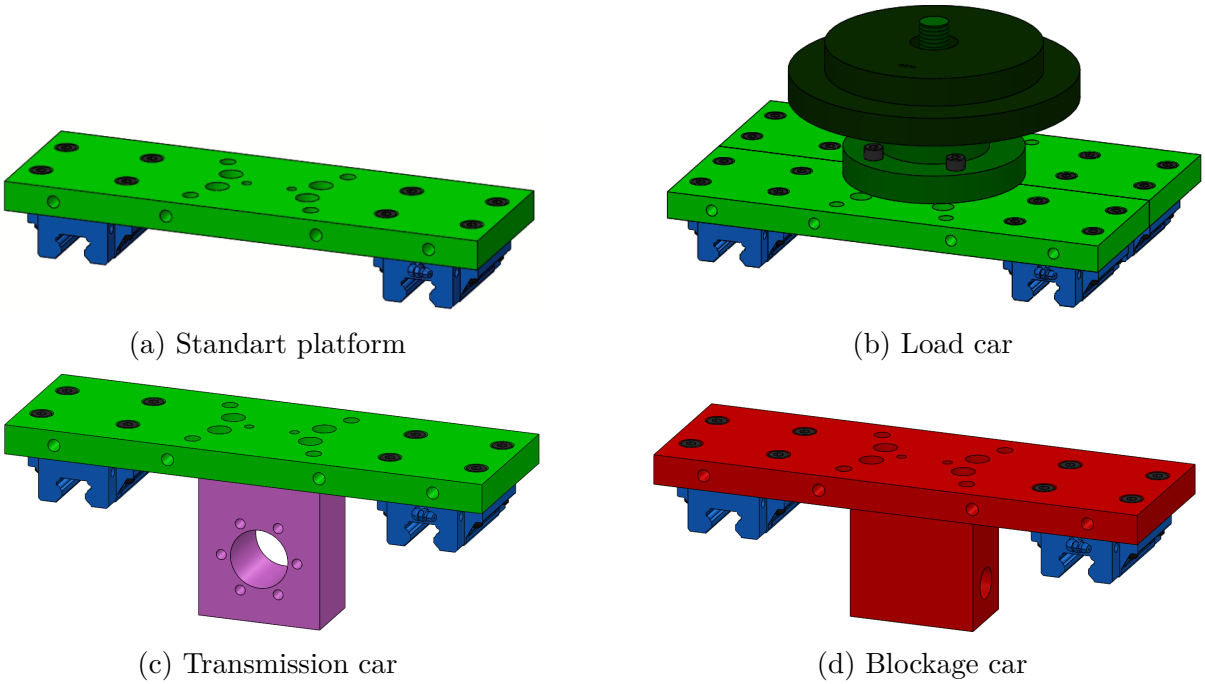

(a) Standart platform

(b) Load car

(c) Transmission car

(d) Blockage car

Figure 8 – The parts represented in light green are those that are able to move; in dark blue are the sliders; in red are the parts that will be blocked; in purple are the block for the transmission of force; and in dark green is the union part, that joins two platforms and supports variable weights.

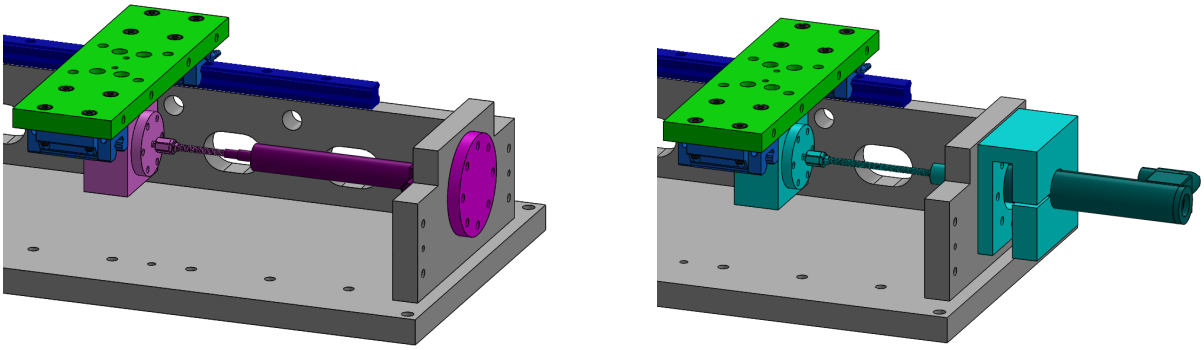

(a) In purple we have highlighted the hydraulic linear actuation system, in which we highlight the flange for fixing the cylinder.

(b) In cyan we have highlighted the electric linear actuation system, in which we highlight the flange for fixing the LinMot.

Figure 9 – Linear transmission assembly: In gray you have the global base, the sides and the flanges for fastening the actuators, in light green the standard platform and in dark blue the linear guides and sliders.

created to hold a sleeve/nut with a spindle. This setup enables the conversion of the actuator's rotational motion into linear motion for the car. The chosen components for this conversion are the BN25x5R NOWPR universal ball sleeve/nut and the BN5x5R 90 G5 spindle from SKF. Figure 10 illustrates these components.

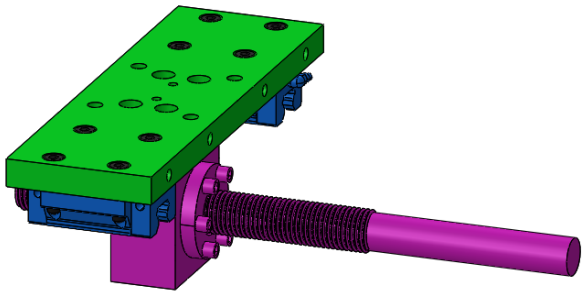

Figure 10 – Rotational transmission assembly: In purple the sleeve/nut with a spindle attached to same transmission block.

3.2.1.1.2 Load car

The load car is constructed by connecting two modular platforms using the union part shown in Figure 8b. This part also has the capability to attach a threaded bar, which functions as a guide for the iron weight plates. The height of the union part is determined to prevent the plates from colliding with the coupling fixings and to ensure that the load is evenly distributed among the four sliders that support the assembly.

3.2.1.1.3 Blockage car

The purpose of the blockage car is to enable the utilization of a single actuator with a known load and to evaluate the actuator's performance by conducting tests with it completely blocked. These tests are commonly employed in benchmarking methodologies. To achieve this goal, a steel shaft with a diameter of 20 mm is employed as a latch. The dimensions of the shaft are carefully determined to withstand the force exerted by the contact surface between the shaft and the block, which can reach up to 5 kN. The shaft is designed to have an interference fit with the block and the side supports of the structure, ensuring that there is no backlash.

3.2.1.2 Structure, actuators flanges, linear guide and sliders

The linear guides are attached to supports, which are fixed onto a global base. At the end of the guides, there are two universal flanges that allow both the cylinder shaft and the spindle axis to pass through. The flanges have a hole pattern, which enables the production of adjustable fixing parts for each actuator to be attached to them, as shown in Figure 9. The chosen linear guide is a singular part with a length of one meter. To ensure smoother movement of the sliders, the selected model is the TRH25-FL from *Kalatec*. Its static and dynamic load capacity exceeds the desired 10 kN. Up to six sliders can be fitted per guide. The selection of linear guides creates a gap between the supports for the guides and the platforms, which can be useful for wiring instrumentation. During the assembly of the linear guides, a dial gauge was used to ensure that the geometric tolerances specified

in the manufacturer's datasheet were met. Additionally, a lubricating oil (SAE10) was applied to minimize friction in the system.

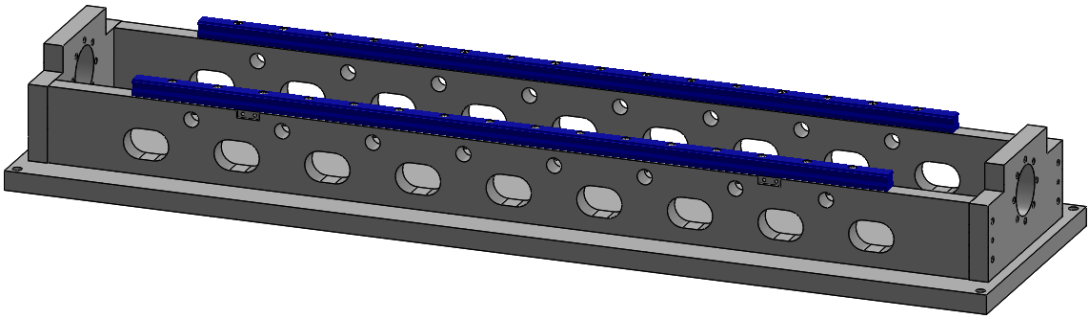

Figure 11 – Rails support on the global base, the linear guides are in dark blue

3.2.1.3 Load Cell coupling

The assembly of the load cells is divided into two main sections (Figure 12a). The first section is responsible for attaching the load cell to the platform, while the second section is custom-made and threaded for each sensor. The curved surface of the first section helps to compensate for slight angular misalignment, preventing any residual stresses in the sensor readings and ensuring a tight assembly without any backlash (Figure 12b). After being attached to the coupling, the load cell is then secured between two platforms, as depicted in Figure 12c.

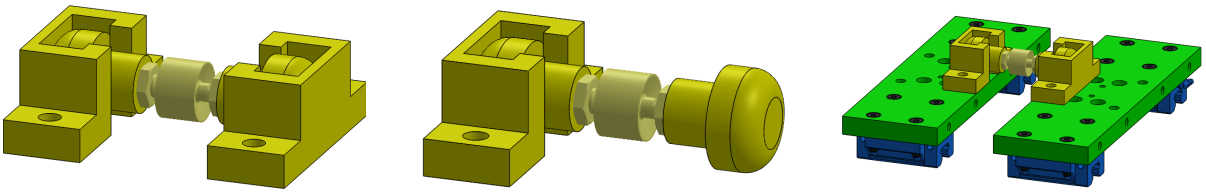

(a) (b) (c)

Figure 12 – In yellow the entire load cell fastening set is represented. The cell represented is the Burster 8417-6005.

3.2.1.4 Springs and dampers fixation

The fixation of the springs and dampers on the platforms is intended to maintain the symmetry of the system at all times. These combinations enable the utilization of various environments and even the incorporation of series elastic actuators (SEA). At present, the springs being used are those that have been modified from another setup, but there are plans to procure a wider range of springs and dampers. As a result, four holes were drilled on each side of the platforms to allow for the attachment of different types of springs, shock absorbers, or even supplementary components, as depicted in Figure 13. To utilize the springs that are already available, a flange and an additional component that connects the flange to the side of the platform were adapted.

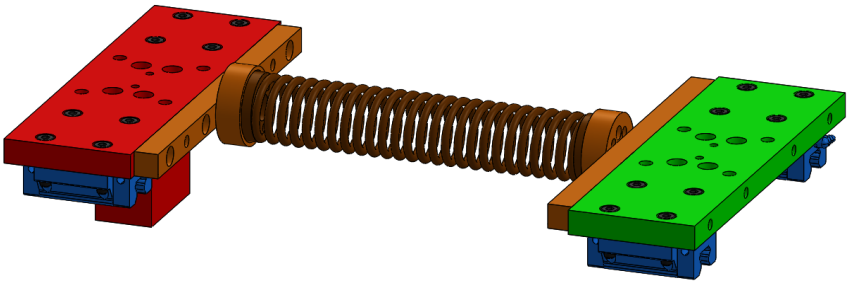

Figure 13 – Spring assembly currently used is represented in orange.

3.2.1.5 Material selection

The initial proposal for the structural parts, platforms, and coupling parts was to use aluminum alloy 6082. This choice was made to achieve the desired strength while keeping the overall mass relatively low compared to simple carbon steel. However, since the bench is designed to be assembled and disassembled frequently, a decision was made to use SAE 1020 steel instead. This was because the threads needed for assembly could wear out over time if aluminum was used. As a result, the final mass of the bench can reach up to 200 kg depending on how it is assembled. Since the bench is placed on a breadboard, there is no need to move the base structure, which contributes the most to the overall mass. To prevent steel from oxidizing over time, a surface treatment was necessary. Galvanic nickel was chosen for this purpose as it provides a more refined surface layer compared to zinc plating. Additionally, galvanic nickel has a more aesthetically pleasing appearance, as shown in Figure 14.

3.2.1.6 Good Design Practices

The aim of the design was to simplify the manufacturing process and ensure that all geometric tolerances are met during assembly. To achieve this, guide pins were used both for positioning and to withstand shear forces on the screws. Additionally, an alignment nail was included on one side to facilitate the alignment of the rails and smooth sliding of the sliders. The CAD designs, technical drawings, and assemblies can be found in (VERGAMINI; SANTOS; ZANETTE, 2023). Figure 7 shows the support for the linear magnetic encoders, which will be utilized to measure the position of the platforms.

3.2.2 Fluid power system

The fluid power system was created with the specific needs of the hydraulic actuator in mind, which is used on various experimental platforms at the Legged Robotics Group facility. These platforms include the hydraulic robotic leg and hydraulic arm manipulator (SEMINI; TSAGARAKIS; VANDERBORGHT, et al., 2008; UR REHMAN et al., 2016). The selection and design of the key components were based on the technical requirements to ensure optimal performance and reliability. Figure 15 provides an overview of the

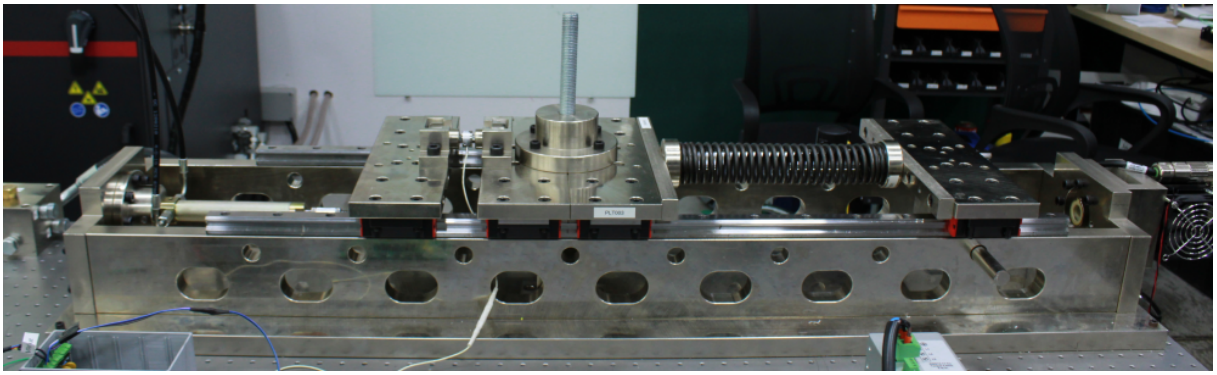

Figure 14 – IC2D bench final assembly

hydraulic circuit diagram and the relevant hardware. More detailed information about these components will be discussed in the subsequent sections.

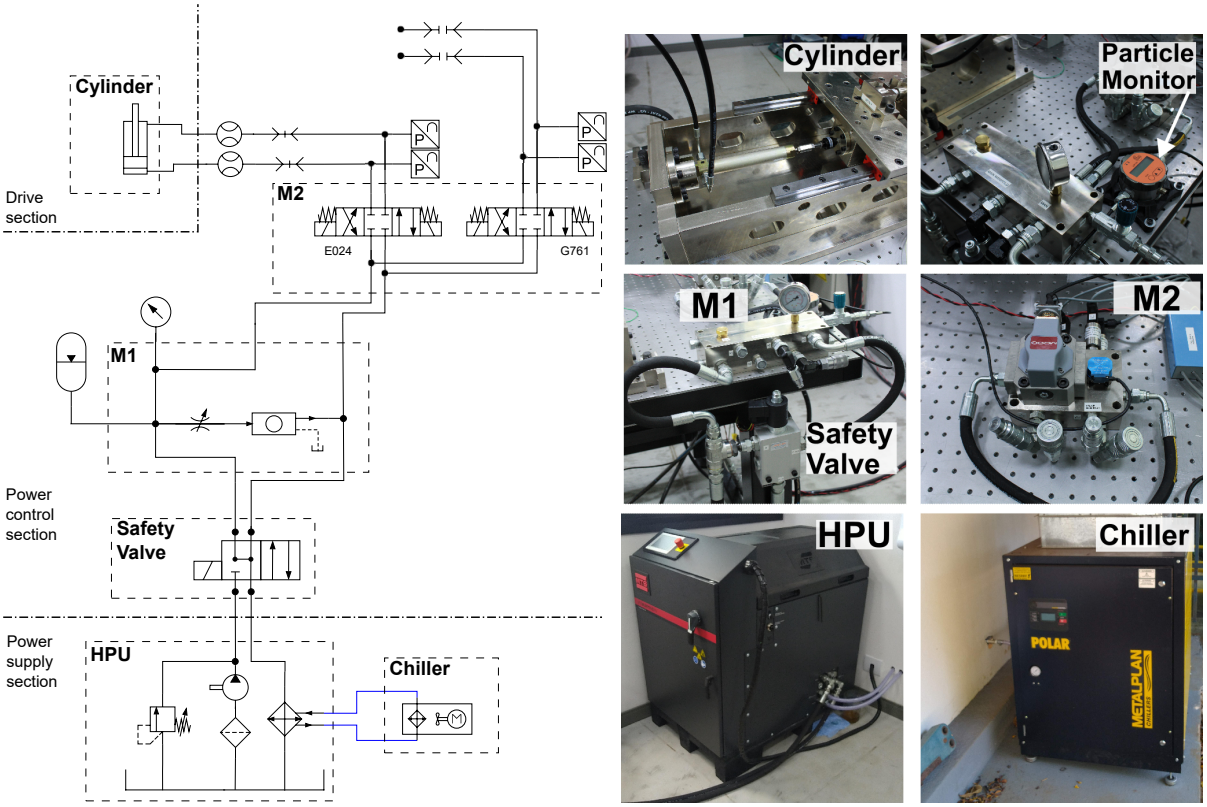

(a) Hydraulic circuit diagram.

(b) Fluid power hardware.

Figure 15 – Fluid power system overview containing the main elements of the power supply, power control, and drive sections. The accumulator and flow sensors are shown only in the diagram (a).

3.2.2.1 Hydraulic Power Unit

In contrast to electrical systems that solely rely on a battery for actuation, hydraulic systems necessitate a collection of components that form the hydraulic power unit (HPU). The primary constituents of a conventional HPU include:

- *Tank*: It is the fluid reservoir, which is the place where the fluid is stored and cooled prior to being transferred to the pump.

- *Power source*: Typically, the pump is powered by either an electric motor or a combustion engine. While combustion engines offer greater autonomy, they tend to be larger, noisier, and are commonly used in outdoor settings. In contrast, electric motors provide a quieter alternative and can be more compact. Although they have lower autonomy, recent advancements in battery technology and technical innovations have significantly improved the energy autonomy of electric-powered mobile HPUs (CHO et al., 2021).

- *Hydraulic pump*: The pump's main role is to increase the pressure of the fluid in the tank and transfer it to the actuation system. However, it may encounter efficiency losses due to internal leaks and friction. Variable displacement pumps have a high efficiency of 99% at low pressures (< 100 *bar*), but this efficiency can decrease to around 90% at higher pressures (< 250 *bar*). Furthermore, the efficiency can be affected by the temperature of the fluid. As the temperature increases, the fluid becomes less viscous, which can lead to increased internal leakage.

- *Relief valve*: The primary function of this valve is to regulate the highest pressure within the system, thus ensuring its safety. Consequently, it maintains a consistent pressure level in the circuit by preventing it from surpassing the valve's predetermined value. In the event that the pressure exceeds this specified value, the valve will open and redirect the fluid back to the tank. However, this action results in a decrease in hydraulic power and an increase in fluid temperature.

- *Heat exchanger*: In order to ensure the proper functioning of the HPU, it is necessary to exchange heat due to the common pressure losses in the fluid. This heat exchange can be achieved using either water or air. In the case of robotic devices, the temperature of the fluid is typically maintained below 60 $°C$ to ensure the safety of the hydraulic components.

- *Filters*: As previously stated, maintaining the cleanliness of the fluid is of utmost importance. Therefore, it is necessary to have a filter in place to prevent any contamination of the valves. These valves are highly sensitive to contamination, and even particles as small as tens of micrometers can cause total or partial blockage, resulting in reduced performance or complete inoperability of the valve (PARK, 1997). Oil contamination is known to deteriorate sealing elements, especially towards the end of their lifespan. Alongside the filter, it is highly recommended to have contamination sensors installed in the line to detect any contamination and facilitate timely filter changes without causing damage to any component.

The Hydraulic Power Unit (HPU) used in this study is the MTS model HPU 515-11 Water Cooled, which is equipped with a variable displacement pump. It has a regulated operating pressure of up to 207 *bar* and a flow rate of 40 *lpm*. The filtration system is designed to operate at full flow on the return side. The pump is driven by an 18.5 kW electric motor. The HPU is equipped with sensors to measure pressure, oil level, and temperature. Additionally, it is equipped with a heat exchanger that has a heat removal capacity of 18.7 kW. The oil reservoir has a capacity of approximately 200 L. The HPU is capable of providing the required pressure and flow to supply the IC2D servovalves.

3.2.2.2 Chiller

The function of the chiller is to provide a coolant fluid to the HPU, which is an essential component of fluid power systems. Temperature control is a critical aspect of these systems, and it is required that the oil temperature remains at 40 $°C$ during operation, in accordance with the standard. It is important to avoid temperature fluctuations as they can negatively affect the integrity and viscosity stability of the oil. While the HPU can warm the oil in its reservoir, it is necessary to remove excess heat, and this is achieved by the chiller supplying cooled water within the temperature range of 5 $°C$ to 25 $°C$. The specific chiller model installed is the PA-15 RE, manufactured by Metalplan, and it has a heat removal capacity of 17.4 kW.

3.2.2.3 Hydraulic hoses and connections

The hoses establish a connection between the fluid system, providing greater flexibility in terms of setup compared to tubes. In this particular configuration, hoses were chosen over tubes due to their ability to withstand a working pressure of 215 *bar*, which exceeds the maximum working pressure supported by the HPU. The specifications for hose diameter and length took into account factors such as pressure loss and adherence to assembly guidelines outlined in DIN 20021 standards. To ensure optimal sealing, the adopted standard for connections was BSP. Additionally, quick connector couplings were incorporated to facilitate the switch between servovalves.

3.2.2.4 Manifolds

Due to the different hardware connected to the HPU, multiple fluid lines are required. In order to distribute these lines, a distribution manifold (M1) was designed and manufactured. Additionally, a servovalves manifold (M2) was also designed. The distribution manifold (M1) was designed to accommodate six different lines, including the particle counter line, pressure gauge, and accumulator (see Figure 17a). The servovalves manifold (M2) was designed to match the port pattern of Moog servovalves E024 and G-761, and also supports pressure sensors on the actuation lines of both valves (see Figure 17b). Both manifolds were manufactured using SAE 1020 carbon steel, and their structural

integrity under the maximum working pressure of 207 *bar* was evaluated through finite element analysis. The maximum stress computed on both manifolds, using the von Mises stress criteria, is below 170 MPa, which provides a safe margin for structural integrity considering the yield strength of SAE 1020 hot-rolled carbon steel, which is 210 MPa (CALLISTER; RETHWISCH, 2007). To prevent rust, the surface of the manifold was treated with nickel.

3.2.2.5 Hydraulic oil

Oil serves as the medium for transmitting mechanical power. In the field of robotics, mineral oil is commonly used as a fluid for this purpose. Its low compressibility allows for faster and more effective energy transfer. Additionally, the oil acts as a lubricant for circuit components, such as valves and cylinders, ensuring their longevity and minimizing leakage. The specific fluid chosen for this system is ISO 68 mineral hydraulic oil, which has a density of 875 kg/m^3 and a standard kinematic viscosity of 68 cSt at 40 $°C$. At atmospheric pressure and without the presence of mixed gas, the fluid has a bulk modulus of 1.34 GPa and a compressibility rate of 0.75 % per 100 *bar*. According to the DIN 51524-2 standard, the fluid falls under the HLP class, which is known for its enhanced corrosion resistance, wear protection, and aging stability.

3.2.2.6 Sensing

The IC2D testbench includes pressure and flow sensors as part of its instrumentation hardware. Piezoelectric sensors are used to measure the pressure of the A and B lines in the hydraulic actuation system, which are connected to the M2 manifold for both valves. These pressure sensors have a range of 0 - 250 *bar* and an accuracy of ±0.25%, specifically the RS PRO 797-4986 model. Additionally, flow sensors will be installed on the cylinder lines to fully enable sensing of the IC2D hydraulic actuator.

3.2.2.7 Auxiliary elements

To enhance the efficiency and maintainability of the system, additional components such as a pressure gauge, accumulator, and particle counter are necessary. The pressure gauge, positioned at M1, enables the monitoring of system pressure. An accumulator will be installed to mitigate pressure fluctuations within the system. The particle counter, also known as a contamination sensor, will be placed at M1. Specifically, the LDP100 sensor model from IFM Electronic is utilized to monitor oil particle levels in accordance with ISO 406/NAS 1638 standards. The inclusion of this sensor is crucial in ensuring that both valves, E024 and G-761, operate with an extended lifespan by preventing blockages.

3.2.2.8 Servovalves and cylinder

The system responsible for converting hydraulic energy from the HPU into mechanical power, enabling the system to exert forces on a specific load, is known as the *actuation system*. This process involves the utilization of various components, which include:

- *Actuator*: The task of converting fluid power into mechanical power is carried out by hydraulic actuators in robotics. Among these actuators, double-acting cylinders are the most commonly used. Figure 16 illustrates these actuators, which feature two connection ports for the fluid to enter and exit the internal chambers. This design allows for the control of both the extension and retraction of the piston rod in a cylinder.

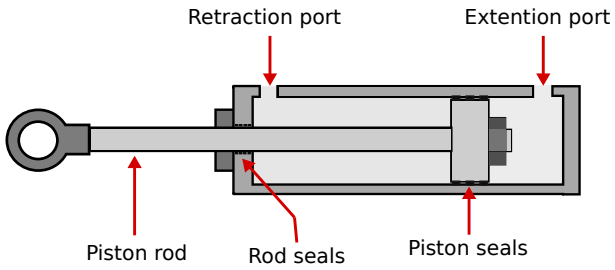

Figure 16 – Simplified schematics for linear hydraulic actuator and its main elements. Adapted from (BOAVENTURA; SEMINI, 2020).

- *Directional Control Valve (DCV)*: Proportional and servovalves are the most commonly utilized valves in the field of robotics. Servovalves are particularly recommended for robots that require dynamic movements. Despite being more expensive, servovalves offer significantly faster response times, typically in the range of a few milliseconds. Additionally, they provide more precise and consistent flow control with minimal hysteresis. These high-performance valves enable the achievement of high control bandwidth and robustness, making them essential for hydraulic systems in robotics. Furthermore, servovalves serve as an ideal interface between low-power electric signal control and high-power robot joints.

  The servovalve contains a spool, which is a movable component situated within the valve housing. The spool is responsible for regulating the flow by either obstructing or opening the valve ports, thereby controlling the magnitude and direction of the flow. This movement is activated by applying an electrical input to the valve. Additionally, four-way valves with zero-lapped spools exhibit a linear relationship between the spool stroke and the controlled flow, as described by a linear curve (MERRITT, 1991).

  Typically, servovalves are equipped with four connection ports, namely a, b, s, and t. These ports are responsible for linking the valve to the actuator chamber a, actuator

chamber b, supply line s, and tank t (also known as the return line). The configuration of these ports depends on the position of the spool inside the valve. In this study, we utilize two-stage electrohydraulic servovalves that incorporate a flapper valve in the first stage. It is worth mentioning that these valves offer a compact size and wide bandwidth due to their design features. However, their operational principle and dynamic characteristics still resemble those of standard 4/3 DCV.

To evaluate the force and impedance control of hydraulic actuators used in quadruped robots, we have chosen the LB6 1610 0080 model cylinder from Hoerbiger, which is a double-acting type. Similarly, the E024 four-way directional servovalve from MOOG is also selected. These components have been previously utilized in the hydraulic quadruped robot HyQ (SEMINI; TSAGARAKIS; GUGLIELMINO, et al., 2011a; FAHMI et al., 2020). The cylinder has a piston mass of 445 g and a stroke length of 80 mm. The piston diameters are 16 mm and 10 mm, while the dead zone is 400 mm^3. The cylinder exhibits a viscous friction of 700 N, with Coulomb and breakaway friction of 100 N. The servovalve has a bandwidth of 250 Hz at a pressure of 210 bar, and a maximum rated flow of 7.5 L/min with a pressure drop of 70 bar. Additionally, a second servovalve, the G761 model from MOOG, with a bandwidth of 450 Hz, has been installed on the servovalve manifold (Figure 17b) to characterize the control system with a wider servovalve bandwidth.

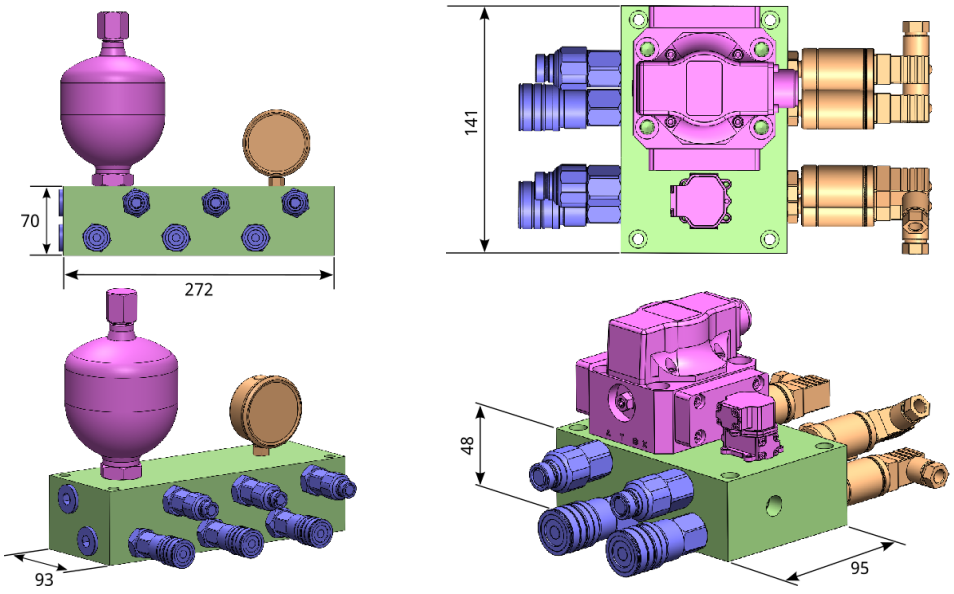

(a) Distribution manifold assembly. (b) Servovalves manifold assembly.

Figure 17 – Fluid power system manifolds assemblies for functionality preview. The manifolds are green and quick connectors are blue on both figures. In (a), the accumulator and the pressure gauge are pink and orange, respectively. In (b), the servovalves and the pressure sensors are pink and orange, respectively.

3.2.3 Electric, electronic, control and data acquisition

Following the completion of the mechanical structure and hydraulic circuit assembly, the next step involved the development of electrical installations. These installations were crucial for powering the electrical actuator and establishing the necessary electrical circuit for sensor reading, control signal transmission, and data acquisition during the conducted tests. This section will delve into these steps, providing a comprehensive overview of the bench's functioning.

3.2.3.1 Electric set up

The linear motor used in the experiment was the LinMot PS01-37x120F-HP-C (stator) and PL01-20x240 / 180HP (slider) models. It had a maximum force of 255 N and a maximum stroke of 120 mm. To control and power the system, a LinMot B1100-GP-HC drive and an S01-72/1000 power supply were utilized. The wiring of the components can be seen in Figure 18. In order to achieve more accurate measurements, an Interface SMT1-250N load cell with a force range of 250 N was used. The motor's configuration was performed using LinMot-Talk, a software available for download on the LinMot website.

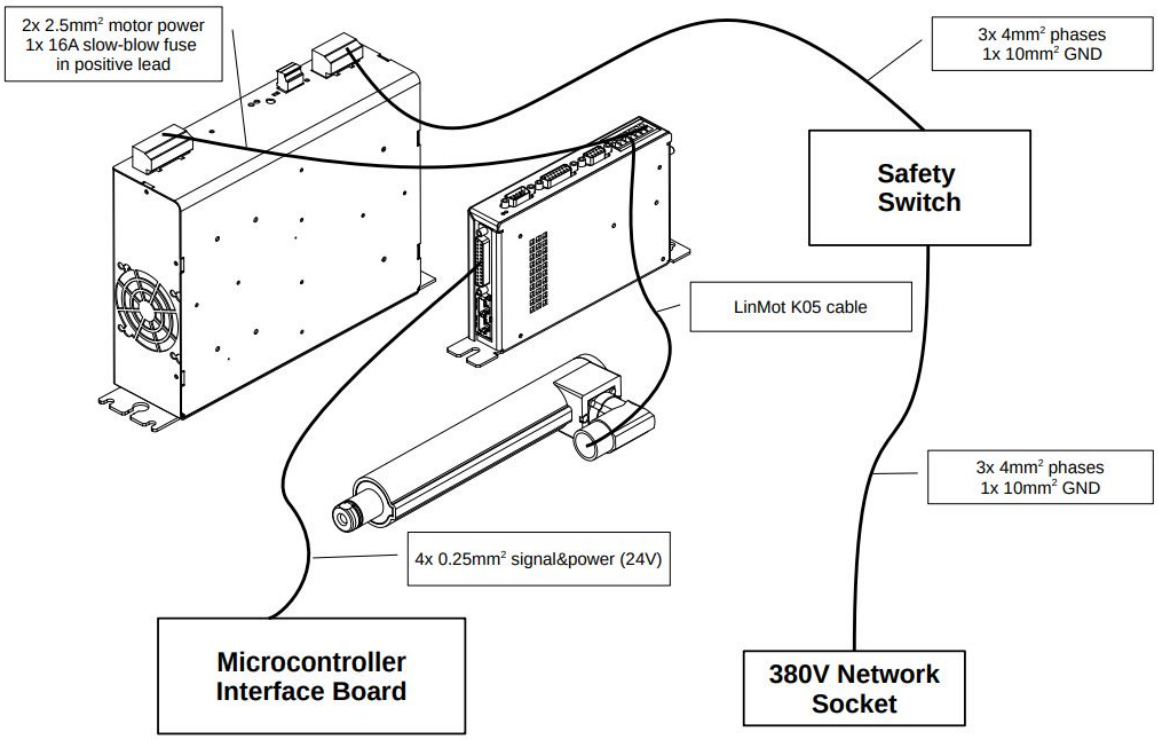

Figure 18 – Connection of the LinMot linear motor to its drive, power source, and the other components of the system, adapted from (HAMMER, 2016).

As illustrated in Figure 18, the LinMot power supply is connected to a three-phase 380V network socket. However, this type of electrical installation is not commonly found

in Brazil. Therefore, it is required to install a 5 kva 220/380V 60 Hz three-phase auto transformer.

3.2.3.2 Electronics and data acquisition

Both drivers have the same signal input range of -10 V to 10 V for the actuators. The linear motor was powered by the S01-72/1000 power supply. The LinMot driver used was the B1100-GP-HC, while the servo valve driver was the G123-815A001 from MOOG. The load force was measured using two different load cells. For the first actuator, a miniature load cell 8417-6005 from Burster was used, which had a range of 5 kN, a nominal sensitivity of 1 mV/V, a maximum operating force of 120 %, and a full-scale deflection of 60 μm. For the second actuator, an Interface SMT1-250N load cell was used, which had a range of 250 N, a nominal sensitivity of 2 mV/V, a maximum operating force of 200 %, and a full-scale deflection of 15 μm. The pressure at the control chambers was measured using NAT 8251.74.2517 pressure sensors from Trafag AG, which had a maximum pressure reading of 25 MPa and an accuracy of $\pm$ 0.5 %. The incremental encoder used was the LM10IC001AB10F00 from RLS, which had a resolution of 1 μm. The functional diagram of the electronics is shown in Figure 19.

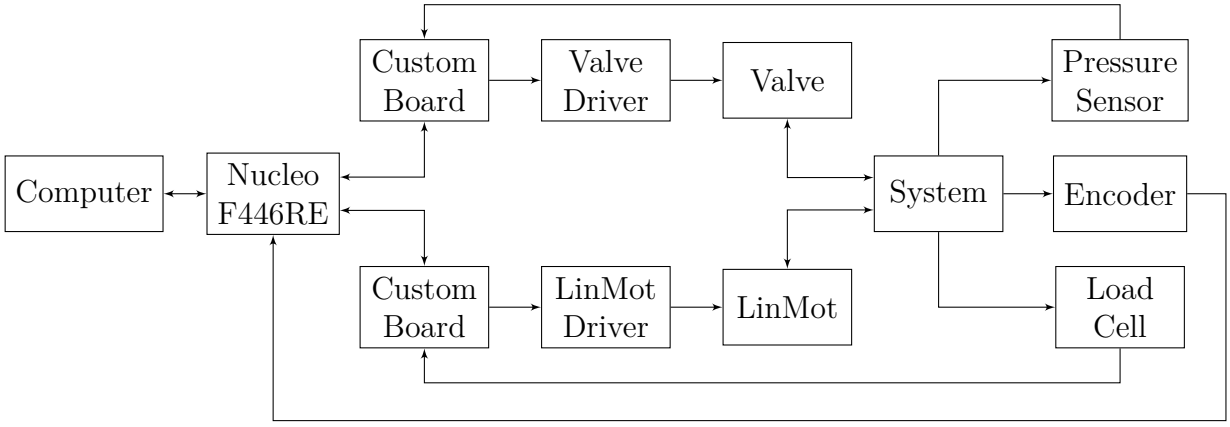

Figure 19 – Functional diagram of the electronic connections

The 3D representation of the custom board that features the circuits described in Sections 3.2.3.3 to 3.2.3.5 can be seen in Figure 20.

Data acquisition and control commands are processed using the STM32 Nucleo-F446RE microcontroller, from STMicroelectronics, with an ARM32-bit Cortex-M4 CPU, real-time capability up to 180 MHz, and 512 kB flash memory. This MCU uses a 3.3 V signal level so an electronic I/O signal conversion for actuators and sensors is necessary, since the sensors used are in the 0 to 10 V range and the actuators need an input ranging from -10 to 10 V. This conversion was made using a customized board with the following capabilities: 0 to 10 V and 0 to 5 V to 0 to 3.3 V conversion for the sensors (Section 3.2.3.3), 0 to 3.3 V and 0 to 5 V to -10 to 10 V for the actuators (Section 3.2.3.4), an amplifier circuit

for the load cell (not being used currently) and a power regulation circuit (Section 3.2.3.5). The complete circuit can be seen in (VERGAMINI; SANTOS; ZANETTE, 2023).

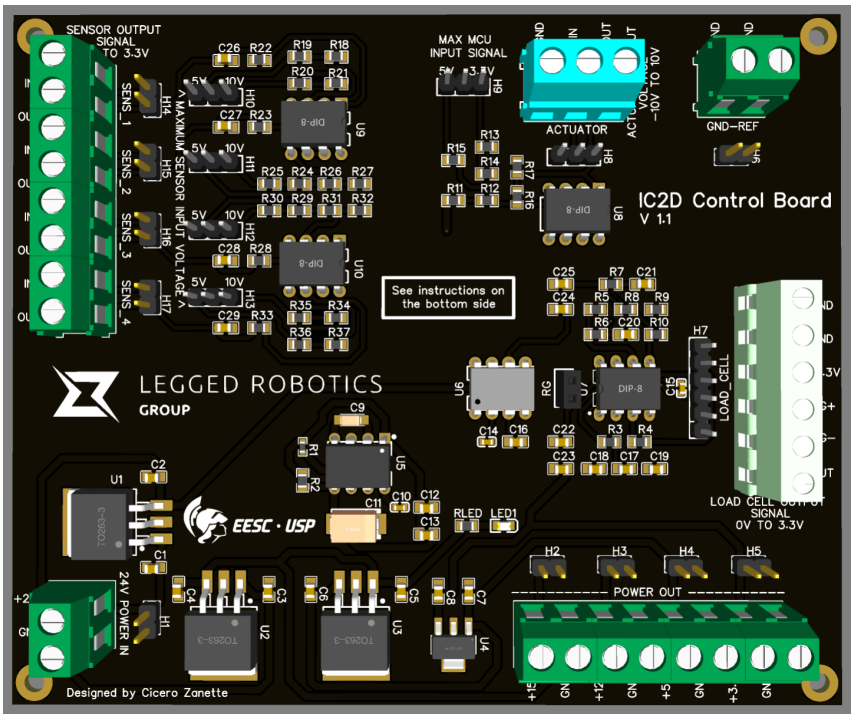

Figure 20 – 3D model of the customized board

3.2.3.3 Sensors circuit

The circuit for the sensors includes a voltage divider that has two different setups. One configuration is used for input voltages ranging from 0 to $10V$, while the other is used for input voltages ranging from 0 to $5V$. In both cases, the output voltage ranges from 0 to $3.3V$. To enhance signal preservation, an operational amplifier was incorporated in a buffer configuration. Additionally, a low-pass filter was employed to enhance noise rejection. The circuit diagram can be seen in Figure 21.

In this setup, when the switch is set to the 0 to 5 V position, the equation that determines the voltage divider ratio is Equation 3.1.

$$U_+ = \frac{R_4}{R_3 + R_4} U_{in} = \frac{39\,\text{k}\Omega}{59\,\text{k}\Omega} U_{in} \Rightarrow U_+ = 0.66 U_{in}, \quad 0\,\text{V} \leq U_{in} \leq 5\,\text{V} \tag{3.1}$$

which rescales the input range of 0 to 5 V to the range of 0 to 3.3 V, and when the switch is set to the position of 0 to 10 V, the voltage divider ratio is determined by Equation 3.2.

$$U_+ = \frac{R_4}{R_1 + R_2 + R_3 + R_4} U_{in} = \frac{39\,\text{k}\Omega}{118\,\text{k}\Omega} U_{in} \Rightarrow U_+ = 0.33 U_{in}, \quad 0\,\text{V} \leq U_{in} \leq 10\,\text{V} \tag{3.2}$$

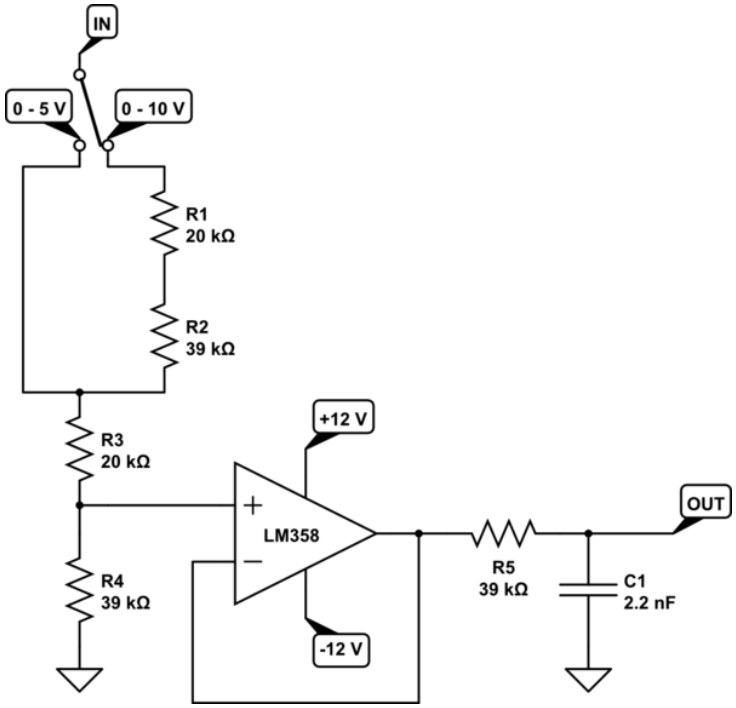

Figure 21 – Sensors circuit

which scales the 0 to 10 V input to the 0 to 3.3 V range.

Equation 3.3 demonstrates that the operational amplifier buffers the signal and the low-pass filter, with a cutoff frequency of 1.8 kHz, filters it.

$$f_c = \frac{1}{2\pi RC} = \frac{1}{2\pi \times 39\,\text{k}\Omega \times 2.2\,\text{nF}} = 1.86\,\text{kHz} \tag{3.3}$$

In these circuits, we establish connections with pressure sensors that already possess an output of 0 to 10 V, along with the utilization of the Mantracourt SGA/D signal conditioner to amplify the signal originating from the strain gauge load cells.

3.2.3.4 Actuator circuit

The actuator circuit comprises an operational amplifier that adjusts the input signal range from 0 to 3.3 V or 0 to 5 V to -10 to 10 V. Figure 22 illustrates the circuit.

In this setup, when the switch is set to the 0 to 3.3 V position, the output is determined by Equation 3.4.

$$U_{out} = \left(\frac{U_+}{R_1//R_2} - \frac{5 - U_+}{R_4 + R_5}\right) R_6 + U_+ = 6.07U_+ - 10, \quad 0\,\text{V} \leq U_{in} \leq 3.3\,\text{V} \tag{3.4}$$

which scales the input range of 0 to 3.3 V to the output range of -10 to 10 V. When the switch is set to the position where the input voltage is between 0 V and 5 V, the output is determined by Equation 3.5.

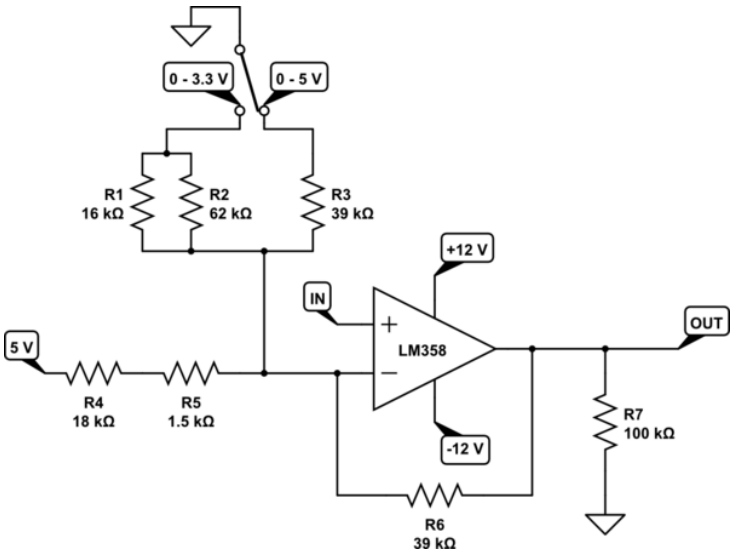

Figure 22 – Actuator circuit

$$U_{out} = \left(\frac{U_+}{R_3} - \frac{5 - U_+}{R_4 + R_5}\right) R_6 + U_+ = 4U_+ - 10, \quad 0\,\text{V} \leq U_{in} \leq 5\,\text{V} \tag{3.5}$$

which adjusts the input range of 0 to 5 V to the output range of -10 to 10 V.

3.2.3.5 Power regulation circuit

The circuit depicted in Figure 23 is responsible for producing all the voltages utilized on the board. A 24 V external power source is connected, and four linear regulators are employed to generate output voltages of 15, 12, 5 and 3.3 V. To generate the -12 V required by certain operational amplifiers on the board, a switched-capacitor voltage converter was implemented, following the instructions provided in the datasheet. Additionally, an LED indicator was incorporated to signify that the board is powered.

3.2.3.6 Software

The software implemented on the micro controller is the ForceCAST Studio, provided by Altair Robotics Laboratory (VICARIO et al., 2021a). In the firmware developed in the ForeCAST project, the most efficient way of making ADC reads for the sensors used during the control loop was with DMA and continous conversion enabled. In this configuration, multiple ADC reads from the same channel were continously stored in a buffer and so the controllers always had access to multiple recent reads in order to calculate the average. In the previous firmware version, it was only possible to use three ADC channels using DMA and continous conversion of the ADC. That was because the firmware set each channel to a respective DMA bus, which there are only three in the MCU, as shown in Figure 24.

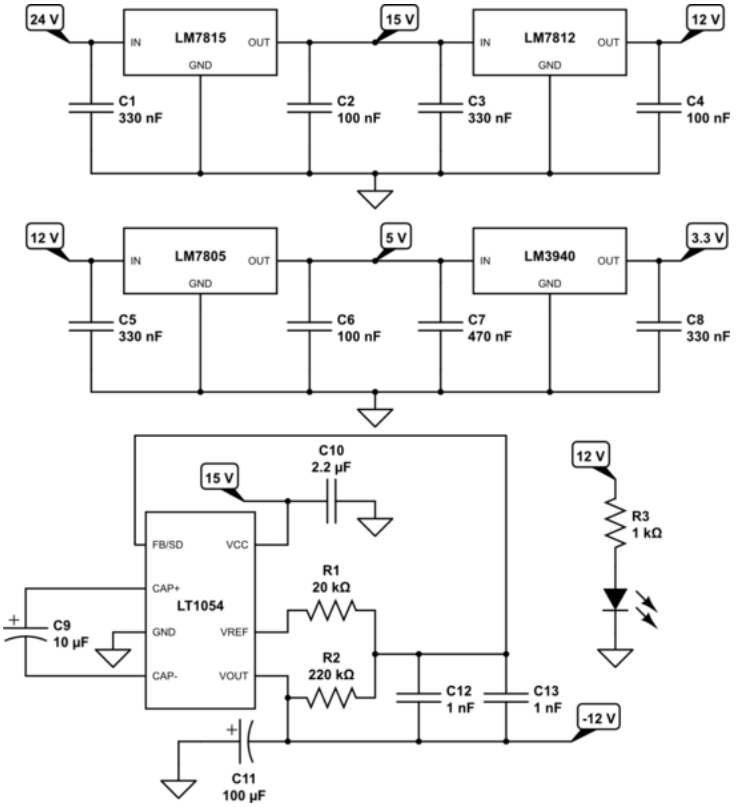

Figure 23 – Power circuit

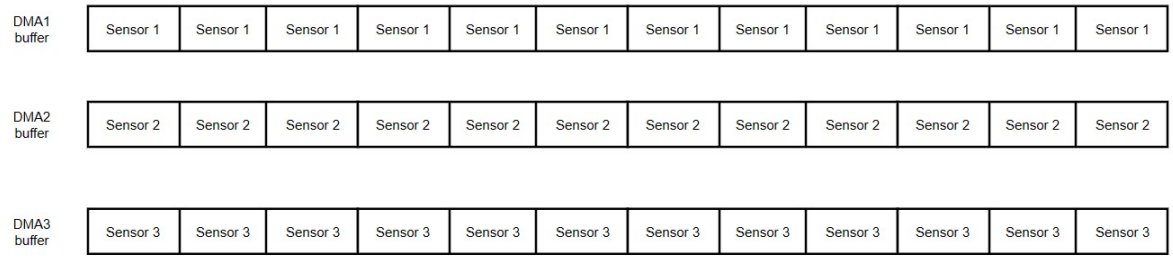

Figure 24 – For each DMA bus, a buffer was filled with the reads of a single sensor

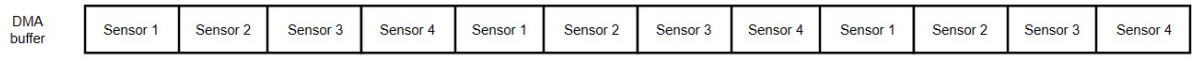

Figure 25 – In the new modified firmware, only one DMA bus is used with a single buffer. The buffer is filled with the reads of all the necessary sensors.

This DMA configuration then allowed the use of only three analog inputs at a time, for the ForceCAST bench configuration it was sufficient; however, IC2D, as it had pressure sensors, a larger number of load cells, required adapting the use of DMA to meet our demands. Therefore, the firmware was modified so that only one DMA bus was used for all the ADC channels by configuring the ADC to make a sequence of reads of multiple different channels and those values were stored in a buffer using the DMA. In this way, in order to get the reads of a given ADC channel, the firmware had to select only the desired channel in the buffer from all the different ADC reads for different sensors, as shown in

Figure 25.

By implementing these modifications, we successfully opted for the comprehensive configuration of the eight analog sensors. Additionally, we established a closed control loop operating at a frequency of 5 kHz. To ensure the desired speed, we limited the logging of variables to 1 kHz. This means that out of every five measurements, only one is transmitted and stored in the experiment log.

3.2.4 Validation

To validate the construction of the bench, we examined three aspects. The initial aspect focused on experimental repeatability, which involved assessing the consistency of measured data across multiple runs using the same setup. The second aspect involved evaluating backlash-related phenomena by measuring the displacement of a blocked car subjected to the force of an actuator. Lastly, we conducted an assessment of friction forces on the bench and calibrated the sensors. Additionally, we determined the experimental stiffness of the spring by blocking one end and utilizing force and position sensors, while considering the known stiffness of the spring used in the setup.

In order to validate the experiment, we implemented proportional-integral (PI) force control on both linear actuators. The Moog E024 servovalve with a supply pressure of 10 MPa was used, with a proportional gain of $K_p = 1.5$ and an integrative gain of $K_i = 1.5$ for the hydraulic actuator. The mechanical setup resembled the one depicted in Figure 7, excluding the load car. The reference force signal consisted of a sine wave with an amplitude of 50 N and a frequency of 0.1 Hz. An example of the response of the encoder and load cells during one of the oscillations can be observed in Figure 26.

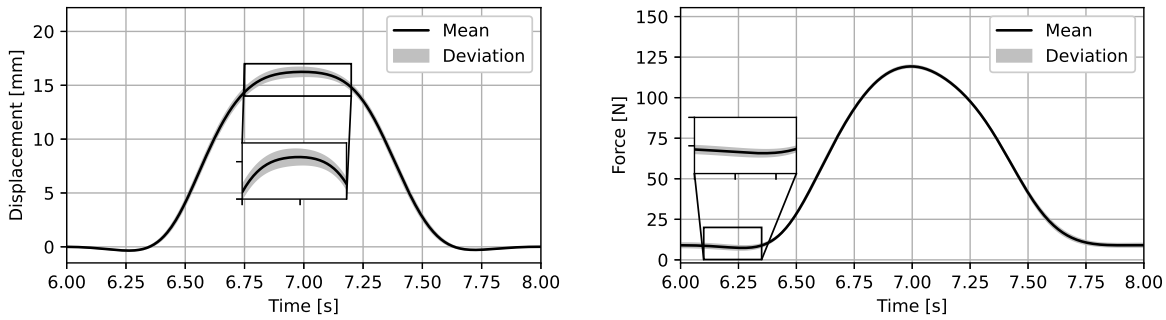

(a) Displacement (b) Force

Figure 26 – Hydraulic actuation system.

The procedure for the electric actuator was conducted in a similar manner. However, the values for the proportional gain (K_p) and integrative gain (K_i) were different, with K_p being 0.73 and K_i being 0.03. Additionally, the sine reference force had an amplitude

of 75 N and a frequency of 2.0 Hz. Figure 27 displays one of the oscillations observed in the obtained responses. Each actuator underwent the described setup ten times.

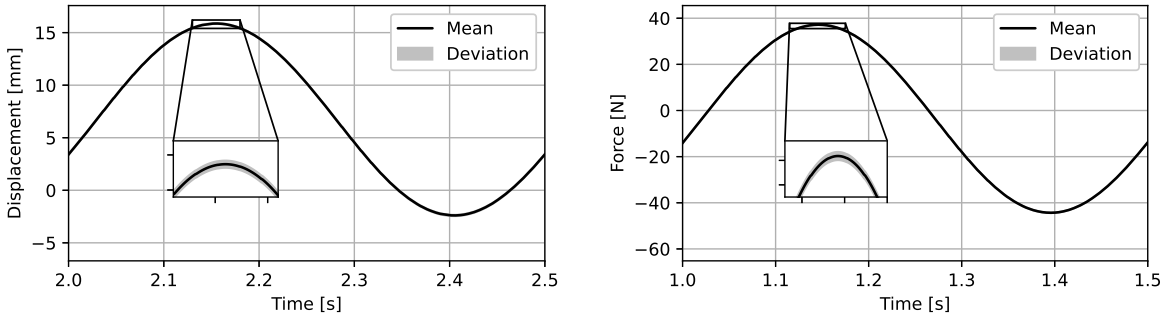

(a) Displacement (b) Force

Figure 27 – Electric actuation system.

The experiments assess the reproducibility of the bench for hydraulic and electric actuators in terms of their displacement and forces. The results obtained from ten experiments, as shown in Figure 26a for displacement and Figure 26b for force, indicate that the deviation and mean values are very similar. This suggests that the bench provides a valid qualitative and quantitative representation of the actual system.

Applying the electric actuator at its maximum operating force for a reference step signal, we obtained a displacement measurement of approximately 0.15 mm (Figure 28) when the actuator was blocked. This test was repeated ten times. It is evident that the displacement mainly arises from the deformation of the load cell. Consequently, we can deduce that this displacement is insignificant, thus confirming the objective of achieving an assembly with minimal backlash.

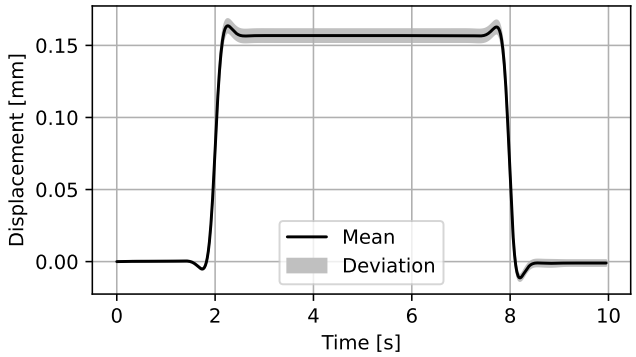

Figure 28 – Displacemnt mesured at the blocked set up.

In the third set of experiments, we conducted a manual compression of the spring. One end of the spring was blocked, while the other end had the linear encoder and force sensor attached. The experimental curves showing the relationship between force and

displacement are presented in Figure 29. The purpose of these experiments was to evaluate the impact of friction and sensor calibration.

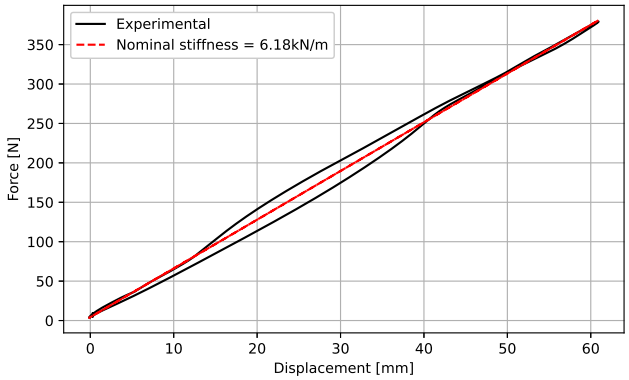

Figure 29 – Linear regression of the experimental spring stiffness.

By conducting a linear regression using the average of ten experiments and a correlation coefficient of $R_k = 0.9987$, the stiffness of the spring was determined to be 6.18 kN/m. The anticipated stiffness value was 6 kN/m. The detected variation can be ascribed to the friction between the sliders and the guide, as mentioned by Zanette et al. (ZANETTE et al., 2023). Additionally, the impact of viscous friction is particularly evident during the transition between the endpoints, where the movement velocity is more prominent.

4 FORCE CONTROLLERS REVIEW

The objective of this chapter is to present the dynamic models and force controllers employed in this study by reviewing articles, books, and other significant works. In order to implement controllers on the constructed bench, an investigation was conducted on the modeling of these actuation systems. The objective was to gain insights into the implementation of controllers and the expected response. The study focuses on the modeling of the actuation systems under examination: the DC motor, PMLSM, and hydraulic cylinder with servovalve. Additionally, the force controllers employed in this study will be presented and discussed.

4.1 Electric actuation system model

In this section, we will describe a model for a torque-controlled SEA DC motor and a model for a force-controlled PMLSM linear motor. This study used both types of electric motors.

4.1.1 DC Motor dynamics

The model of the torque-controlled SEA DC motor is created by assigning a transfer function to each part of the control loop, as shown in Figure 30.

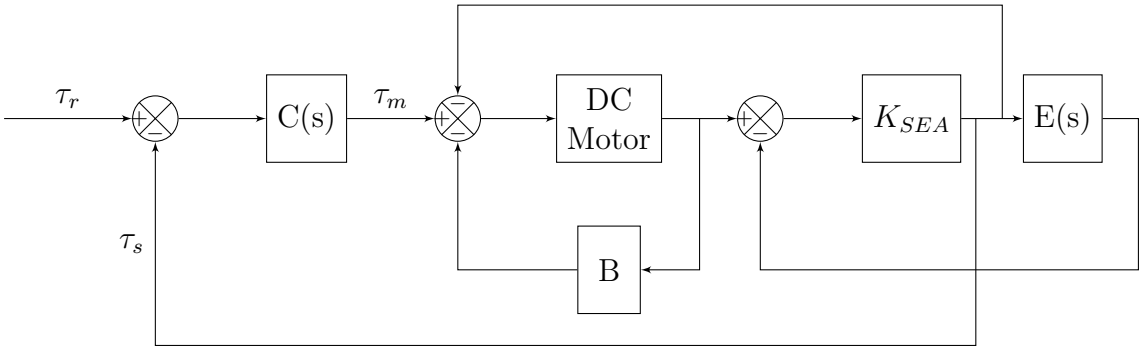

Figure 30 – Block diagram of the DC Motor torque control loop

The block *C(s)* is the controller, which will be further developed in the next sections. The block *DC Motor* represents the dynamics of the DC motor with rotor inertia J_m. Its transfer function is:

$$DCMotor = \frac{1}{J_m s^2} \tag{4.1}$$

The block K_{SEA} represents the stiffness spring k_{SEA} that composes the series elastic actuator. Series elastic actuators (SEA's) are an emerging technology to achieve

high fidelity force control of high power density motors. In fact, series compliance can dramatically improve explicit force control robustness (PRATT; WILLIAMSON, 1995). Most of the applications of SEAs nowadays are based on impedance control and need to deliver forces with a high level of safety and accuracy. The block B represents the frictions present in the bench and in the motor, here represented by Coulomb and viscous friction. And finally, the block *E(s)* is the environment/load:

$$E(s) = \frac{1}{J_l s^2 + B_l s + k_l} \tag{4.2}$$

The load damping (B_l) is calculated from the following equation:

$$B_l = 2\zeta\sqrt{J_l k_l}\ , \tag{4.3}$$

where k_l is the stiffness of the load, ζ is the damping coefficient of the load and J_l is the inertia of the load.

The block diagram was implemented at the Simulink software, as shown in Figure 31. In this block diagram, we have the force controller PID block, a function delimiting the motor torque, the SEA block, shown in more detail below, and the environment or load block.

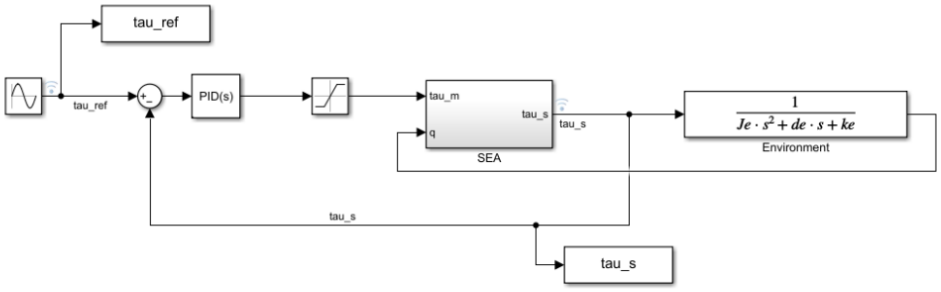

Figure 31 – Simulation of the bench

Figure 32 shows the inside of the SEA block, which contains the motor block, the applied frictions (Coulomb and Viscous) and the spring.

In table 1 below, all the parameters used in the simulations represented by the ForceCAST bench.

4.1.2 Linear Motor dynamics

The advantages of the precision motion system, which is powered by a permanent magnet linear synchronous motor (PMLSM), include high speed, high acceleration, and high positioning accuracy. However, the performance of the feed device may be affected by the PMLSM's ability to handle nonlinear and uncertain disturbances, such as cogging force,

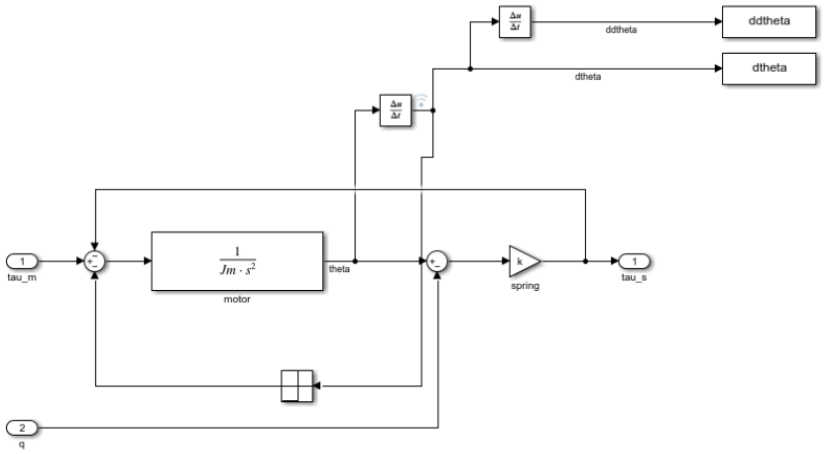

Figure 32 – SEA block of the simulation

Parameters	Value
Motor Inertia (J_m)	0.133 Kgm^2
Spring SEA (k_{SEA})	60 Nm/rad
Max Motor Torque (τ_{max})	0.5 Nm
Load Stiffness (k_l)	10 Nm/rad
Load Inertia (J_l)	0.001 Kgm^2
Load Damping Coefficient (ζ)	1
Coulomb Friction	0.5
Coefficient of Viscous Friction	0.01

Table 1 – Simulation parameters for the ForceCAST DC motor.

friction, thermal effects, residual vibration, and load disturbance. Typically, PMLSMs are three-phase, but the one used in this master's degree project is only two-phase. Therefore, we have adapted the model proposed by (YU et al.) for our specific application. The mechanical equation of the motor is represented by Equation 4.4.

$$F_e = m\ddot{x} + B\dot{x} + F_\Omega \tag{4.4}$$

Where F_e is the electromagnetic force (N), m is the mass of the actuator (kg), x is the position of the actuator (m), $\dot{x}$ is the velocity (m/s), $\ddot{x}$ is the acceleration (m/s^2), B is the coefficient of viscous friction (kg/s), F_Ω are lumped uncertainties (N). However, for a PMLSM with an external permanent magnet surface mounted, the electromagnetic force can still be defined by:

$$F_e = k_f i_q \tag{4.5}$$

Where k_f is the motor force constant (N/A) and i_q is the current on the q axis (A). Finally, combining 4.4 and 4.5, there is the dynamic equation expressed by Equation 4.6.

$$\ddot{x}(t) = k_1 u(t) + k_2 \dot{x}(t) + D(t) \tag{4.6}$$

where $u(t)$ is equivalent to i_q and k_1, k_2 and D are defined by:

$$k_1 = \frac{k_f}{m}, \quad k_2 = -\frac{B}{m}, \quad D(t) = -\frac{F_\Omega}{m} \tag{4.7}$$

The parameters used in this study were based on the LinMot datasheet and previous models developed for similar motors (JIN et al., 2010; WANG; FENG, et al., 2011).

Parameters	Value
Motor Force Constant (k_f)	17 N/A
Motor opposite Force Constant (k_m)	9 N/A
Motor internal resistance (R_m)	3 Ω
Mass of the actuator (m)	0.49 kg
Motor coefficient of Viscous Friction (B)	0.1 kg/s

Table 2 – Model parameters for the LinMot.

In this case, the consideration of lumped uncertainties was disregarded due to the intended use of this model in the implementation of force controllers, which requires a simplified model. Additionally, the identification of model parameters becomes a challenging task in the absence of identified bench frictions.

4.2 Hydraulic actuation system model

In this section, we will develop a model of the hydraulic actuation system, starting from fundamental principles such as mass and energy conservation. Our main focus will be on formulating mathematical equations that describe the force behavior of actuators, taking into account the interplay of various fluid dynamics equations. The dynamic response of hydraulic actuators can be effectively captured by a set of governing equations that are closely tied to fluid dynamics. To this end, we will break down the modeling process into three components: valve spool dynamics, pressure dynamics, and actuator force. For a more detailed explanation, please refer to (BOAVENTURA, 2013a; BOAVENTURA; SEMINI, 2020).

Due to the nonlinear dynamics of hydraulic actuated systems, controlling them is a complex task. Several researchers have explored different approaches to model-based impedance and force control. Boaventura et al. focused on designing an impedance controller that ensures overall stability and performance (BOAVENTURA; BUCHLI, et al., 2015). Kim proposed a control method using a deep neural network-based inverse model (KIM; CHO; SHIN, et al., 2021). Vorndamme enhanced the performance of the humanoid robot Atlas by applying observer-based disturbance compensation control with fault detection

and estimation methods (VORNDAMME et al., 2016). Chen initially proposed an adaptive robust force control for the joint-level of a hydraulic exoskeleton knee, and later extended it to an underactuated lower limb hydraulic exoskeleton (CHEN; CHEN, et al., 2016; CHEN; ZHANG, et al., 2022). Pasoli, on the other hand, presented a hybrid position-force control approach using a unified state feedback controller combined with feedforward dead-zone compensation. The experiments were conducted on a testbench with two opposing hydraulic cylinders (PASOLLI; RUDERMAN, 2019).

The electrohydraulic flow control servovalves have been the primary control mechanism for hydraulic actuation since the 80's (KONAMI; NISHIUMI, 2016). However, there is still a concern regarding the modeling and control of this type of servovalve, as discussed in the literature. To address this, Somashekhar developed a dynamic model of a two-stage servovalve with mechanical feedback, which was experimentally validated using finite element models (SOMASHEKHAR; SINGAPERUMAL; KUMAR, 2007). Nikiforuk developed a transfer function of sixth order to describe the relationship between the control voltage and load flow in a two-stage servovalve. This transfer function takes into account various factors such as motor coil impedance, flapper inertia, viscous forces, leakage flow, and the compressibility of the oil (NIKIFORUK; UKRAINETZ; TSAI, 1969). In the work by Rozali, system identification was employed to create a model for an electrohydraulic servovalve, which was then used to design a PID controller based on the model (ROZALI et al., 2010). Talib proposed a PID controller for automotive active suspension systems with hydraulic actuators. The controller was tuned using the Ziegler-Nichols method and an iterative learning algorithm (TALIB; DARNS, 2013).

4.2.1 Fluid properties

Mineral oil is widely used in robotics as a fluid due to its popularity. Its low compressibility enables faster and more efficient energy transfer. Moreover, the oil serves as a lubricant for circuit components like valves and cylinders, ensuring their long-term integrity and minimizing leakage. Nonetheless, the environmental risks and flammability associated with oil have prompted researchers to explore water-based fluid power transmission (YANG et al., 2009; GARY; PATRICK, 2004; HODGES, 1996). Water-based systems are currently being developed to achieve the same level of corrosion protection and leakage prevention as oil-based systems. The properties of the fluid, such as viscosity and compressibility, are influenced by the temperature and pressure of the system. The compressibility, which is measured by the Bulk modulus, increases with the system pressure. Additionally, the Bulk modulus decreases with an increase in temperature under the same pressure. It is important to understand these factors and their impact on the control system in order to ensure a stable and robust closed-loop response. In this physical model, the Bulk modulus was taken into account and described by:

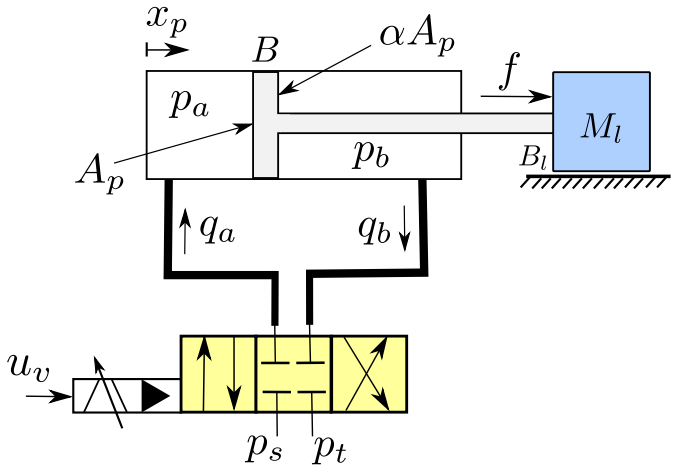

Figure 33 – A standard hydraulic diagram is presented, illustrating a cylinder controlled by a valve. The symbol used for the 4/3 DCV operator signifies a two-stage servovalve equipped with a hydraulic pilot. The spool position signal is denoted as u_v. The schematic also includes information about the system pressures and flow directions. Additionally, specific parameters related to the cylinder, such as the piston area (A_p) and the viscous friction coefficient (B), are indicated. The load, which has a mass of M_l and exhibits viscous friction (B_l), is depicted in blue. This diagram is an adaptation from the work of (BOAVENTURA; SEMINI, 2020).

$$\beta = -v_0 \left(\frac{\partial p}{\partial v} \right) \tag{4.8}$$

In this equation, v_0 represents the initial volume of the fluid that is confined, measured in cubic meters (m^3), and is subjected to atmospheric pressure. The term ∂v refers to a change in volume of the fluid when it is pressurized, also measured in cubic meters (m^3). Similarly, ∂p represents a change in pressure applied to the fluid, measured in pascals (Pa).

4.2.1.1 Valve spool dynamics

Proportional valves typically utilize solenoids driven by electricity to produce forces that move the spool in proportion to the current input signal u. The dynamics of the spool can be represented by a second-order linear system in mathematical modeling,

$$u = \left(\frac{1}{w_v^2} \right) \ddot{u}_v + \left(\frac{2D_v}{w_v} \right) \dot{u}_v + u_v \tag{4.9}$$

where w_v is the natural angular frequency of the valve spool, D_v is the damping of the valve spool, and u_v can be read as a low-pass filter version of the input u.

It is feasible to develop the equation that establishes the connection between the flow rate and the pressure drop, also known as orifice equations. The flow rates, denoted as q_a and q_b in Figure 33, can be represented as:

$$q_a = \begin{cases} K_v u_v \sqrt{p_s - p_a}, & u_v > 0. \\ K_v u_v \sqrt{p_a - p_t}, & u_v < 0. \end{cases} \tag{4.10}$$

$$q_b = \begin{cases} K_v u_v \sqrt{p_b - p_t}, & u_v > 0. \\ K_v u_v \sqrt{p_s - p_b}, & u_v < 0. \end{cases} \tag{4.11}$$

where p_a, p_b, p_s and p_t are respectivelly, the cylinder's chamber a pressure, the cylinder's chamber b pressure, the supply pressure and the tank pressure.

The valve gain K_v can be expressed in terms of the discharge coefficient C_d, the density of the oil ρ in units of kilograms per cubic meter (kg/m^3), and the area gradient W in units of square meters per ampere (m^2/A), as shown below:

$$K_v = \frac{C_d W \sqrt{2}}{\sqrt{\rho}} = \frac{q_n}{u_n \sqrt{\Delta p_{n_1}}} = \frac{q_n}{u_n \sqrt{\frac{\Delta p_{n_2}}{2}}} \tag{4.12}$$

However, it is easier to determine the valve gain using parameters from the datasheet (Table 3), such as the nominal flow rate q_n, the nominal pressure drop across one control edge Δp_{n_1} or Δp_{n_2}, and the nominal valve input u_n (A).

4.2.1.2 Pressure dynamics

The pressure dynamics of each actuator chamber can be determined by applying the mass conservation principle, assuming no external or internal leakage, and using the continuity equation.

$$\dot{p_a} = \frac{\beta_e}{v_a} \left(q_a - A_p \dot{x}_p \right) \tag{4.13}$$

$$\dot{p_b} = \frac{\beta_e}{v_b} \left(-q_b + \alpha A_p \dot{x}_p \right) \tag{4.14}$$

In this context, p_a and p_b refer to the immediate pressure of the actuator chambers labeled as a and b respectively. Similarly, v_a and v_b represent the instantaneous volume of these chambers. The effective Bulk modulus is denoted as β_e, while $\dot{x}_p$ represents the velocity of the piston. The variable A_p corresponds to the area of the piston, and αA_p represents the area of the piston-rod (or annular area), where α is a scaling factor that is less than 1.

The volumes of the chambers v_a and v_b change depending on the position of the piston x_p, which can be described as:

$$v_a = v_{pl} + A_p x_p \tag{4.15}$$

$$v_b = v_{pl} + (l_{cyl} - x_p)\alpha A_p \tag{4.16}$$

l_{cyl} represents the stroke length of the cylinder, which is the maximum distance the cylinder rod can travel. The calculation of the chamber volume should take into account the volume of the pipeline v_{pl} that exists between the valve and the actuator.

4.2.1.3 Actuator force

The hydraulic force f_h of the actuator is the force that arises solely from the pressure difference in its chambers, namely,

$$f_h = A_p p_a - \alpha A_p p_b \tag{4.17}$$

In robotics applications, the pressure in the circuit can reach levels exceeding 200 *bar*. To prevent internal fluid leakage, cylinders are equipped with seals. Consequently, it is necessary to incorporate non-negligible friction forces into the model. These friction forces, denoted as f_f, are typically simplified and modeled as static, Coulomb, and viscous friction (WATTON, 2009).

$$f = f_h - f_f \tag{4.18}$$

Due to the square-root correlation between flow and pressure drop, as demonstrated in Equations 4.10 and 4.11, and the friction forces f_f in the actuator, the model mentioned above is nonlinear. Nevertheless, to minimize the impact of these non-linearities, the decision has been made to linearize the model around a specific operating point of the system. This enables an examination and comprehension of its dynamics within the vicinity of that particular point. Additional information can be found in (BOAVENTURA, 2013a) and in Appendix A. Table 3 shows the parameters used to implement the control with the MOOG E024 valve.

4.3 Force Controllers

Force controllers are those that receive as input the error in the desired force and generate the control signal necessary for the plant. Here we will see PID control, PID added with velocity compensation for both linear actuators, and in the case of the electric linear actuator a disturbance observer was also implemented.

4.3.1 Force PID

The PID error feedback controller is by far the most popular controller, as it is simple and robust (LEVINE, 2018). The simple block diagram shown in Figure 34

Parameters	Value
Effective Bulk Modulus (β_e)	1.3 e^{+9} Pa
Piston diameter(D_p)	0.016 m
Rod diameter (D_r)	0.01 m
Cylinder stroke (l_{cyl})	0.08 m
Pipeline volume (v_{pl})	1.21 e^{-3} m^3
Nominal valve input (u_{v_n})	0.01 A
Nominal valve pressure drop (Δ_{pn})	70 e^{+5} Pa
Nominal valve flow (q_n)	1.25 e^{-4} m^3/s
Valve spool frequency (ω_v)	250 Hz
Valve spool dampinng (D_v)	0.5

Table 3 – Parameters for the hydraulic actuation system with the E024 MOOG valve.

illustrates the feedback control of the force from any plant dynamics.

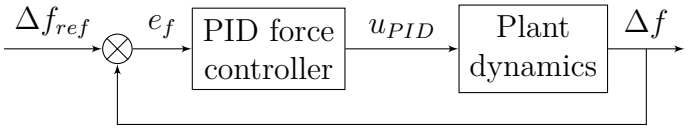

Figure 34 – PID Force controller closed loop.

As tuning was not a study objective in this work, controller gains were selected based on the behavior observed in the experiments, the general idea was to have a fast response without much overshoot. The output of the PID error feedback controller u_{PID} controls the valve according to the following control law:

$$u_{PID} = e_f \left(K_p + \frac{K_i}{s} + K_d s \left(\frac{N_d}{s + N_d} \right) \right) + \Delta f_{ref} \tag{4.19}$$

where e_f is the force error, K_p the proportional gain, K_i the integral gain, K_d the derative gain and N_d the derivative filter coefficient. When conducting experiments on benches, it is worth mentioning that typically, the control law for electric motors is combined with the reference signal (Δf_{ref}). This allows the motor to track the reference by adjusting based on the error. In the case of hydraulic actuators, if the error approaches zero, the valve should remain fixed in its position. Therefore, in the hydraulic actuators studied in this context, the reference signal combined to the control's law should ideally be zero. Therefore, the term highlighted in the equation above will only be used in electric actuators.

4.3.2 Load velocity compensation + PID controller

The principle of causality necessitates the use of a deformable or compressible transmission element to control force. This compliant transmission element acts as the medium through which force is transmitted from the actuator to the load. By utilizing

fundamental principles of physics, it is shown that this framework, comprising of a velocity source, a transmission, and a load, can effectively model the force dynamics for different types of force-controllable actuators (BOAVENTURA, 2013a).

The force that is transferred from the actuator to the load is affected by the dynamics of both the load and the actuator. The ability of feedback controllers to control the force and track its performance is restricted by the dynamics of the load. To surpass this restriction, a feedforward control signal based on the velocity of the load can be employed (ALLEYNE; LIU, 1999; BOAVENTURA; FOCCHI, et al., 2012).

When a spring mass system is moving, there is a built-in velocity feedback in the model that can result in performance problems. The force dynamics are influenced by the properties of the actuator, transmission, and load. This interaction occurs irrespective of the specific actuator or load being utilized. Figure 35 illustrates a simple mechanical system.

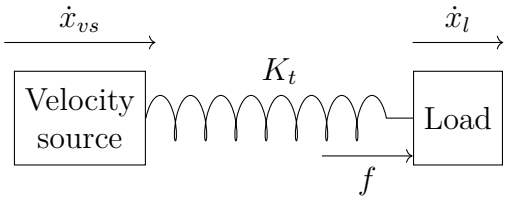

Figure 35 – Basic mechanical system composed of three basic elements: an actuator, represented by an ideal velocity source; a transmission with stiffness K_t; and a generic load.

Springs, being impedances, have velocity as their input and force as their output in terms of dynamics. On the other hand, masses, being admittances, have force as their input and velocity as their output in terms of dynamics (HOGAN, 1984). In Figure 35, the velocity source v_s is a mass that is accelerated by an external actuator and has an instantaneous velocity x_{vs}, which is then transmitted to the transmission spring. The output force of the spring, denoted as f, acts on the load mass, which is also accelerated and has an instantaneous velocity x_l. The dynamics of the load force, represented by $\dot{f}$, can be expressed as:

$$\dot{f} = K_t(\dot{x}_{vs} - \dot{x}_l) \tag{4.20}$$

In block diagram form:

The relationship between force and load dynamics is an essential aspect of force physics, and it remains unchanged regardless of the actuation and load characteristics. Mathematically, this relationship can be represented as load velocity feedback, as shown

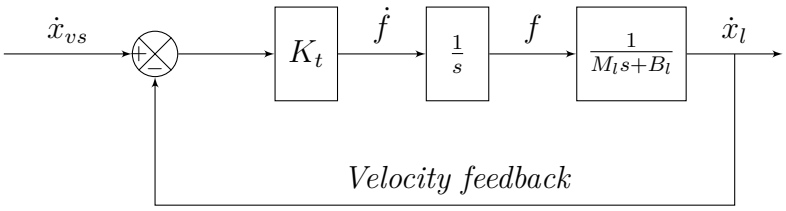

Figure 36 – A block diagram is presented to illustrate the functioning of a velocity source, which is exerting an effect on a load by means of a transmission stiffness denoted as K_t. It is evident that the load velocity, denoted as x_l, is being utilized as feedback in the dynamics of the load force.

in Figure 36. By considering M_l as the mass and B_l as the damping of the load, we can derive the following transfer function:

$$\frac{f}{\dot{x}_{vs}} = \frac{K_t(M_l s + B_l)}{s(M_l s + B_l) + K_t} \tag{4.21}$$

By examining Figure 36, it becomes evident that the pole of the load dynamics is also present as a zero in the force transfer function specified in Equation 4.21. This observation holds true, irrespective of the speed of the actuation dynamics (DYKE et al., 1995). Consequently, when a force control loop is closed, the controller gain and system performance are both constrained by the frequency of this zero. The subsequent sections elaborate on the implementation of a load velocity compensation term, which is incorporated into the force controller for two distinct actuation systems.

4.3.2.1 Hydraulic actuation system

In a hydraulic system, the implementation of this feedforward control involves adding an additional desired flow q_{ex} to the servovalve. This can be observed from the linearized model.

$$q_{ex} = A_{e\oslash}\Delta\dot{x}_p \tag{4.22}$$

thus, the valve input, considering the hydraulic force control, is:

$$u_{VC} = K_{VC}\frac{A_{e\oslash}\Delta\dot{x}_p}{K_{qe}} \tag{4.23}$$

The system block diagram applying velocity compensation with the feedback controller is show on Figure 37.

Additional information regarding the necessary parameters to execute this controller can be located in the Appendix A. In practical situations, it is important to recognize the distinction between the model and the actual system. As previously stated, the

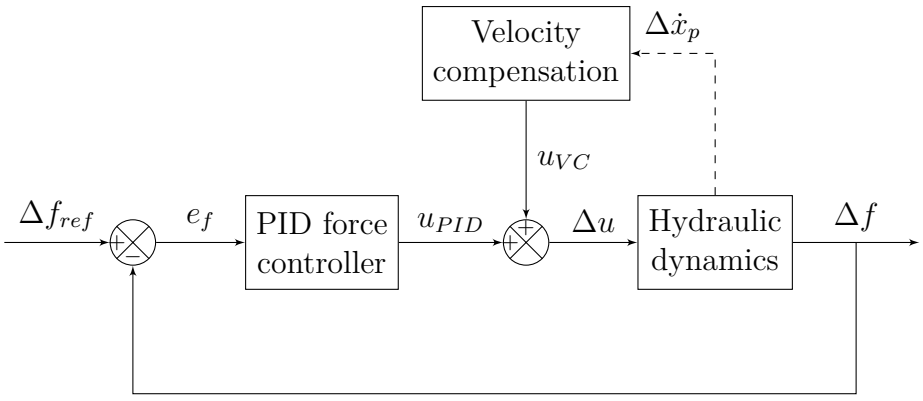

Figure 37 – PID + velocity compensation force controller closed loop for the hydraulic dynamics.

model parameters have not yet been completely determined and verified. To rectify these disparities between the model and the real system, a gain K_{VC} was employed. This gain multiplies the control signal derived from velocity compensation.

4.3.2.2 Linear electric actuation system

Similarly to the hydraulic system, as here the control signal is a current sent to the motor, this compensation will be an additional term in the current control signal, as shown in Figure 38.

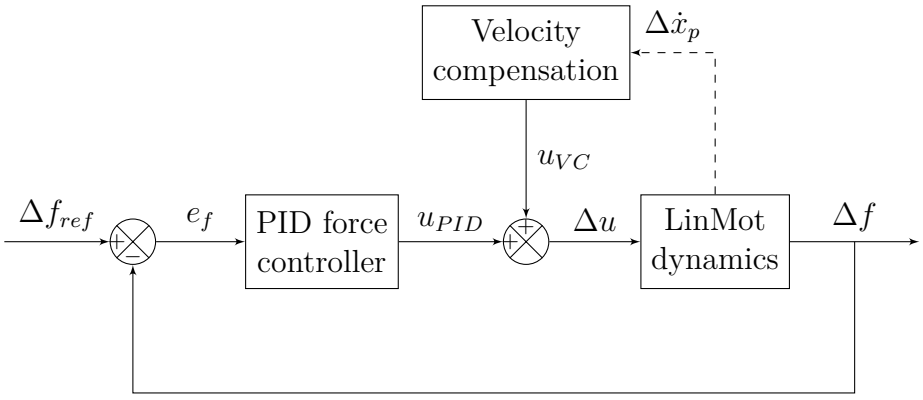

Figure 38 – PID + velocity compensation force controller closed loop for the LinMot dynamics.

Thus, the compensation drive input, considering the force control and the LinMot dynamics, is:

$$u_{VC} = m\ddot{x} + B\dot{x} + \frac{k_f k_m \dot{x}}{R_m} \tag{4.24}$$

Where m is the mass of the actuator, B is the motor coefficient of viscous friction, k_f is the motor force constant, k_m is the motor opposite force constant and R_m is the

motor internal resistance, all the values used are in Table 2. As for the previous cases, the torque transfer function has a zero due to the load dynamics. All the poles (one real and two complex) depend on both load and motor parameters.

4.3.3 Disturbance Observer Based controller (DOB)

The disturbance observer (DOB) is a control technique proposed by Ohnishi et al. (1996) that is used to estimate external disturbances and uncertainties in a system (OHNISHI; SHIBATA; MURAKAMI, 1996). To enhance system robustness, the DOB incorporates an inner feedback loop that feeds back the estimated disturbances, which include system uncertainties.

The system achieves performance goals by utilizing an external feedback loop controller that is designed independently, considering only the nominal plant model. This is done to normalize the inner-loop using a disturbance observer (DOB) (UMENO; HORI, 1991). In the literature, this control structure is known as two-degrees-of-freedom control (OHISHI; MIYAZAKI; NAKAMURA, 1995).

To design a disturbance observer (DOB), it is necessary to have a low pass filter (LPF) and the inverse of a nominal plant model. The low-pass filter (LPF) plays a vital role in maintaining causality in the inner-loop of the disturbance observer (DOB). Nonetheless, it can also impose limitations on the robustness and performance of control systems that utilize DOB (WANG; TOMIZUKA, 2004). Moreover, the use of the inverse of a nominal plant model may result in internal stability problems when the plant possesses non-minimum phase zero(s). Hence, special attention is required when implementing a DOB in a non-minimum phase plant (JO; SHIM; SON, 2010). The accurate estimation of disturbances by a DOB is widely acknowledged, as long as the disturbances are within the bandwidth of the DOB's LPF (KATSURA; IRIE; OHISHI, 2008). Therefore, it is desirable to increase the bandwidth of the DOB to effectively estimate disturbances across a wide range of frequencies, thereby improving both robustness and performance. However, the bandwidth of a DOB is limited by the system's robustness and the presence of noise, making it difficult to adjust freely (OHNISHI; SHIBATA; MURAKAMI, 1996; SARIYILDIZ; OHNISHI, 2013).

The robustness of a control system based on DOB is influenced by the dynamic properties of the LPF and nominal plant of the DOB. These properties also impose a restriction on the bandwidth of the DOB. However, the precise correlation between the robustness of a system and the dynamic characteristics of the DOB's LPF and nominal plant has not been adequately documented (CHOI et al., 2003).

Figure 39 shows a general control block diagram for a DOB based robust control system. In this figure, the $G(S)$ (*LinMot dynamics*) and $G^{-1}(S)$(*LinMot inverse dynamics*) denote the plant and the inverse plant models, respectively; the $Q(s)$ (LPF) is the low

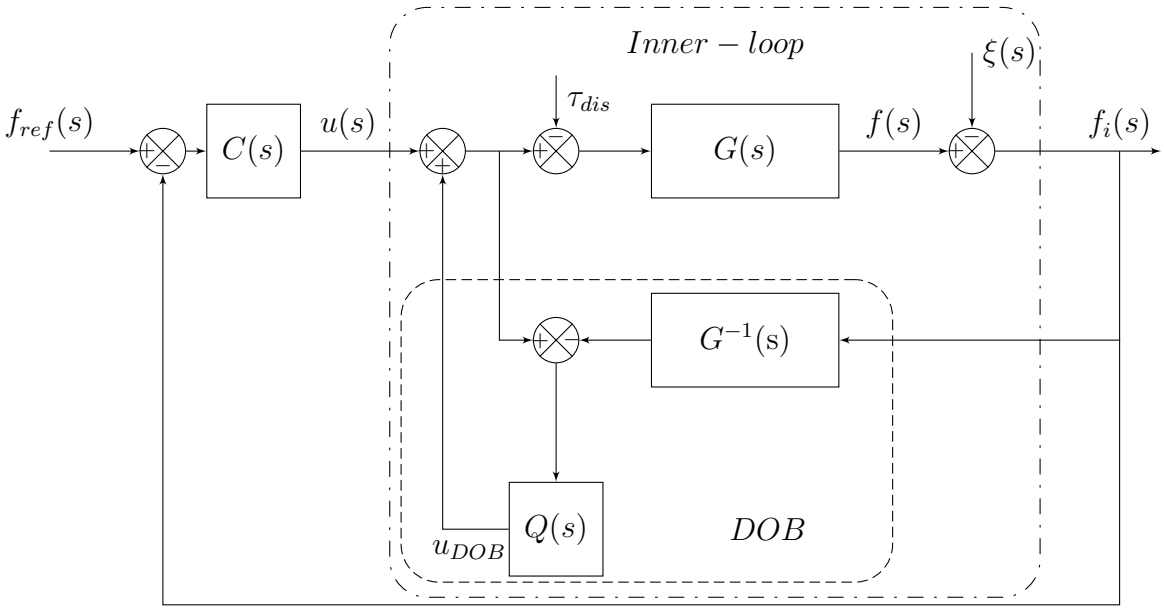

Figure 39 – A block diagram for a two-degrees-of-freedom DOB based robust control for the LinMot actuation system, addapted from (SARIYILDIZ; OHNISHI, 2014).

pass filter of a DOB; $C(s)$ denotes the outer-loop force controller; f_{ref} denote the reference force and f_i denote the interaction force, τ_{dis} and ξ are the disturbance and noise external inputs, respectively; and u_{DOB} denotes the contribuition of the DOB loop to the external force control loop, it estimates disturbances, which includes external disturbances and system uncertainties. Its value was estimated from the following equation:

$$u_{DOB} = Q(s)(u(s) - G^{-1}(f_i - \xi)) \tag{4.25}$$

For our experiment, we opted to incorporate a disturbance observer (DOB) into the LinMot system to evaluate its performance when considering bench friction as external noise (ξ). The LinMot dynamic model here applied was an simplification of the discussed model in a previous section of this chapter, only the motor constant k_f was used, and a first order butterworth low-pass filter with a frequency of 5 kHz was selected.

5 METHODOLOGY

This chapter presents and discusses the methodology to perform force controllers benchmarking with different actuation systems. As mentioned in the State-of-the-art (Chapter 2), there is no established methodology to analyze the performance of force-controlled systems. The main difficulty in its development is the influence of the environment dynamics. Attempts to experimentally test every possible combination are often unpractical and time-consuming. Therefore, a novel methodology will be presented in this chapter.

5.1 Force Control Benchmarking Methodology

Four general elements can fully describe the dynamics of a force-controlled system: a controller, an actuator, a transmission, and a load, as depicted in Figure 40 for a system with three different actuation systems: a DC motor, a PMSLM (Permanent Magnetic Syncronous Linear Motor) and an hydraulic cylinder.

Despite the controller, the other elements are mechanical subsystems that can be modeled as an impedance or an admittance (BOAVENTURA; FOCCHI, et al., 2012), as shown in Figure 41. Note that an impedance must be associated with an admittance for causality reasons and vice versa (HOGAN, 1984). The force and velocity of the interaction are defined at the boundaries between two subsystems. If the velocity is the input and the force is the output, then the system is modeled as an impedance. In the inverse case, it is modeled as an admittance.

The *load subsystem*, Figure 41c represents the body, which may include the robot link and any other coupled object, on which the actuator applies and controls an interaction force f_i. An external force f_{ext} can also influence the load dynamics. Its representation as admittance is the most natural choice, since the environment can be usually see as mass. Therefore, it will be modeled as an admittance Y_l (the Laplace variable s is omitted for simplicity), having as inputs the interaction force f_i and eventually an external force f_{ext}, and as output the interaction velocity v_i.

The *transmission subsystem* is present for two reasons: first, for causality consistency in the entire system; and the second, it is closer to the real system, since the actuator must have at least a force sensor between the environment and the actuator. The transmission, Figure 41b, represents the most compliant elements in the chain and usually includes force sensors (e.g., a load cell) and/or elastic elements in the case of a Series Elastic Actuator (SEA) (PRATT; WILLIAMSON, 1995). Transmission inertia is often neglected, considering only its stiffness and eventually damping. Since it is connected to an admittance (the environment), this subsystem must be modeled as an impedance. Furthermore, the

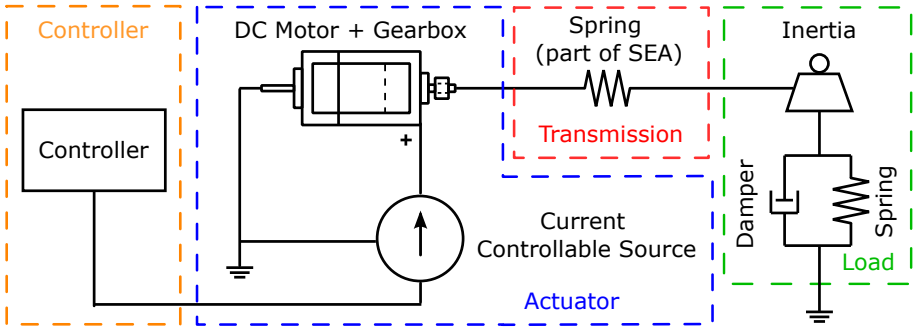

(a) DC Motor

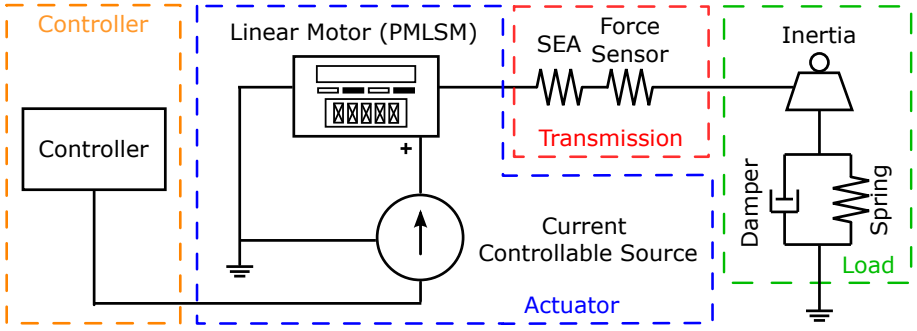

(b) PMLSM

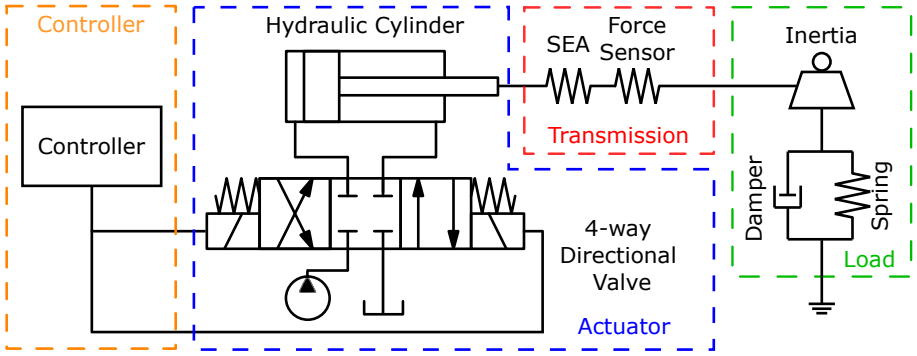

(c) Hydraulic cylinder

Figure 40 – Schematics of a force-controlled system driven by three different actuation systems.

system interacts with both the actuator and the environment. Thus, the transmission impedance must have the actuator velocity (v_{act}) as input. Consequently, it must also have the interaction force (f_i) as output.

The *actuator subsystem*, Figure 41a, acts as a source of velocity for the transmission impedance and is often considered a pure mass/inertia. Initially, the interest is on the velocity source (Y_a), it models the moving part of actuator. For example, in a hydraulic cylinder it is the cylinder piston, and in electric motors, the rotor. Again, since the velocity source is connected to an impedance (the transmission subsystem), it must be an admittance with the interaction force (f_i) as one of the inputs and the actuator velocity (v_{act}) as the output. The actuator is accelerated by a driving force f_d proportional to the command from *controller*. The block P_a in Figure 42 represents the dynamics responsible for converting the control input into the driving force f_d, for example, the valve and fluid

dynamics in hydraulics, and the electric dynamics of the motor driver and stator circuit in electric motors.

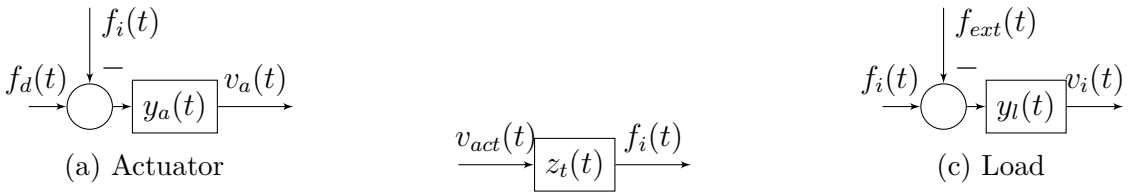

(a) Actuator

(b) Transmission

(c) Load

Figure 41 – Block representation of the mechanical subsystems of a force control system. The actuator and load are modeled as admittances, while the transmission is modeled as an impedance.

When the whole system is operating in closed loop, the three subsystems actuator, transmission, and load are connected as shown in Figure 42. There is one additional block (C) that is the controller.

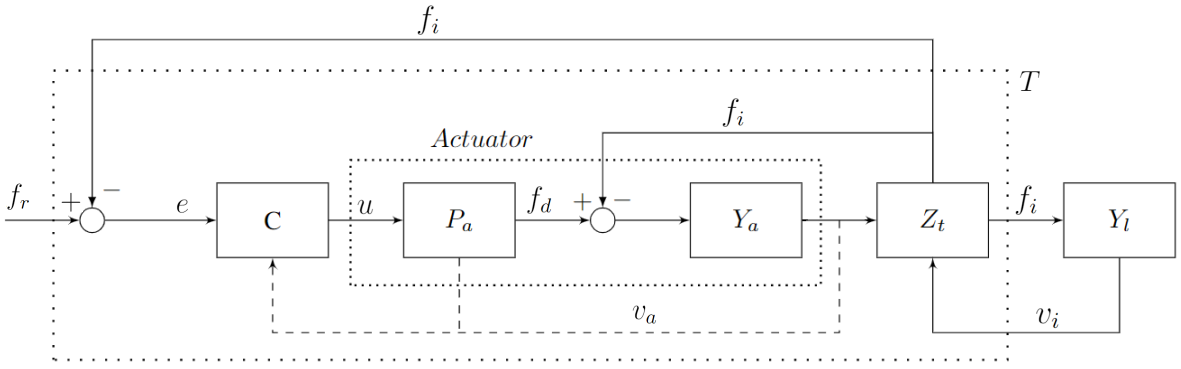

Figure 42 – Interaction with closed-loop force control

5.1.1 Force control modeling framework

The closed-loop force control can be represented by the block diagram in Figure 42. This block diagram can be simplified by grouping all the blocks that represent the dynamics of the controller, actuator, and transmission into a single block T (the Laplace variable s is again omitted for simplicity). These are the subsystems that are subject to design choice, since the load is, in most cases, unknown beforehand. The controlled actuator is the overall system T, divided into two subsystems: tracking (T_t) and apparent impedance (T_i). These functions already represent the behavior with closed-loop control. The load is represented by the admittance Y_l. Note that both T_t, T_i, and Y_l do not necessarily need to be linear, but if they are the coupled response is then defined by the transfer function:

$$\frac{F_i(s)}{F_r(s)} = \frac{T_t(s)}{1 - T_i(s)Y_l(s)} \tag{5.1}$$

On one hand, the block T_i comprises the dynamics related to *load motion*, having the load velocity v_i as input. On the other hand, T_t includes the dynamics of the *blocked* system, i.e. it is not affected by the load motion. For example, when the load is a rigid wall, $v_i = Y_l \times f_i = 0$ for any force f_i.

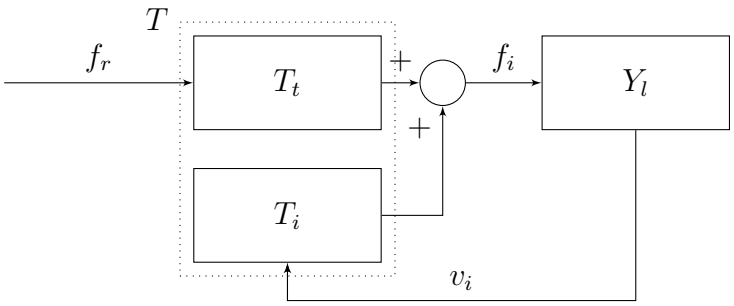

Figure 43 – Interaction model. The three signals are the reference force (f_r), the load interaction force (f_i), and velocity (v_i).

Therefore, the problem of analyzing the influence of the load on the dynamics of the force control can be reduced to a system identification problem, as the response of the coupled system to an *arbitrary* load can be predicted if T_t and T_i are known.

Regarding the linearity assumption, it is not as restrictive as it may initially seem when the system is in a closed loop, as non-linear effects tend to be minimized by the controller (PINTELON; SCHOUKENS, 2013). Thus, the linear approximation of T by T_t and T_i can satisfactorily capture the behavior when the system is closed loop.

Considering this approach the benchmarking methodology proposed is the one presented on the diagram on Figure 44.

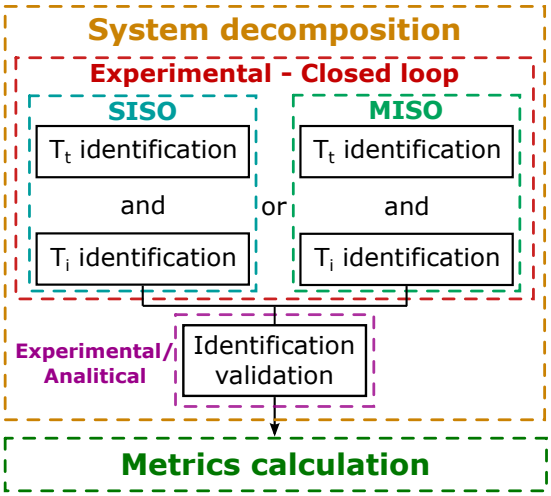

Figure 44 – Benchmarking Methodology Fluxogram

5.1.2 System Identification

To identify the transfer functions T_t and T_i, it is necessary to adequately generate the input and output signals for each system. These systems can be identified individually by

two SISO systems or simultaneously by one MISO system. Each approach has its advantages and disadvantages. In this section, we will describe how to do these identifications while we present its application in the ForceCAST bench, in order to better exemplify and indicate the difficulties and benefits of the methodology.

The identification of systems from experimental data is not a very trivial task, therefore, regarding the identification several questions were raised during the process, so a controller was chosen as the reference one and a more detailed study of the identification is presented in this section. The PD force controller ($K_p = 15$ and $K_d = 0.5$) was considered the reference controller for being the one with the best performance in general on the bench. Initially, for the identification, we also defined a standard load, this load was commonly simulated on the bench, i.e., a virtual load with good accuracy. Therefore, the reference values are $k_l = 10\ N.m/rad$, $\zeta = 1$ and $J_l = 0.001\ Kg.m$.

The first identification methodology applied was the MISO one, as the bench did not have a simple way to carry out the SISO identification, since blocking the actuator was not something foreseen in the bench design. However, an attempt at the SISO identification will also be made, but in a second moment.

5.1.2.1 MISO identifications

This identification uses only one experiment attached to an arbitrary load, as shown in Figure 40. The reference force, interaction force and interaction velocity signal are logged and their data are used by a MIMO system identification algorithm. The reference force and interaction velocity are the inputs of the MIMO and the interaction force is the output. MIMO identification algorithms are more complex and as not as easily available as SISO ones. However, only one experiment is required. The load does not need to have a specific admittance, it does not even need to be linear, even if the identified system T is. However, it cannot be too stiff so that the velocity signal is still measurable. It can not also be to soft, because some force controllers become unstable when coupled with soft loads.

For the MISO identification, considering the reference load, a sweep was applied with a frequency from 0 to 20 Hz in 20 s with an amplitude of 0.4 Nm. To avoid bench variables that could lead to poor repeatability of the tests, it was decided to run each experiment at least ten times and to use at least five that were most similar. The identification algorithm was then applied to the obtained data. As the function used to estimate the transfer functions is Matlab's *tfest* function, we performed the identification of T_t and T_i, from six tests and the merge data of these tests, the transfer function bode diagrams obtained are presented in Figure 45.

Henceforth, we performed the algorithm again, with the same method of data merge for the MISO identification, for the same controller but coupled to different loads.

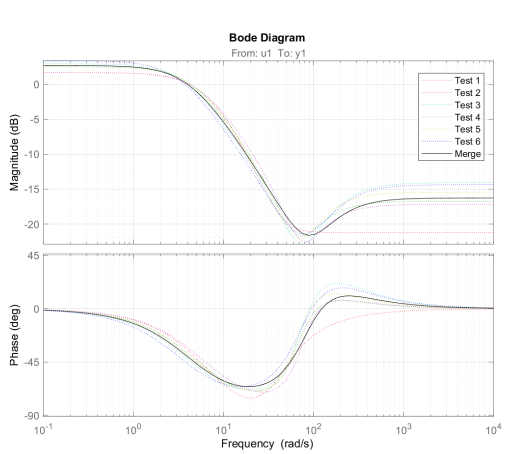

(a) T_t bode plot

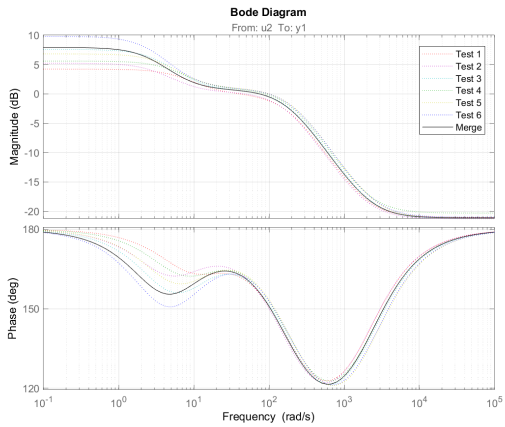

(b) T_i bode plot

Figure 45 – MISO identification using merged experimental data

As identification is independent of the load, this would be a way of confirming such a premise. The bode diagrams shown in Figure 46 were the results.

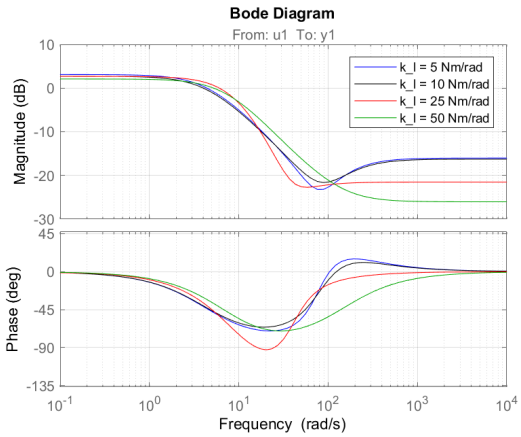

(a) T_t bode plot

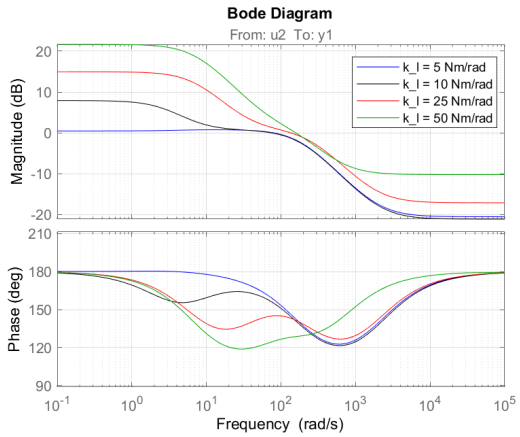

(b) T_i bode plot

Figure 46 – MISO identification using merged experimental data, with load stiffness variations

The curves, in general, are very close even when varying the loads' stiffness; the differences observed here may be due to the admittance control used to create the virtual loads. However, these differences are greatest in the identifications of T_i, the transfer functions that represent the transparency of the system, as can be seen in Figure 43. As transparency is more observable at low frequencies, the MISO identification was not very sensitive to it. Since for T_t the bode is expected to have a magnitude drop at a given cut-off frequency and for T_i a magnitude increase is desired, and these behaviors are only confirmed for T_t. Subsequently, the SISO identification will be performed to further deepen the analysis.

5.1.2.2 SISO identifications

The SISO identifications require an experiment for each transfer function. Since the system analyzed is a MISO, it is necessary to reset the input not relevant to that specific transfer function. That is, $v_i = 0$ when T_t is being estimated and $f_r = 0$ when T_i is being estimated. To identify T_t, is necessary to reset the interaction velocity, by blocking the actuator (Figure 47a), and to identify T_i, it is necessary to reset the reference force of the controller and measure the interaction force after inputting an input signal at the end of the actuator (Figure 47b). The input and output signals are then used by a SISO system identification algorithm to estimate T_t and T_i. This method is more common, so the algorithms to estimate the transfer functions will have better results, and there are no need to implement any load. However, this method assumes that the system T has a high level of linearity.

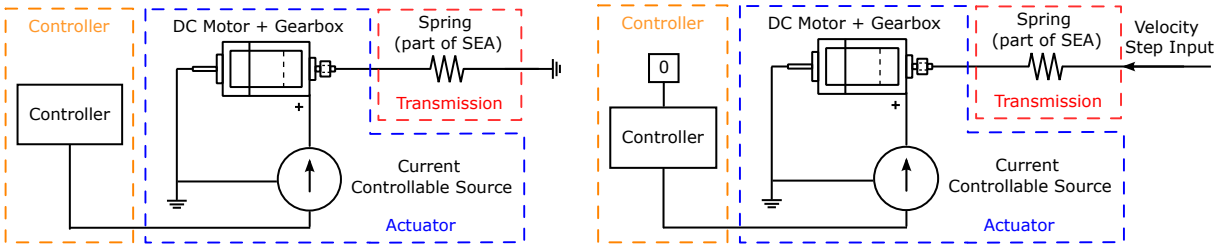

(a) T_t identification experimental set up (b) T_i identification experimental set up

Figure 47 – Schematics for the SISO identifications.

For the SISO identification, we start with an attempt to block the actuator, uncoupling the motor that emulates the virtual loads and locking the coupling with a steel bar. Then, an amplitude step of 3 Nm was used, and the procedure of performing ten tests and data merging was repeated. However, this blocking was not completely rigid, as one can see in the bode diagrams in Figure 48 for the transfer function T_t. To identify T_i, we performed a standard transparency test, placing a null reference in the force controller and a sinusoidal position signal for the actuator to follow, always measuring the residual interaction torque.

Only with the SISO identification from the transparency test we obtained a profile of the Bode diagram for T_i that was closer to the expected one, seeing the behavior of the bench with the increase in frequency in the transparency test. Therefore, the next step was to compare all identified transfer functions and validate them by comparing them to experimental data and simulations to verify whether or not the proposed methodology is plausible.

5.1.2.3 Identification validation

Once T_t and T_i are identified using the above system identification methods, it is recommended to validate them by comparing the response of the identified system and the

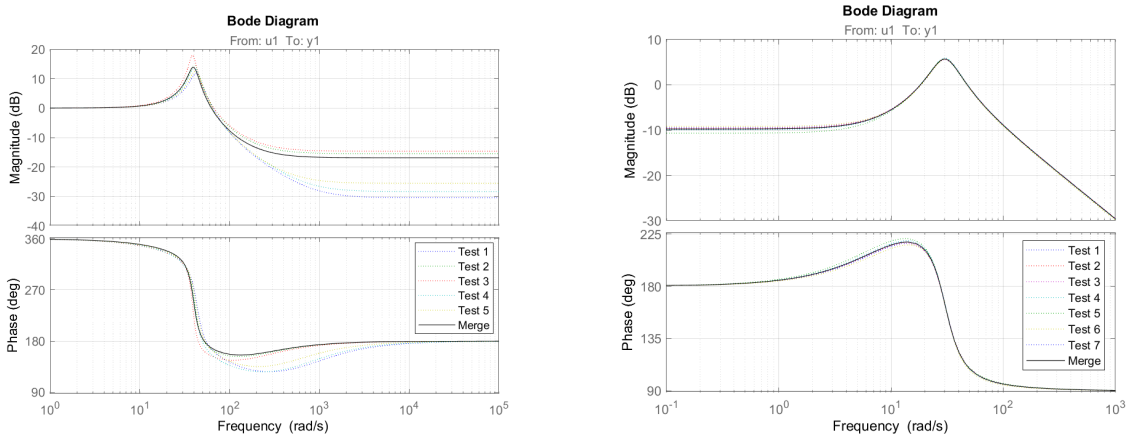

(a) T_t bode plot (b) T_i bode plot

Figure 48 – SISO Identification using merged experimental data.

real system, through experiments and/or simulations. In Figure 49, the functions identified in four different ways are shown.

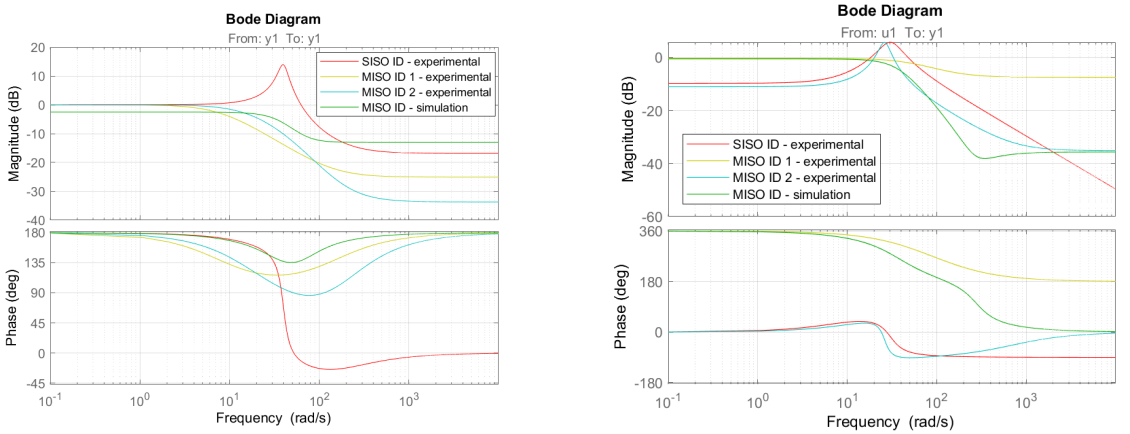

(a) T_t bode plot (b) T_i bode plot

Figure 49 – Bode diagrams of the identified transfer functions.

The SISO identifications are the same as those shown in Figure 48, while for the MISO, we used several tests on the bench with different inputs, steps, ramps, sine, sweep, totaling a data merge of more than 200 experiments. The difference between the MISO 1 and the MISO 2 identification is that within the data merge of MISO 2, transparency tests were also inserted. The simulation transfer functions were obtained from the Simulink block diagram output data, the model implemented was the one presented in Section 4.

We see that for T_t, only the SISO identification differs a little more, precisely because the test is not completely blocked. Regarding T_i, only the curves that had a share of transparency showed better results. The simulation curves, being MISO identifications, were also subject to misidentification of the transparency transfer function. And because the simulation contains few elements of friction and dynamics of the drives and sources of

the motors, naturally it differs a lot from the experimental ones.

To validate identifications, transfer functions were coupled to the standard load that forms the closed loop of Figure 42, which in turn was subjected to a step and a sine, and compared to the responses of simulations and experiments. Since the coupling of the MISO systems became unstable, we propose a hybrid coupling, that is, in the absence of the possibility of making the SISO identification correctly, we propose to make the MISO identification to obtain T_t and the SISO identification of the transparency to obtain T_i. By doing this, we had a response that was closer to what we wanted as a whole and proved to be an alternative that allows the application of the methodology in different experimental frameworks, as shown in Figures 50a and 50b.

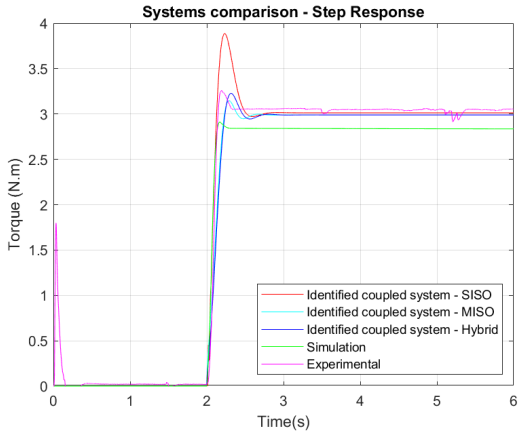

(a) Step response to the closed loop

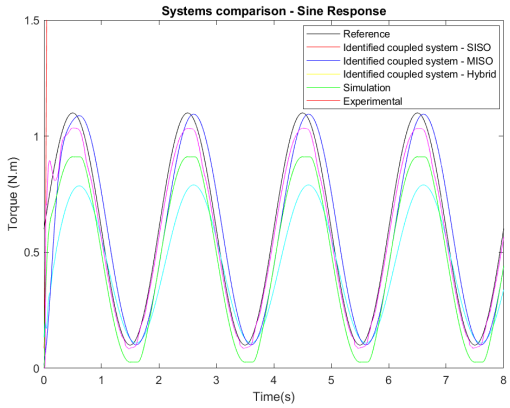

(b) Sine response to the closed loop

Figure 50 – Identification validation.

With the validation completed, the next step was to apply the same identification methodology to the other controllers, that is, the hybrid identification methodology, which proved to be the one with the best result for the ForceCAST bench.

5.2 Metrics

The benchmark metrics normally proposed depend on the coupling with the loads, especially when analyzing the experimental responses. Therefore, our methodology will have a different approach to calculating metrics. We propose load-independent metrics for the two identified transfer functions T_t and T_i.

5.2.1 T_t metrics

For the tracking system (T_t), the metrics employed include the classic control parameters: overshoot, rising time, settling time, and bandwidth. These are standard metrics in control theory, but nevertheless, are defined better next.

5.2.1.1 Rise time, settling time and overshoot

The rising time (t_r) is the time taken for the response to rise from 10% to 90% of the steady-state value. The settling time (t_s) is the time required for the response $f_i(t)$ to reach and stay within a range of a certain percentage (e.g., 2%) of the steady-state value f_s. The maximum overshoot (o_s) is the highest peak f_{max} the response reaches, divided by f_s. (Equation 5.2).

$$o_s = 100\frac{f_{max} - f_s}{f_s} \tag{5.2}$$

5.2.1.2 Bandwidth

The bandwidth (ω_B) of a system can be defined as the range of frequencies that can pass through a system. For frequencies beyond the bandwidth, the system response is degraded. Usually, the bandwidth is the first frequency where the gain drops below 70.79% (-3 dB) of the value of the signal at zero frequency.

5.2.2 T_i metrics

Intuitively, a system is passive if it does not create energy. Mathematically, given a system with input $u(t)$ and output $y(t)$ a system is passive if there is a constant β such that, for any time t:

$$\int_0^t u(\tau)y(\tau)d\tau \geq \beta \tag{5.3}$$

If the system is SISO linear, it can be shown that the passivity of the system is equivalent to its phase being between $-\pi/2$ and $\pi/2$. A lot of common loads are passive systems, for example, any combination of a mass, spring and damper is passive.

According to Equation 5.1, the behavior of a force controlled system depends on the load. One of the initial inquiries is whether the force being controlled is consistently stable. If not, it is important to identify which loads can cause instability in the coupled system. For an arbitrary linear load, the answer is that for any $T_i(s)$, there is a load (not necessarily minimum phase or stable) that makes fixed output system unstable (any $Y(s)$ such that $Y(i\omega) = 1/T_i(i\omega)$ for some frequency ω).

However, if we restrict the load to be passive, then there is a sufficient condition on T_i that guarantees that the coupled system remains stable if it already has fixed output.

The condition proof is as follows, a load create instability if and only if $1 - T_i(i\omega)Y(i\omega) = 0$ for some frequency ω. Thus, to keep stability $T_i(i\omega)Y(i\omega) \neq 1$ for all frequencies. If a linear system is passive, then its phase is between $-\pi/2$ and $\pi/2$. If the phase of $T_i(s)$ is between $\pi/2$ and $3\pi/2$,then the phase of $T_i(i\omega)Y(i\omega)$ will never be zero

(phase of 1). Thus a sufficient condition to keep the stability with passive load is to require that $-T_i$ itself is passive.

Usually, only the magnitude of the transparency is analyzed. This result show that the phase is also important and should be taken into account. One intuitive way to understand this result and maintain the stability of the system is to consider that the residual force exerted by T_i should oppose the velocity of the load for the majority of the time.

The hypothesis that the load is an arbitrary linear admittance is too general to get practical results. It is useful to restrict the class of load. The assumption that the load is a passive system has a good balance between allowing for interesting results and still modeling loads commonly found in real applications.

However, we propose a novel set of metrics to assess apparent impedance (T_i): a passivity index, a stability margin derived from the gap metric (GEORGIOU, 1988) that can offer information on how close the coupled system is to become unstable. And lastly, the infinity norm gives a measure of the influence of the load on the response of T_i.

5.2.2.1 Passivity Index

The passivity index R (XIA et al., 2020), shown in Figure 54, provides a measure of the degree of passivity. For a linear SISO system H, being passive is equivalent to its real part being positive real. This condition can be also written as a small gain condition.

$$R_H(\omega) = ||(I - H(i\omega))(I + H(i\omega))^{-1}||, \quad \forall\omega \in \mathbb{R} \tag{5.4}$$

In the context of force control, we measure R_{-T_i}. If the maximum value of R_{-T_i} is greater than one, $-T_i$ is not passive (we choose $-T_i$ because of the positive feedback in the diagram of Figure 43). Although all controllers have the same maximum value, the frequency response of R_{-T_i} still provides information. Therefore we define a new metric P_b that is the magnitude of R_{-T_i} at the bandwidth frequency of the T_t associated with T_i.

5.2.2.2 Stability margin

The gap metric $\delta_\nu(Y_{l1}, Y_{l2})$ measures the distance between two systems Y_{l1} and Y_{l2}. In this case, the stability margin is selected to be $b(-T_i, 0)$ (remember that the admittance of a fixed wall is 0), which means that the force controller is stable for every load admittance Y_l such that $\delta_\nu(Y_l, 0) < b(-T_i, 0)$.The gap metric theory is explained in more detail in (SHIME; NETO; BOAVENTURA, 2023).

5.2.2.3 Infinity norm

According to equation 5.1, if $Y(s)$ is fixed and $||T_i(s)||_\infty ||Y||_\infty$ is much less than 1, then $F_i(s)/F_r(s) \approx T_t(s)$. That is the behavior of the controller is less sensitive to load influence. Therefore is $||T_i(s)||_\infty$ is used as a metric.

5.2.2.4 Transparency and Backdrivability gain

Transparency (F_t): For force controllers, transparency will represent the controller's ability to mask the dynamics of the actuator, such as its inertia and frictions involved. In this work, we propose to measure transparency by calculating the RMSE of the force response generated by a chirp velocity input, i. e. the residual force. Note that the transparency is defined by the transfer function T_i.

Backdrivability gain (κ_B): After calculating the transparency of the actuator with the controllers and without them the last one is used as reference transparency (F_{t_r}), a simple ratio between them for each controller, as shown in Equation 5.5, will indicate the backdrivability gain provided by the controller.

$$\kappa_B = \frac{F_{t_r}}{F_t} \tag{5.5}$$

6 RESULTS

According to the previously mentioned benches and the suggested benchmarking approach, the results obtained will be presented in the order in which they were achieved. First, it was essential to determine the transfer functions for the force-controlled systems. Subsequently, the metrics were calculated for three distinct actuators, each with different torque/force controllers. Lastly, a comparison was made among the actuation systems.

6.1 Systems identification

The identification process was conducted using the two experimental setups described in Chapter 3. To improve the identifications made, we added a function to the code that tested different orders for the identified functions, also varying the number of poles and zeros, aiming to find the best possible fit. In the case of the DC motor tested in ForceCAST, two controllers, PD and PID, were chosen. For IC2D, six controllers were tested for each actuation system. In the case of hydraulics, only the E024 valve was selected for the tests. Four variations of PID and two variations of PID with velocity compensation were tested. For the electrical actuation system, the same four variations of PID were used, along with one variation of PID with velocity compensation and one variation with disturbance observer based control (DOB). The main objective of this study was not to optimize the controllers, but rather to compare them. However, optimizing the controllers is crucial for improving overall performance. As a result, the evaluation of the findings is carried out using comparative and qualitative measures.

6.1.1 DC Motor - ForceCAST

The procedure of determining systems from experimental data was conducted as explained in Chapter 5. The force controllers that were examined are presented in Table 4.

	PD	**PID**
K_p	15	15
K_i	0	1
K_d	0.5	0.5

Table 4 – Force controllers - DC Motor

Due to the challenges of performing bench tests, the identifications were conducted using a hybrid approach, which combines the results from both MISO and SISO identifications. The Bode diagrams of the identified functions can be seen in Figure 51. The validation process involved comparing the identified functions with the experimental data, and the results are provided in Appendix B. The MISO identification technique used

sweep input tests, and the validation process involved comparing the response to step and sinusoidal signals.

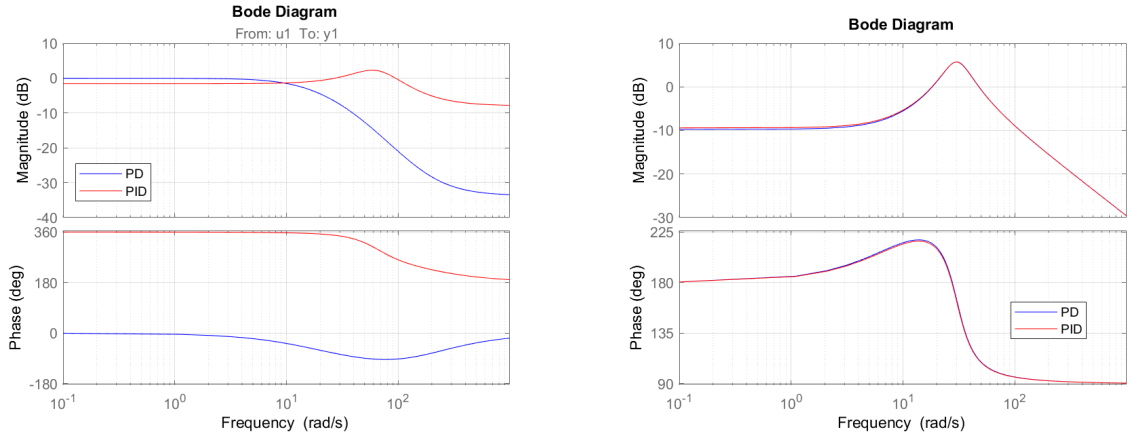

(a) T_t bode plot (b) T_i bode plot

Figure 51 – Systems identification using merged experimental data, bode plots showcasing the frequency response of (T_t) and (T_i) for the controllers implemented at the DC motor.

The functions found for T_i showed a significant level of similarity for both controllers. Regarding T_b, there was a slightly greater disparity, but despite the apparent difference in the phase diagram, one starts at 0 degrees while the other starts at 360 degrees, suggesting that they are more similar than they seem in the figure. Furthermore, they are similar across the tested frequency range.

6.1.2 LinMot

The identification procedure was replicated at IC2D, similar to the tests conducted at ForceCAST. The PID gains for the controllers employed are detailed in Table 5. The design of the controllers, including velocity compensation (VC) and disturbance observer (DOB), is explained in Chapter 4. To facilitate comparison, we retained the PID gain, despite it not necessarily being the most optimal controller in terms of performance. This was done in order to observe the effects caused by velocity compensation and DOB.

	P	**PD**	**PI**	**PID**	**PID + VC**	**PID + DOB**
K_p	1	1	1	1	1	1
K_i	0	0	0.2	0.2	0.2	0.2
K_d	0	0.03	0	0.03	0.03	0.03

Table 5 – Force controllers - LinMot

Nevertheless, since the bench was specifically designed to accommodate the suggested identification tests, including transparency and blocked actuator tests, both were performed. Additionally, MISO identification tests with sweep, sine, and step signals were

also performed. Ideally, it would be preferable to conduct transparency tests using a second actuator that provides a known velocity input to the system. However, due to the current state of the bench, it was not possible to connect two actuators simultaneously. As a result, transparency tests had to be performed manually, which somewhat compromised the quality of the results. The impact of this can be observed in Figure 52, where the functions T_t exhibit the expected behavior, while only the P, PD and PID + VC controllers show the desired trend of system transparency for the T_i functions.

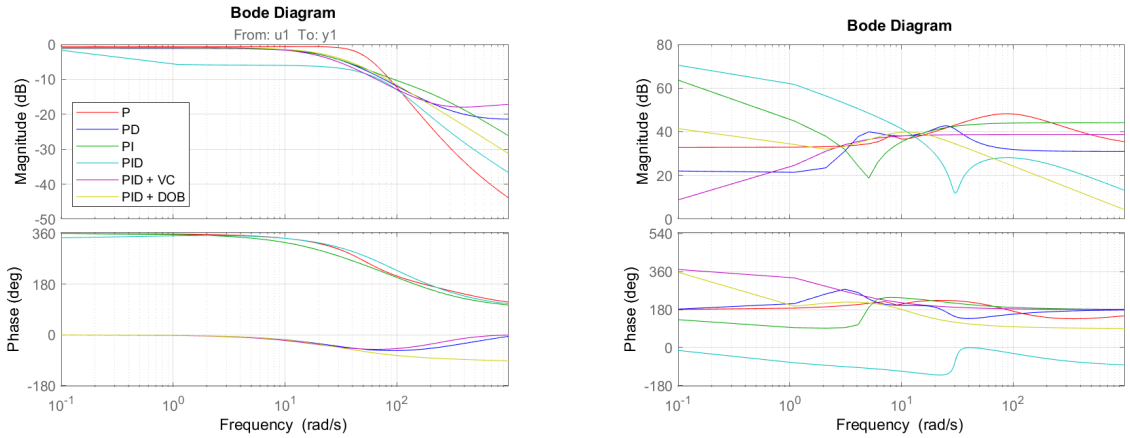

(a) T_t bode plot (b) T_i bode plot

Figure 52 – Systems identification using merged experimental data, bode plots showcasing the frequency response of (T_t) and (T_i) for the controllers implemented at the linear motor.

The validation figures for the sinusoidal and step response can be found in Appendix B. In the case of IC2D, the environment was identified considering that it was the same for all controllers, due to friction on the bench. The identified environments are also included in the same appendix. For the LinMot, mostly SISO tests were used for identification and were subsequently compared to experimental data, however, MISO identifications sometimes resulted in functions that improved coupling validation.

6.1.3 Hydraulic actuation system

In the hydraulic system, we incorporated two velocity compensators in addition to the variations of the PID controller. The main difference between these compensators is the value of the gain K_{VC}. For the compensator $VC1$, the selected gain was $K_{VC} = 1$, while for $VC2$, the gain was $K_{VC} = 1.5$. It is important to note that this gain can be used to correct any discrepancies between the model parameters and the actual system. The gains utilized for the PIDs are presented in Table 6. Similar to the approach followed in LinMot, the PID was employed as the reference controller for comparing velocity compensation.

In order to identify the functions depicted in Figure 53, we employed the hybrid method, similar to the approach used for the DC motor. In the blocked tests, the responses

	P	**PD**	**PI**	**PID**	**PID + VC1**	**PID + VC2**
K_p	0.01	0.01	0.01	0.01	0.01	0.01
K_i	0	0	0.01	0.01	0.01	0.01
K_d	0	0.00028	0	0.00028	0.00028	0.00028

Table 6 – Force controllers - Hydraulic cylinder

were oscillatory, an unexpected behavior, but as it is a non-linear system, it could be a limit circle. Also the Interface load cell, which has a much larger deformation than Burters, was used for these tests. This deformation may interfere on the response as well. The cell was not replaced because a calibration process was required, and since it was necessary to provide full scale of the load cell (5 kN) we did not had the rigth equipment. Due to this constraint, we used the flexibility of the methodology to perform tests with sweep input and determine T_t using the MISO test.

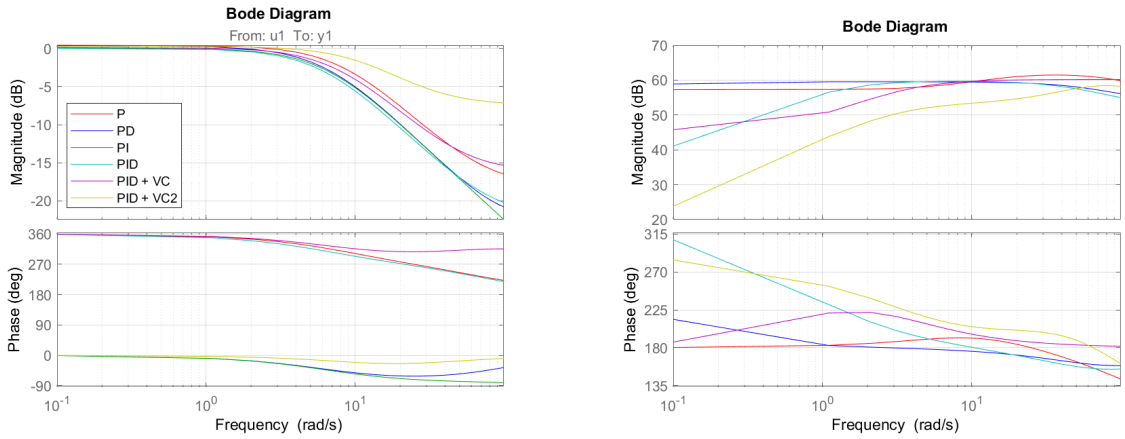

(a) T_t bode plot (b) T_i bode plot

Figure 53 – Systems identification using merged experimental data, bode plots showcasing the frequency response of (T_t) and (T_i) for the controllers implemented at the hydraulic actuation system.

We noticed that the T_t functions were very similar as desired and that the VC provided changes. In the phase diagram, the main distinction lies in how it is depicted, as all values begin at either 0 degrees or 360 degrees. To ensure transparency, the PD and PID controllers exhibited greater differences than anticipated in their behavior, possibly due to challenges similar to those in the LinMot identification procedure. The environments were also identified and can be observed in conjunction with the comparative responses using the experimental data in the Appendix B. Once the transfer functions have been determined, the subsequent task involves computing the metrics.

6.2 Metrics calculation

From the functions identified for the three force-controlled actuation systems studied, we calculate the metrics proposed by the methodology. The tables 7, 8 and 9 show the metrics calculated for T_t and T_i. The first four metrics are calculated using T_t with the usual definitions. The remaining three metrics are computed using T_i. A higher stability margin is more desirable, while a lower infinity norm and passivity index are also preferable. The passivity index is also visualized in Figure 54.

Metric (Unit)	**PD**	**PID**
Overshoot (%)	0	32.60
Rise Time (s)	0.143	0.017
Settling Time (s)	0.25	0.11
Bandwidth (Hz)	2.42	28.86
Stability Margin	0.4594	0.4605
Infinity Norm	1.93	1.92
Passivity Index R_b	0.5	0.32

Table 7 – Metrics for the DC motor force controllers

When comparing actuators, the integrative gain was observed to have a notable impact on response velocity, causing it to increase. However, this increase also led to a significant overshoot increase. Additionally, there was an increase in bandwidth, although it slightly affected the stability margin and resulted in a decrease in both the infinity norm and the passivity index. Generally, the metrics associated with T_i were more nuanced due to the similarity between the identified transfer functions. Specifically, the disparity in the passivity index can be attributed to the bandwidth discrepancy, as demonstrated in Figure 54a, where both values are quite similar.

Metric (Unit)	**P**	**PD**	**PI**	**PID**	**PID+VC**	**PID+DOB**
Overshoot (%)	4.805	0	0	0	0	0
Rise Time (s)	0.0407	0.0765	0.0877	11.5207	0.0930	0.0709
Settling Time (s)	0.1139	0.1369	0.1669	23.3271	0.1678	0.1263
Bandwidth (Hz)	8.4454	4.5947	4.3377	0.0322	3.7940	4.9213
Stability Margin	0.0039	0.0073	0.00044	0.00029	0.0116	0.0015
Infinity Norm	258.5	136.7	2272.6	3428.4	86.2	679.4
Passivity Index R_b	0.9923	1.0060	0.9991	inf	inf	inf

Table 8 – Metrics for the LinMot force controllers

In the case of the LinMot actuator, it was observed that the derivative and integrative gain had a negative impact on its performance. During the experiments, we noticed that the inclusion of the derivative component led to motor vibrations. On the other hand, the P controller exhibited improved velocity and bandwidth, albeit with

increased overshoot. The PID controller had the slowest responde and the highest rising time and settling time, the performance got much better with the addition of the velocity compensation or DOB term. Regarding the T_i metrics, it was previously mentioned that the transparency tests did not yield optimal identifications. Consequently, the metrics indicate systems with minimal stability margin and significantly high infinity norm values. Only the P, PD and PI controllers had passivity index values below 1. Figure 54b illustrates that only these three controllers exhibit a curve within the desired frequency range. Overall, the velocity controller (VC) for the LinMot significantly enhance performance compared to the proportional-integral-derivative (PID) controller as well as the DOB controller. Introducing a gain K_{VC}, similar to what was done with the hydraulic actuator, could potentially compensate for model uncertainties and enhance performance even more. Fine-tuning the DOB controller by removing the derivative gain , for example, adjusting the filter, or obtaining a more accurate understanding of the plant dynamics could greatly enhance its performance.

Metric (Unit)	**P**	**PD**	**PI**	**PID**	**PID+VC1**	**PID+VC2**
Overshoot (%)	0	0	0	0	0	0
Rise Time (s)	0.264	0.345	0.335	0.360	0.251	0.184
Settling Time (s)	0.469	0.617	0.596	0.644	0.463	0.330
Bandwidth (Hz)	1.337	1.013	1.040	0.973	1.239	2.324
Stability Margin	0.0008	0.0011	0.0010	0.0010	0.0010	0.0012
Infinity Norm	1183.5	946.2	1021.0	961.9	1021.0	833.6
Passivity Index R_b	1.00	inf	0.998	inf	0.998	inf

Table 9 – Metrics for the hydraulic cylinder force controllers

Initially, it is observed that the determination of T_t for the hydraulic actuators might have been hindered due to the lack of blocked tests. This is because the metrics do not show any overshoot, but the load cell on the bench deformed enough to produce oscillatory responses indicating controller overshoot. This can also be seen in the identification validation figures in Appendix B. Nevertheless, as intended, the velocity controller (VC) enhanced the system's responsiveness, particularly in comparison to the proportional-integral-derivative (PID) controller. Interestingly, when the gain K_{VC} deviated from 1, a significant enhancement was observed, resulting in a wider bandwidth. Surprisingly, the VC with a unity gain exhibited the lowest passivity index overall, as depicted in Figure 54c. Additionally, VC2 demonstrated the lowest infinity norm and, consequently, the highest stability margin.

The transparency measurements were obtained from both the experimental trials conducted on the bench and the transfer functions T_i that were identified. However, only the ForceCAST data allowed for the calculation using the experimental data, as the velocity inputs were known and equal. Since it was not feasible to apply the same

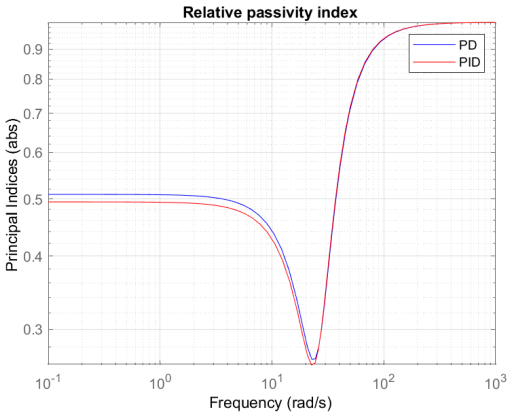

(a) DC motor

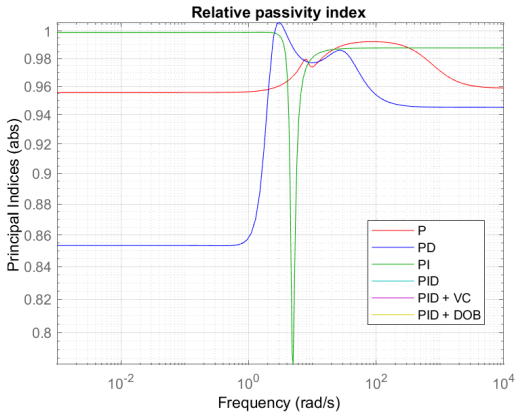

(b) Linear motor

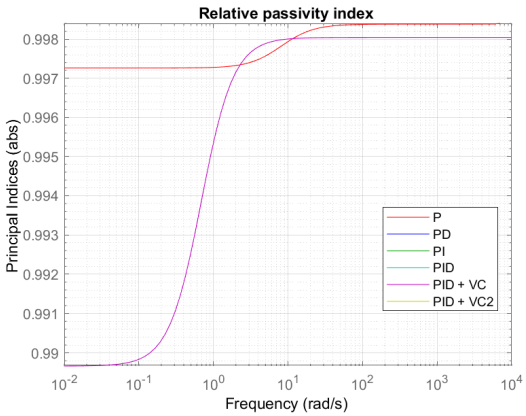

(c) Hydraulic cylinder

Figure 54 – Passivity Indices.

procedure for IC2D, it was determined that the identified functions would be used to analytically calculate the metrics.

Table 10 – Transparency and Backdrivability gain - DC motor

	PD	**PID**	**PD - exp**	**PID - exp**
F_t [N.m]	8.50	8.45	3.55	3.308
κ_{B_f}	1.51	1.52	1.10	1.17

Regarding ForceCAST, we have the option to compare the experimental results with the simulation results. It was observed that the transparency functions identified in both cases were very similar. Additionally, the transparency and backdrivability gain values were also quite close. The relationship between using a PID controller and achieving a subtle improvement compared to using a PD controller was maintained. Although the specific values themselves were not very close, the overall relationship between the two control strategies was partially maintained. The same input was applied in both the experimental and simulation setups, which involved a position sweep ranging from 0 to 8 Hz with an amplitude of 0.3 rad.

Table 11 – Transparency and Backdrivability gain - LinMot

	P	**PD**	**PI**	**PID**	**PID+VC**	**PID+DOB**
F_t $[N]$	10.30	11.80	10.99	14.09	11.55	13.72
κ_{B_f}	1.68	1.47	1.58	1.23	1.50	1.26

The LinMot and hydraulic actuator were subjected to a sinusoidal input with a velocity amplitude of 0.2 m/s at a frequency of 2 Hz. A comparison between the two reveals that the residual force in the hydraulic actuator is ten times higher than in the electric actuator. This observation aligns with reality as the presence of friction in the cylinder is much more pronounced in the hydraulic actuator compared to the LinMot. The hydraulic actuation system is significantly less backdrivable since even with controllers that have ample room for improvement, there are substantial gains in backdrivability, particularly for controllers equipped with velocity compensation.

Table 12 – Transparency and Backdrivability gain - Hydraulic cylinder

	P	**PD**	**PI**	**PID**	**PID+VC1**	**PID+VC2**
F_t $[N]$	142.45	131.99	138.50	134.77	138.50	68.58
κ_{B_f}	2.10	2.27	2.16	2.22	2.16	4.36

In Table 12, it can be observed that the transparency of the actuator was negatively affected by the derivative gain, while the load velocity compensation played a more significant role. In Table 11, the VC and DOB controllers showed a slight improvement compared to the PID controller, although it was not the best compared to the P, PD and PI controllers.

7 CONCLUSION

This Master's main objective is a systematic comparison of stability and performance of force controllers applied to electric and hydraulic actuators. However, since there is no consolidated benchmarking methodology and metrics for this purpose, the first step was to develop a methodology and a set of metrics to classify the performance of force controller systems. The developed method is a novel approach mainly due to a modeling framework that separates the coupled system dynamics into two intuitive parts: one that depends only on the blocked actuator; and another one that brings all the influence of the load into the system response. It was possible because the method was model-based, which keeps it general, that is, independent of the actuator, and avoids testing the force-controlled system interacting with several environments.

To implement the methodology, it was necessary to design, manufacture, assemble and validate the experimental bench with the actuators to be evaluated. The project involved many iterative steps, reworks and various challenges. Therefore, in parallel, the methodology was being developed through simulations, and it was applied at IC2D only at the end of 2023. During the BEPE internship, it was then possible to start applying the methodology on an experimental platform. Many challenges were faced again, such as friction on the bench, configuration limitations in ForceCAST, and data acquisition in general. The project as a whole had the contribution of several members of the research group, in the experimental part in particular the master's students Cícero and Lucca and the doctoral student Leonardo. For the methodology, it was worked on together with the doctoral student Victor.

In general, the identifications fit as expected, the validations, considering that system identification even more so by inserting many external variables such as friction on the bench, which resulted in an unknown environment, the difficulty of carrying out the SISO tests for the DC motor and the hydraulic actuator. From the identification of the transfer functions T_t and T_i, the metrics are easily calculated. Furthermore, the method can capture the most relevant information on force control. Regarding the benchmarking of the controllers proposed in the case study, it became evident that as a derivative gain can negatively impact the performance of an actuator, it showed that velocity compensation, especially in the hydraulic actuator, improves the speed and bandwidth of the controller. The hydraulic actuators had slower responses compared to electric actuators. However, the presence of non-linearities in the actuation system model negatively impacts the performance of linear controllers like PID. When comparing different benches, the DC motor of the electric actuators exhibited a better overall performance. Nonetheless, when taking into account the design of the actuation systems, it becomes feasible to attain

quicker responses using hydraulic actuators. In other words, these comparisons among actuators depend on the controllers, thereby rendering the methodology a valuable tool that enables an iterative approach to finding a suitable controller-actuator combination for a specific application.

To conclude, it is evident that the utilization of system identification in methodologies has both pros and cons. On the positive side, it enables the inclusion of comprehensive metrics that evaluate system stability, thereby indicating whether the system is at risk of instability. In contrast, without system identification, one can only make inferences about system stability in a given configuration. Furthermore, the methodology facilitates quicker computation of metrics overall due to its analytical nature.

In future research, there is potential for further development of metrics and identification methods. For instance, additional closed-loop linearity metrics could be incorporated into the benchmarking process. Another possibility is the development of load dependent metrics. To enhance the performance of force controllers for hydraulic systems, it is crucial to test non-linear controls, whether they are model based or not. One example of a non-linear control strategy that could be explored is feedback linearization. However, it is important to note that the effectiveness of such a controller relies on the quality of the model. This is highlighted in Appendix A, where it is mentioned that characteristics such as valve leakage and pressure sensitivity can contribute to improving the overall model. To identify the necessary parameters, tests need to be conducted using pressure and flow sensors. Fortunately, both sensors have already been acquired, and these tests will be carried out sequentially. The results of these tests will enable the creation of a more accurate model that better represents the bench. Consequently, it is expected that the performance of all model based controllers will also improve. Validation of the linear actuator model will also be carried out with a view to improving the performance of force actuators on the bench, as impedance controllers will be implemented in the next stages, so the internal force loop must have the best possible performance. The bench construction can also be enhanced in order to minimize friction, however, it will prove highly valuable for the research team as it enables the examination of controllers in a controlled setting and at the joint level.

REFERENCES

ALLEYNE, Andrew; LIU, Rui. On the Limitations of Force Tracking Control for Hydraulic Servosystems. **Journal of Dynamic Systems, Measurement, and Control**, v. 121, n. 2, p. 184–190, June 1999. ISSN 0022-0434. DOI: 10.1115/1.2802453. eprint: https://asmedigitalcollection.asme.org/dynamicsystems/article-pdf/121/2/184/5516008/184_1.pdf. Available from: https://doi.org/10.1115/1.2802453.

ATKESON, C. G. et al. Using Humanoid Robots to Study Human Behaviour. **IEEE Intelligent Systems**, v. 15, p. 46–56, 2000.

BÄHLER, Jannis. Investigation of the Performance of Commercially Available Actuators. Bachelor Thesis, 2021.

BEHRENS, Rol et al. Performance Indicator for Benchmarking Force-Controlled Robots. In: 2018 IEEE International Conference on Robotics and Automation (ICRA). 2018. P. 1653–1660. DOI: 10.1109/ICRA.2018.8460858.

BOAVENTURA, Thiago. **Hydraulic Compliance Control of the Quadruped Robot HyQ**. 2013. PhD thesis – Istituto Italiano di Tecnologia and University of Genoa. Ph.D. thesis.

_____._____. 2013. PhD thesis – University of Genoa.

BOAVENTURA, Thiago; BUCHLI, Jonas, et al. Model-based hydraulic impedance control for dynamic robots. **IEEE Transactions on Robotics**, IEEE, v. 31, n. 6, p. 1324–1336, 2015.

BOAVENTURA, Thiago; FOCCHI, Michele, et al. On the role of load motion compensation in high-performance force control. In: IEEE. 2012 IEEE/RSJ International Conference on Intelligent Robots and Systems. 2012. P. 4066–4071.

BOAVENTURA, Thiago; SEMINI, Claudio. Hydraulic Actuation. In: ENCYCLOPEDIA of Robotics. Berlin, Heidelberg: Springer Berlin Heidelberg, 2020. P. 1–10. ISBN 978-3-642-41610-1. DOI: 10.1007/978-3-642-41610-1_116-1. Available from: https://doi.org/10.1007/978-3-642-41610-1_116-1.

BRUHM, Hartmut; CZINKI, Alexander; LOTZ, Markus. High performance force control - A new approach and suggested benchmark tests. **IFAC-PapersOnLine**, v. 48, n. 10, p. 165–170, 2015. 2nd IFAC Conference on Embedded Systems, Computer Intelligence and Telematics CESCIT 2015. ISSN 2405-8963. DOI: https://doi.org/10.1016/j.ifacol.2015.08.126. Available from: https://www.sciencedirect.com/science/article/pii/S2405896315009933.

CALANCA, Andrea; MURADORE, Riccardo; FIORINI, Paolo. A Review of Algorithms for Compliant Control of Stiff and Fixed-Compliance Robots. **IEEE/ASME Transactions on Mechatronics**, v. 21, p. 1–1, Jan. 2015. DOI: 10.1109/TMECH.2015.2465849.

_____. Impedance control of series elastic actuators: Passivity and acceleration-based control. **Mechatronics**, v. 47, p. 37–48, Nov. 2017. DOI: 10.1016/j.mechatronics.2017.08.010.

CALLISTER, William D; RETHWISCH, David G. **Fundamentals of materials science and engineering**. Wiley London, 2007. v. 4.

CAO, Wenping et al. Overview of electric motor technologies used for more electric aircraft (MEA). **IEEE transactions on industrial electronics**, IEEE, v. 59, n. 9, p. 3523–3531, 2011.

CHEN, Shan; CHEN, Zheng, et al. Adaptive robust cascade force control of 1-DOF hydraulic exoskeleton for human performance augmentation. **IEEE/ASME Transactions on Mechatronics**, IEEE, v. 22, n. 2, p. 589–600, 2016.

CHEN, Shan; ZHANG, Heng, et al. Adaptive robust force control of an underactuated walking lower limb hydraulic exoskeleton. **Transactions of the Institute of Measurement and Control**, SAGE Publications Sage UK: London, England, p. 01423312221125971, 2022.

CHO, Buyoun et al. Design of a compact embedded hydraulic power unit for bipedal robots. **IEEE Robotics and Automation Letters**, IEEE, v. 6, n. 2, p. 3631–3638, 2021.

CHOI, Youngjin et al. On the robustness and performance of disturbance observers for second-order systems. **IEEE Transactions on Automatic Control**, IEEE, v. 48, n. 2, p. 315–320, 2003.

CLARK, Daniel C. Selection and performance criteria for electrohydraulic servodrives. In: PROCEEDINGS of the 25th annual meeting of the national Conference on Fluid Power. 1969.

COLGATE, Ed; HOGAN, Neville. The Interaction of Robots with Passive Environments: Application to Force Feedback Control. In_____. **Advanced Robotics: 1989**. Berlin, Heidelberg: Springer Berlin Heidelberg, 1989. P. 465–474. ISBN 978-3-642-83957-3.

DUFFY, Joseph. 'The fallacy of modern hybrid control theory that is based on "orthogonal complements. **of twist and wrench spaces,"J. Robot. Syst**, v. 7, n. 2, p. 139–144, 1990.

DYKE, SJ et al. Role of control-structure interaction in protective system design. **Journal of engineering mechanics**, American Society of Civil Engineers, v. 121, n. 2, p. 322–338, 1995.

EPPINGER, S.; SEERING, W. Understanding bandwidth limitations in robot force control. In: PROCEEDINGS. 1987 IEEE International Conference on Robotics and Automation. 1987. v. 4, p. 904–909. DOI: 10.1109/ROBOT.1987.1087932.

FAHMI, Shamel et al. Stance: Locomotion adaptation over soft terrain. **IEEE Transactions on Robotics**, IEEE, v. 36, n. 2, p. 443–457, 2020.

FALCO, Joseph et al. **Benchmarking Robot Force Control Capabilities: Experimental Results**. en. NIST Interagency/Internal Report (NISTIR), National Institute of Standards and Technology, Gaithersburg, MD, 2016. DOI: https://doi.org/10.6028/NIST.IR.8097.

GARY, WK; PATRICK, SKC. Water hydraulics-theory and applications. In: WORKSHOP on Water Hydraulics, Agricultural Equipment Technology Conference (AETC∼04), Louisville. 2004. P. 1–33.

GEORGIOU, Tryphon T. On the computation of the gap metric. **Systems & Control Letters**, v. 11, n. 4, p. 253–257, 1988. ISSN 0167-6911. DOI: https://doi.org/10.1016/0167-6911(88)90067-9. Available from: https://www.sciencedirect.com/science/article/pii/0167691188900679.

GRIMMINGER, F. et al. An Open Torque-Controlled Modular Robot Architecture for Legged Locomotion Research. **IEEE Robotics and Automation Letters**, v. 5, n. 2, p. 3650–3657, 2020. DOI: 10.1109/LRA.2020.2976639.

HAMMER, Lisa. Human-Robot Interaction Force Estimation for Transparency Control on WearableRobots. Master Thesis, 2016.

HIGA, Felipe Y. G. et al. Joint kinematic configuration influence on the passivity of an impedance-controlled robotic leg. In: 2019 International Conference on Robotics and Automation (ICRA). 2019. P. 9516–9522. DOI: 10.1109/ICRA.2019.8794094.

HODGES, Peter. **Hydraulic fluids**. Butterworth-Heinemann, 1996.

HODOSHIMA, R. et al. Development of Quadruped Walking Robot TITAN XI for Steep Slopes - Slope Map Generation and Map Information Application. **Journal of Robotics and Mechatronics**, v. 19, p. 13–26, 2007.

HOGAN, Neville. Impedance Control: An Approach to Manipulation. In: 1984 American Control Conference. 1984. P. 304–313. DOI: 10.23919/ACC.1984.4788393.

HOGAN, Neville; BUERGER, Stephen P. Impedance and interaction control. In: ROBOTICS and automation handbook. CRC press, 2018. P. 375–398.

HUANG, Yuancan; HUANG, Qiang. Interaction Stability Analysis from the Input-Output Viewpoints. In: 2020 IEEE International Conference on Robotics and Automation (ICRA). 2020. P. 7878–7884. DOI: 10.1109/ICRA40945.2020.9196643.

HUTTER, Marco et al. Anymal-a highly mobile and dynamic quadrupedal robot. In: IEEE. 2016 IEEE/RSJ international conference on intelligent robots and systems (IROS). 2016. P. 38–44.

HYON, S. H.; EMURA, T.; MITA, T. Dynamics-based control of a one-legged hopping robot. **J. Syst. Control Eng.**, 217 (2), p. 83–89, 2003.

JIN, Jianxun et al. Simulation and analysis of a PMLSM control system based on SVPWM. In: IEEE. PROCEEDINGS of the 29th Chinese Control Conference. 2010. P. 3316–3320.

JO, Nam Hoon; SHIM, Hyungbo; SON, Young Ik. Disturbance observer for non-minimum phase linear systems. **International Journal of Control, Automation and Systems**, Springer, v. 8, p. 994–1002, 2010.

KATSURA, Seiichiro; IRIE, Kouhei; OHISHI, Kiyoshi. Wideband force control by position-acceleration integrated disturbance observer. **IEEE Transactions on Industrial Electronics**, IEEE, v. 55, n. 4, p. 1699–1706, 2008.

KIM, Hyomin; KWON, Jaesung, et al. Weighted Hybrid Admittance-Impedance Control with Human Intention Based Stiffness Estimation for Human-Robot Interaction. In: 2018 IEEE/RSJ International Conference on Intelligent Robots and Systems (IROS). 2018. P. 1–6. DOI: 10.1109/IROS.2018.8594435.

KIM, Jin Tak; CHO, Jung San; PARK, Byung-Yun, et al. Experimental investigation on the design of leg for a hydraulic actuated quadruped robot. In: 44TH International Symposium on Robotics (ISR). 2013.

KIM, Sung-Woo; CHO, Buyoun; SHIN, Seunghoon, et al. Force control of a hydraulic actuator with a neural network inverse model. **IEEE Robotics and Automation Letters**, IEEE, v. 6, n. 2, p. 2814–2821, 2021.

KONAMI, S.; NISHIUMI, T. **Hydraulic Control Systems: Theory And Practice**. World Scientific Publishing Company, 2016. ISBN 9789814759663. Available from: https://books.google.com.br/books?id=UWVIDQAAQBAJ.

KURFESS, Thomas R. Robotics and automation handbook. In: CRC press, 2018. Impedance and Interaction Control.

LEVINE, William S. **The Control Handbook (three volume set)**. CRC press, 2018.

MERRITT, H E. **Hydraulic Control Systems**. Cincinnati, Ohio: John Wileys and Sons, 1967. ISBN 0-471-59617-5.

_____._____. Wiley, 1991. ISBN 9780471596172. Available from: https://books.google.com.br/books?id=Imu-v-6lzwYC.

NIKIFORUK, PN; UKRAINETZ, PR; TSAI, SC. Detailed analysis of a two-stage four-way electrohydraulic flow-control valve. **Journal of Mechanical engineering science**, SAGE Publications Sage UK: London, England, v. 11, n. 2, p. 168–174, 1969.

NIKSEFAT, N.; SEPEHRI, N. Designing robust force control of hydraulic actuators despite system and environmental uncertainties. **IEEE Control Systems Magazine**, v. 21, n. 2, p. 66–77, 2001. DOI: 10.1109/37.918266.

OHISHI, Kiyoshi; MIYAZAKI, Toshimasa; NAKAMURA, Yoshihiro. Two-degrees-of-freedom speed controller based on doubly coprime factorization and speed observer. In: IEEE. PROCEEDINGS of IECON'95-21st Annual Conference on IEEE Industrial Electronics. 1995. v. 1, p. 602–608.

OHNISHI, Kouhei; SHIBATA, Masaaki; MURAKAMI, Toshiyuki. Motion control for advanced mechatronics. **IEEE/ASME transactions on mechatronics**, IEEE, v. 1, n. 1, p. 56–67, 1996.

OTT, Christian; MUKHERJEE, Ranjan; NAKAMURA, Yoshihiko. A Hybrid System Framework for Unified Impedance and Admittance Control. **Journal of Intelligent & Robotic Systems**, v. 78, p. 359–375, June 2015. DOI: 10.1007/s10846-014-0082-1.

PARK, RW. Contamination control–a hydraulic OEM perspective. In: WORKSHOP on Total Contamination Control. 1997.

PASOLLI, Philipp; RUDERMAN, Michael. Hybrid state feedback position-force control of hydraulic cylinder. In: IEEE. 2019 IEEE International Conference on Mechatronics (ICM). 2019. v. 1, p. 54–59.

PINTELON, Rik; SCHOUKENS, Johan. FRF Measurement of Nonlinear Systems Operating in Closed Loop. **IEEE Transactions on Instrumentation and Measurement**, v. 62, n. 5, p. 1334–1345, 2013. DOI: 10.1109/TIM.2012.2220033.

PRATT, G.A.; WILLIAMSON, M.M. Series elastic actuators. In: PROCEEDINGS 1995 IEEE/RSJ International Conference on Intelligent Robots and Systems. Human Robot Interaction and Cooperative Robots. 1995. v. 1, 399–406 vol.1. DOI: 10.1109/IROS.1995.525827.

RAIBERT, Marc H; CRAIG, John J. Hybrid position/force control of manipulators, 1981.

RAMPELTSHAMMER, Wolfgang F. et al. Evaluation and comparison of SEA torque controllers in a unified framework. **ArXiv**, abs/2201.00583, 2022.

RHEE, Issac et al. Hybrid impedance and admittance control of robot manipulator with unknown environment. **Intelligent Service Robotics**, v. 16, n. 1, p. 49–60, 2023. DOI: 10.1007/s11370-022-00451-5.

ROBINSON, D.W. et al. Series elastic actuator development for a biomimetic walking robot. In: 1999 IEEE/ASME International Conference on Advanced Intelligent Mechatronics (Cat. No.99TH8399). 1999. P. 561–568. DOI: 10.1109/AIM.1999.803231.

RONG, Xuewen et al. Design and simulation for a hydraulic actuated quadruped robot. **Journal of Mechanical Science and Technology**, Springer Science + Business Media, v. 26, n. 4, p. 1171–1177, 2012. ISSN 1976-3824.

ROOZING, Wesley et al. On the Stiffness Selection for Torque-Controlled Series-Elastic Actuators. **IEEE Robotics and Automation Letters**, v. 2, n. 4, p. 2255–2262, 2017. DOI: 10.1109/LRA.2017.2726141.

ROZALI, S Md et al. PID controller design for an industrial hydraulic actuator with servo system. In: IEEE. 2010 IEEE Student Conference on Research and Development (SCOReD). 2010. P. 218–223.

SAFONOV, Michael George. **Stability and Robustness of Multivariable Feedback Systems**. Cambridge, MA, USA: MIT Press, 1980. ISBN 0262191806.

SARIYILDIZ, Emre; OHNISHI, Kouhei. A guide to design disturbance observer. **Journal of Dynamic Systems, Measurement, and Control**, American Society of Mechanical Engineers, v. 136, n. 2, p. 021011, 2014.

_____. Analysis the robustness of control systems based on disturbance observer. **International Journal of Control**, Taylor & Francis, v. 86, n. 10, p. 1733–1743, 2013.

SCHAFT, A. van der. **L2-Gain and Passivity Techniques in Nonlinear Control**. Springer International Publishing, 2016. (Communications and Control Engineering). ISBN 9783319499925. Available from: https://books.google.com.br/books?id=jvmoDQAAQBAJ.

SEMINI, Claudio; BARASUOL, Victor, et al. Brief introduction to the quadruped robot HyQReal. In: ITALIAN Conference on Robotics and Intelligent Machines (I-RIM). 2019.

SEMINI, Claudio; TSAGARAKIS, Nikos G; GUGLIELMINO, Emanuele, et al. Design of HyQ–a hydraulically and electrically actuated quadruped robot. **Proceedings of the Institution of Mechanical Engineers, Part I: Journal of Systems and Control Engineering**, SAGE Publications Sage UK: London, England, v. 225, n. 6, p. 831–849, 2011.

SEMINI, Claudio; TSAGARAKIS, Nikos G; VANDERBORGHT, Bram, et al. HyQ-Hydraulically actuated quadruped robot: Hopping leg prototype. In: IEEE. 2008 2nd IEEE RAS & EMBS International Conference on Biomedical Robotics and Biomechatronics. 2008. P. 593–599.

SEMINI, Claudio; TSAGARAKIS, Nikos G.; GUGLIELMINO, Emanuele, et al. Design of HyQ - a Hydraulically and Electrically Actuated Quadruped Robot. **IMechE Part I: Journal of Systems and Control Engineering**, v. 225, n. 6, p. 831–849, 2011.

SEOK, Sangok et al. Actuator design for high force proprioceptive control in fast legged locomotion. In: IEEE. 2012 IEEE/RSJ International Conference on Intelligent Robots and Systems. 2012. P. 1970–1975.

SHIME, Victor; NETO, José L Montandon; BOAVENTURA, Thiago. Force Control Benchmarking in the Gap Metric. In: IEEE. 2023 Latin American Robotics Symposium (LARS), 2023 Brazilian Symposium on Robotics (SBR), and 2023 Workshop on Robotics in Education (WRE). 2023. P. 373–378.

SOMASHEKHAR, SH; SINGAPERUMAL, M; KUMAR, R Krishna. Mathematical modelling and simulation of a jet pipe electrohydraulic flow control servo valve. **Proceedings of the Institution of Mechanical Engineers, Part I: Journal of Systems and Control Engineering**, SAGE Publications Sage UK: London, England, v. 221, n. 3, p. 365–382, 2007.

TALIB, Mat Hussin Ab; DARNS, Intan Z Mat. Self-tuning PID controller for active suspension system with hydraulic actuator. In: IEEE. 2013 IEEE Symposium on Computers & Informatics (ISCI). 2013. P. 86–91.

UGURLU, Barkan et al. Benchmarking Torque Control Strategies for a Torsion-Based Series Elastic Actuator. **IEEE Robotics I& Automation Magazine**, v. 29, n. 2, p. 85–96, 2022. DOI: 10.1109/MRA.2021.3124154.

UMENO, Takaji; HORI, Yoichi. Robust speed control of DC servomotors using modern two degrees-of-freedom controller design. **IEEE Transactions on industrial electronics**, IEEE, v. 38, n. 5, p. 363–368, 1991.

UR REHMAN, Bilal et al. Design of a hydraulically actuated arm for a quadruped robot. In: WORLD SCIENTIFIC. ASSISTIVE ROBOTICS: Proceedings of the 18th International Conference on CLAWAR 2015. 2016. P. 283–290.

VERGAMINI, Elisa; SANTOS, Leonardo Felipe; ZANETTE, Cícero. **IC2D Project**. GitHub, 2023. https://github.com/leggedrobotics-usp/ic2d.

VICARIO, Rudy et al. Benchmarking Force Control Algorithms. In: THE 14th PErvasive Technologies Related to Assistive Environments Conference. 2021. P. 359–364.

_____._____. In: THE 14th PErvasive Technologies Related to Assistive Environments Conference. Corfu, Greece: Association for Computing Machinery, 2021. (PETRA 2021), p. 359–364. ISBN 9781450387927. DOI: 10.1145/3453892.3461332. Available from: https://doi.org/10.1145/3453892.3461332.

VORNDAMME, Jonathan et al. Soft robotics for the hydraulic atlas arms: Joint impedance control with collision detection and disturbance compensation. In: IEEE. 2016 IEEE/RSJ International Conference on Intelligent Robots and Systems (IROS). 2016. P. 3360–3367.

WANG, Chun-Chih; TOMIZUKA, Masayoshi. Design of robustly stable disturbance observers based on closed loop consideration using H/sub/spl infin//optimization and its applications to motion control systems. In: IEEE. PROCEEDINGS of the 2004 American Control Conference. 2004. v. 4, p. 3764–3769.

WANG, Xu Dong; FENG, Hai Chao, et al. Modeling and Simulation of Direct Force Control for PMLSM. **Advanced Materials Research**, Trans Tech Publ, v. 216, p. 692–697, 2011.

WATTON, John. **Fundamentals of fluid power control**. Cambridge University Press, 2009. v. 10.

XIA, Meng et al. Sector bounds in stability analysis and control design. **International Journal of Robust and Nonlinear Control**, v. 30, n. 18, p. 7857–7882, 2020. DOI: https://doi.org/10.1002/rnc.5236. eprint: https://onlinelibrary.wiley.com/doi/pdf/10.1002/rnc.5236. Available from: https://onlinelibrary.wiley.com/doi/abs/10.1002/rnc.5236.

YANG, Yousheng et al. Water vs. oil hydraulic actuation for a robot leg. In: IEEE. 2009 International Conference on Mechatronics and Automation. 2009. P. 1940–1946.

YU, Lijuan et al. Sliding-Mode Control for PMLSM Position Control—A Review. In: MDPI, 1. ACTUATORS. 2023. v. 12, p. 31.

ZANETTE, Cícero et al. Análise de atrito de uma bancada experimental hidráulica. In: SIMPÓSIO do Programa de Pós-Graduação em Engenharia Mecânica da EESC-USP (SiPGEM/EESC-USP). 2023. Available from: http://soac.eesc.usp.br/index.php/SiPGEM/viisipgem/paper/view/3806/2658.

APPENDIX

APPENDIX A – HYDRAULIC ACTUATION SYSTEM MODEL

In this appendix, the entire modeling of the hydraulic actuation system is described in more detail, as well as the force controllers used on them, following the model developed in (BOAVENTURA, 2013b).

A.1 Equation index

$\beta \rightarrow$ Bulk Modulus

$\Delta x_v \rightarrow$ valve spool position in meters

$\Delta u_v \rightarrow$ valve spool position in Amperes

$a(u_v) \rightarrow$ valve orifice area

$q \rightarrow$ valve flow

$K_v \rightarrow$ valve constant

$A_p \rightarrow$ piston area

$\alpha \rightarrow$ ratio factor between piston areas

$q_a \rightarrow$ cylinder chamber a flow

$q_b \rightarrow$ cylinder chamber b flow

$v_a \rightarrow$ cylinder chamber a volume

$v_b \rightarrow$ cylinder chamber b volume

$p_l \rightarrow$ load pressure

$f_h \rightarrow$ hydraulic force

$\dot{f}_h \rightarrow$ hydraulic force dynamics

$f \rightarrow$ load force

$\dot{f} \rightarrow$ load force dynamics

A.2 Fluid

$$\beta = -v_o \left(\frac{\delta P}{\delta v} \right) \tag{A.1}$$

$\beta \rightarrow$ Bulk Modulus $[Pa]$;

$v_o \rightarrow$ initial volume of the confined fluid $[m^3]$;

$P \rightarrow$ pressure applied to the fluid $[Pa]$;

$v \rightarrow$ final volume of the pressurized fluid $[m^3]$.

A.3 Valve

$$\Delta x_v = \left(\frac{K_{spool}}{\frac{1}{\omega_v^2} s^2 + \frac{2D_v}{\omega_v} s + 1} \right) \Delta u \tag{A.2}$$

$\Delta x_v \rightarrow$ valve spool position $[m]$, difficult to measure, so it is used Δu_v $[A]$ to indicate the spool position;

$K_{spool} \rightarrow$ steady-state valve input-to-spool-position gain $[m/A]$

$\omega_v \rightarrow F_v = \frac{\omega_v}{2\pi}$: valve spool frequency $[Hz]$;

$D_v \rightarrow$ valve spool damping

$\Delta u \rightarrow$ valve control signal $[A]$;

$$\Delta u_v = \left(\frac{1}{\frac{1}{\omega_v^2} s^2 + \frac{2D_v}{\omega_v} s + 1} \right) \Delta u \tag{A.3}$$

$\Delta u_v \rightarrow$ valve spool position $[A]$;

$\omega_v \rightarrow F_v = \frac{\omega_v}{2\pi}$: valve spool frequency $[Hz]$;

$D_v \rightarrow$ valve spool damping

$\Delta u \rightarrow$ valve control signal $[A]$;

$$\Delta u_v = \frac{1}{K_{spool}} \Delta x_v \tag{A.4}$$

$\Delta u_v \rightarrow$ valve spool position $[A]$;

$K_{spool} \rightarrow$ spool gain $[m/A]$;

$\Delta x_v \rightarrow$ valve spool position $[m]$.

The valve flow control is done by opening the orifice through which the oil passes, which is given by the equation:

$$a(u_v) = W u_v \tag{A.5}$$

$a \rightarrow$ adjustable area $[m^2]$;

$W \rightarrow$ area gradient $[m^2/A]$, hard to find based on datasheets;

$u_v \rightarrow$ valve spool position [A].

$$q = K_v u_v \sqrt{\Delta p} \tag{A.6}$$

$q \rightarrow$ flow $[m^3/s]$;

$K_v \rightarrow$ valve gain;

$u_v \rightarrow$ valve spool position [A];

$\Delta p \rightarrow$ pressure drop across a valve control port;

$$K_v = \frac{C_d W \sqrt{2}}{\sqrt{\rho}} = \frac{q_n}{u_{v_n}\sqrt{\Delta p_{n_1}}} = \frac{q_n}{u_{v_n}\sqrt{\frac{\Delta p_{n_2}}{2}}} \tag{A.7}$$

The data for q_n, u_{v_n}, Δp_{n_1} and Δp_{n_2} can usually be found in the valves' datasheets. If they are not found, it is possible to obtain them by following the procedure described on A.8.1.

$C_d \rightarrow$ discharge coefficient, worth approximately 0.6 (MERRITT, 1967);

$W \rightarrow$ area gradient $[m^2/A]$, hard to find based on datasheets;

$\rho \rightarrow$ oil density $[kg/m^3]$;

$q_n \rightarrow$ nominal flow $[m^3/s]$;

$u_{v_n} \rightarrow$ valve nominal input $[A]$;

$\Delta p_{n_1} \rightarrow$ nominal pressure drop across a valve control port $[Pa]$;

$\Delta p_{n_2} \rightarrow$ nominal pressure drop across two valve control ports $[Pa]$;

A.4 Cylinder

$$A_p = A_a = \frac{\pi {D_p}^2}{4} \tag{A.8}$$

$$A_b = \frac{\pi \left(D_p^2 - D_r^2\right)}{4} = \alpha A_p \tag{A.9}$$

$$\alpha = \frac{A_b}{A_a} = \frac{D_p^2 - D_r^2}{D_p^2} \tag{A.10}$$

$A_p \rightarrow$ piston area $[m^2]$;

$A_a \rightarrow$ chamber a piston area $[m^2]$;

$A_b \rightarrow$ chamber b piston area $[m^2]$;

$D_p \rightarrow$ piston diameter $[m^2]$;

$D_r \rightarrow$ cylinder axis diameter $[m^2]$;

$\alpha \rightarrow$ ratio factor between piston areas.

Taking Equation A.6 as a basis, it is possible to write these flow equations for each chamber of the cylinder.

$$q_a = \begin{cases} K_v u_v \sqrt{p_s - p_a}, & u_v > 0 \\ K_v u_v \sqrt{p_a - p_t}, & u_v < 0 \end{cases} \tag{A.11}$$

$$q_b = \begin{cases} K_v u_v \sqrt{p_b - p_t}, & u_v > 0 \\ K_v u_v \sqrt{p_s - p_b}, & u_v < 0 \end{cases} \tag{A.12}$$

$q_a \rightarrow$ cylinder chamber a flow $[m^3/s]$;

$q_b \rightarrow$ cylinder chamber b flow $[m^3/s]$;

$K_v \rightarrow$ valve gain;

$u_v \rightarrow$ valve spool position $[A]$;

$p_a \rightarrow$ cylinder chamber a pressure $[Pa]$;

$p_b \rightarrow$ cylinder chamber b pressure $[Pa]$;

$p_s \rightarrow$ pump pressure $[Pa]$;

$p_t \rightarrow$ tank pressure $[Pa]$;

A.4.1 Dynamic pressure equations

Consider the masses of fluid in chambers a and b:

$$m_a = v_a \rho(p_a) \tag{A.13}$$

$$m_b = v_b \rho(p_b) \tag{A.14}$$

Differentiating in time:

$$\dot{m}_a = \dot{v}_a \rho(p_a) + v_a \dot{\rho}(p_a) \tag{A.15}$$

$$\dot{m}_b = \dot{v}_b \rho(p_b) + v_b \dot{\rho}(p_b) \tag{A.16}$$

See that, by the chain rule:

$$\dot{\rho}(p) = \frac{d\rho}{dp}\dot{p}$$

Furthermore, the variation in density with pressure can be expressed by (MERRITT, 1967):

$$\frac{d\rho}{dp} = \frac{\rho}{\beta(p)} \tag{A.17}$$

Remembering that mass flows and volumetric flows are related by

$$\dot{m} = \rho q \tag{A.18}$$

We then have:

$$\rho(p_a)q_a = \dot{v}_a\rho(p_a) + v_a\frac{\rho(p_a)}{\beta(p_a)}\dot{p}_a \tag{A.19}$$

$$\rho(p_b)q_b = \dot{v}_b\rho(p_b) + v_b\frac{\rho(p_b)}{\beta(p_b)}\dot{p}_b \tag{A.20}$$

Simplifying $\rho(p)$, we see that for both chambers we have:

$$\dot{p} = \frac{\beta(p)}{v}(q - \dot{v}) \tag{A.21}$$

Adopting the simplification $\beta(p_a) = \beta(p_b) = \beta_e$, and using the following volume derivatives:

$$\frac{dv_a}{dt} = \frac{d}{dt}(v_{pl} + A_p x_p) = A_p\dot{x}_p \tag{A.22}$$

$$\frac{dv_b}{dt} = \frac{d}{dt}\left(v_{pl} + (l_{cyl} - x_p)\alpha A_p\right) = -\alpha A_p\dot{x}_p \tag{A.23}$$

We then have:

$$\dot{p}_a = \frac{\beta_e}{v_a}\left(q_a - A_p\dot{x}_p\right) \tag{A.24}$$

$$\dot{p}_b = \frac{\beta_e}{v_b}\left(-q_b + \alpha A_p\dot{x}_p\right) \tag{A.25}$$

Where:

$$v_a = v_{pl} + A_p x_p \tag{A.26}$$

$$v_b = v_{pl} + \left(l_{cyl} - x_p\right)\alpha A_p \tag{A.27}$$

It is worth mentioning that the negative sign in the flow rate q_b in (A.25) is due to the fact that we adopt here q_b leaving the control volume that represents the cylinder.

$p_a \rightarrow$ cylinder chamber a pressure $[Pa]$;

$p_b \rightarrow$ cylinder chamber b pressure $[Pa]$;

$\beta_e \rightarrow$ oil Bulk Modulus $[Pa]$;

$v_a \rightarrow$ cylinder chamber a volume $[m^3]$;

$v_b \rightarrow$ cylinder chamber b volume $[m^3]$; pipe line volumevolume of *pipe line* $[m^3]$;

$q_a \rightarrow$ cylinder chamber a flow $[m^3/s]$;

$q_b \rightarrow$ cylinder chamber b flow $[m^3/s]$;

$x_p \rightarrow$ piston position $[m]$

$A_p \rightarrow$ piston area $[m^2]$;

$\alpha \rightarrow$ ratio factor between piston areas;

$l_{cyl} \rightarrow$ cylinder stroke.

The difference in forces generated between the chambers a and b is called *hydraulic force* and can be written as a function of the pressures in each chamber and the contact area on each side of the piston.

$$f_h = A_p p_a - \alpha A_p p_b = A_p \left(p_a - \alpha p_b\right) \tag{A.28}$$

$$p_l = \left(p_a - \alpha p_b\right) \tag{A.29}$$

$$f_h = A_p p_l \tag{A.30}$$

$f_h \rightarrow$ hydraulic force $[N]$;

$A_p \rightarrow$ piston area $[m^2]$;

$p_a \rightarrow$ cylinder chamber a pressure $[Pa]$;

$p_b \rightarrow$ cylinder chamber b pressure $[Pa]$;

$\alpha \rightarrow$ ratio factor between piston areas;

$p_l \rightarrow$ load pressure $[Pa]$.

By differentiating Equation A.28 and substituting Equations A.24 and A.25 it is possible to write the dynamics of the hydraulic force:

$$\dot{f_h} = \frac{A_p \beta_e}{v_a} \left(q_a - A_p \dot{x_p}\right) - \alpha \frac{A_p \beta_e}{v_b} \left(-q_b + \alpha A_p \dot{x_p}\right) \tag{A.31}$$

$f_h \rightarrow$ hydraulic force $[Pa]$;

$A_p \rightarrow$ piston area $[m^2]$;

$\beta_e \rightarrow$ oil Bulk Modulus $[Pa]$;

$v_a \rightarrow$ cylinder chamber a volume $[m^3]$;

$v_b \rightarrow$ cylinder chamber b volume $[m^3]$;

$q_a \rightarrow$ cylinder chamber a flow $[m^3/s]$;

$q_b \rightarrow$ cylinder chamber b flow $[m^3/s]$;

$x_p \rightarrow$ piston position $[m]$;

$\alpha \rightarrow$ ratio factor between piston areas.

The force that is actually applied to the load is equivalent to the hydraulic force (f_h) minus the friction force (f_f), this force is called *load force*. The friction force will be modeled as viscous friction only, but there are other types of friction that will be neglected.

$$f = f_h - f_f = f_h - B\dot{x}_p \tag{A.32}$$

$f \rightarrow$ load force $[N]$;

$f_h \rightarrow$ hydraulic force $[N]$;

$f_f \rightarrow$ friction force $[N]$;

$B \rightarrow$ viscous friction coefficient $[Ns/m]$;

$x_p \rightarrow$ piston position $[m]$.

Differentiating the Equation A.32 to obtain the load force dynamics:

$$\dot{f} = \dot{f_h} - B\ddot{x}_p \tag{A.33}$$

Replacing Equations A.11 and A.12 in A.31:

$$\dot{f} = \begin{cases} -\beta_e {A_p}^2 \left(\frac{1}{v_a} + \frac{\alpha^2}{v_b}\right) \dot{x}_p - B\ddot{x}_p + \beta_e A_p K_v \left(\frac{\sqrt{p_s - p_a}}{v_a} + \frac{\alpha\sqrt{p_b - p_t}}{v_b}\right) u_v, & u_v > 0 \\ -\beta_e {A_p}^2 \left(\frac{1}{v_a} + \frac{\alpha^2}{v_b}\right) \dot{x}_p - B\ddot{x}_p + \beta_e A_p K_v \left(\frac{\sqrt{p_a - p_t}}{v_a} + \frac{\alpha\sqrt{p_s - p_b}}{v_b}\right) u_v, & u_v < 0 \end{cases} \tag{A.34}$$

$f \rightarrow$ load force (*load force*) $[N]$;

$\beta \rightarrow$ oil Bulk Modulus$[Pa]$;

$A_p \rightarrow$ piston area $[m^2]$;

$v_a \rightarrow$ cylinder chamber a volume $[m^3]$;

$v_b \rightarrow$ cylinder chamber b volume $[m^3]$;

$x_p \rightarrow$ piston position $[m]$;

$B \rightarrow$ viscous friction coefficient $[Ns/m]$;

$K_v \rightarrow$ valve gain;

$p_a \rightarrow$ cylinder chamber a pressure $[Pa]$;

$p_b \rightarrow$ cylinder chamber b pressure $[Pa]$;

$p_s \rightarrow$ pump pressure $[Pa]$;

$p_t \rightarrow$ tank pressure $[Pa]$;

$\alpha \rightarrow$ ratio factor between piston areas;

$u_v \rightarrow$ valve spool position [A] .

A.5 System linearization

The linearization of a system is done around an operating point, a common point to be used for linearization of nonlinear hydraulic dynamics is:

$$P_{\oslash} = (p_{a\oslash}, p_{b\oslash}, u_{v\oslash}) = \left(\frac{\alpha p_s}{1+\alpha}, \frac{p_s}{1+\alpha}, 0\right) \tag{A.35}$$

$p_a \rightarrow$ cylinder chamber a pressure $[Pa]$;

$p_b \rightarrow$ cylinder chamber b pressure $[Pa]$;

$p_s \rightarrow$ pump pressure $[Pa]$;

$\alpha \rightarrow$ ratio factor between piston areas;

$u_v \rightarrow$ valve spool position [A] .

From this point on, all variables that have a Δ preceding them will be linearized variables (e.g.: q_a is a non-linear variable, Δq_a is the same linearized variable).

The q_a and q_b equations are non-linear, to linearize them you can perform a Taylor expansion and truncate it after the first differential term. Equation A.36 shows the first order Taylor polynomial.

$$P_1(x,y) = f(P_{\oslash}) + \frac{\partial f}{\partial x}\Big|_{P_{\oslash}}(x - x_{\oslash}) + \frac{\partial f}{\partial y}\Big|_{P_{\oslash}}(y - y_{\oslash}) \tag{A.36}$$

Letting $f(x,y) = q_a(u_v, p_a)$ and $f(x,y) = q_b(u_v, p_b)$ we obtain (exemplifying only with q_a for $u_v > 0$):

$$q_a - q_{a\oslash} = K_v\sqrt{p_s - p_{a\oslash}}(u_v - u_{v\oslash}) - \frac{K_v u_{v\oslash}}{2\sqrt{p_s - p_{a\oslash}}}(p_a - p_{a\oslash}) \tag{A.37}$$

$$\Delta q_a = K_{qa}\Delta u_v - K_{ca}\Delta p_a \tag{A.38}$$

$$\Delta q_b = K_{qb}\Delta u_v - K_{cb}\Delta p_b \tag{A.39}$$

$$K_{qa} = \begin{cases} K_v\sqrt{p_s - p_{a\oslash}}, & u_v > 0 \\ K_v\sqrt{p_{a\oslash} - p_t}, & u_v < 0 \end{cases} \tag{A.40}$$

$$K_{qb} = \begin{cases} K_v\sqrt{p_{b\oslash} - p_t}, & u_v > 0 \\ K_v\sqrt{p_s - p_{b\oslash}}, & u_v < 0 \end{cases} \tag{A.41}$$

$$K_{ca} = \begin{cases} \frac{K_v u_{v\oslash}}{2\sqrt{p_s - p_{a\oslash}}}, & u_v > 0 \\ \frac{-K_v u_{v\oslash}}{2\sqrt{p_{a\oslash} - p_t}}, & u_v < 0 \end{cases} \tag{A.42}$$

$$K_{cb} = \begin{cases} \frac{-K_v u_{v\oslash}}{2\sqrt{p_{b\oslash} - p_t}}, & u_v > 0 \\ \frac{K_v u_{v\oslash}}{2\sqrt{p_s - p_{b\oslash}}}, & u_v < 0 \end{cases} \tag{A.43}$$

$P_\oslash \rightarrow$ operating point;

$\Delta q_a \rightarrow$ linearized cylinder chamber a flow $[m^3/s]$;

$\Delta q_b \rightarrow$ linearized cylinder chamber b flow $[m^3/s]$;

$\Delta p_a \rightarrow$ linearized cylinder chamber a pressure $[Pa]$;

$p_a \rightarrow$ cylinder chamber a pressure $[Pa]$;

$p_{a\oslash} \rightarrow$ cylinder chamber a pressure at the operating point $[Pa]$;

$\Delta p_b \rightarrow$ linearized cylinder chamber b pressure $[Pa]$;

$p_b \rightarrow$ cylinder chamber b pressure $[Pa]$;

$p_{b\oslash} \rightarrow$ cylinder chamber b pressure at the operating point $[Pa]$;

$\Delta u_v \rightarrow$ position of the spool of the linearized valve $[A]$;

$u_v \rightarrow$ valve spool position $[A]$;

$u_{v\oslash} \rightarrow$ valve spool position at operating point $[A]$;

$p_s \rightarrow$ pump pressure $[Pa]$;

$p_t \rightarrow$ tank pressure $[Pa]$;

$K_v \rightarrow$ valve gain;

K_{qa} and K_{qb} → flow gains, to better understand what these gains represent, see A.8.1;

K_{ca} and K_{cb} → flow-pressure coefficients, to better understand what these gains represent, see A.8.1.

There are also two other important constants called *pressure sensitivities*:

$$K_{pa} = \begin{cases} \frac{2K_v(p_s - p_{a\oslash})}{u_{v\oslash}}, & u_v > 0 \\ \frac{-2K_v(p_{a\oslash} - p_t)}{u_{v\oslash}}, & u_v > 0 \end{cases} \tag{A.44}$$

$$K_{pb} = \begin{cases} \frac{-2K_v(p_{b\oslash} - p_t)}{u_{v\oslash}}, & u_v > 0 \\ \frac{2K_v(p_s - p_{b\oslash})}{u_{v\oslash}}, & u_v < 0 \end{cases} \tag{A.45}$$

K_v → valve gain;

u_v → valve spool position $[A]$;

$u_{v\oslash}$ → valve spool position at operating point $[A]$;

$p_{a\oslash}$ → cylinder chamber a pressure at the operating point $[Pa]$;

$p_{b\oslash}$ → cylinder chamber b pressure at the operating point $[Pa]$;

p_s → pump pressure $[Pa]$;

p_t → tank pressure $[Pa]$;

K_{pa} e K_{pb} → pressure sensitivities.

Using the basic flow equation for steady state (*Flow = Area x Velocity*),

$$q_a = A_p \dot{x}_p \tag{A.46}$$

$$q_b = \alpha A_p \dot{x}_p \tag{A.47}$$

combining it with the two non-linear flow equations of q_a and q_b and linearizing the resulting equations:

$$\Delta p_a = \frac{1}{1+\alpha^3} \Delta p_l \tag{A.48}$$

$$\Delta p_b = \frac{-\alpha^2}{1+\alpha^3} \Delta p_l \tag{A.49}$$

Derivation of (A.48) and (A.49): from the equations (A.46) and (A.47), we have:

$$q_b = \alpha q_a \tag{A.50}$$

For $u_v > 0$:

$$\begin{aligned}
K_v u_v \sqrt{p_b - p_t} &= \alpha K_v u_v \sqrt{p_s - p_a} \\
p_b - p_t &= \alpha^2 (p_s - p_a) \\
-p_b + p_t &= \alpha^2 (p_a - p_s) \\
-\alpha p_b + \alpha p_t + p_a &= \alpha^3 (p_a - p_s) + p_a \\
p_a - \alpha p_b + \alpha p_t &= (\alpha^3 + 1) p_a - \alpha^3 p_s \\
p_l + \alpha p_t + \alpha^3 p_s &= (\alpha^3 + 1) p_a \\
p_a(p_l) &= \frac{1}{1+\alpha^3} p_l + \frac{\alpha p_t + \alpha^3 p_s}{1+\alpha^3}
\end{aligned} \tag{A.51}$$

Therefore, we see that: $\frac{\partial p_a}{\partial p_l} = \frac{1}{1+\alpha^3}$, and the Taylor expansion (1st order) of (A.51) is given by (A.48). The same goes for $u_v < 0$. Now, for (A.49), again with $u_v > 0$:

$$\begin{aligned}
K_v u_v \sqrt{p_b - p_t} &= \alpha K_v u_v \sqrt{p_s - p_a} \\
p_b - p_t &= \alpha^2 (p_s - p_a) \\
\frac{p_b}{\alpha^2} - \frac{p_t}{\alpha^2} + \alpha p_b &= p_s - p_a + \alpha p_b \\
\frac{p_b}{\alpha^2} - \frac{p_t}{\alpha^2} + \alpha p_b &= p_s - p_l \\
p_b - p_t + \alpha^3 p_b &= \alpha^2 (p_s - p_l) \\
(1+\alpha^3) p_b &= -\alpha^2 p_l + \alpha^2 p_s + p_t \\
p_b(p_l) &= \frac{-\alpha^2}{1+\alpha^3} p_l + \frac{\alpha^2 p_s + p_t}{1+\alpha^3}
\end{aligned} \tag{A.52}$$

Analogously to $p_a(p_l)$, we have here $\frac{\partial p_b}{\partial p_l} = \frac{-\alpha^2}{1+\alpha^3}$ and the derivation of (A.49) by Taylor expansion of (A.52), also valid for $u_v < 0$.

Making a further simplification, the volumes of the cylinder chambers can be considered constant, so that this is possible, the velocity of the piston ($\dot{x}_{p\oslash}$) and the position of the spool ($u_{v\oslash}$) must be zero at the operating point. This way it is possible to write the linearized hydraulic force equation.

$$\Delta \dot{f}_h = \frac{A_p \beta_e}{v_{a\oslash}} (\Delta q_a - A_p \Delta \dot{x}_p) - \alpha \frac{A_p \beta_e}{v_{b\oslash}} (-\Delta q_b + \alpha A_p \Delta \dot{x}_p) \tag{A.53}$$

$\Delta f_h \rightarrow$ linearized hydraulic force $[Pa]$;

$A_p \rightarrow$ piston area $[m^2]$;

$\beta_e \rightarrow$ oil Bulk Modulus $[Pa]$;

$v_{a\oslash} \rightarrow$ cylinder chamber a volume at operating point $[m^3]$;

$v_{b\oslash} \rightarrow$ cylinder chamber b volume at operating point $[m^3]$;

$\Delta q_a \rightarrow$ linearized cylinder chamber a flow $[m^3/s]$;

$\Delta q_b \rightarrow$ linearized cylinder chamber b flow $[m^3/s]$;

$\Delta x_p \rightarrow$ linearized piston position $[m]$;

$\alpha \rightarrow$ ratio factor between piston areas.

Replacing the equations of Δp_a and Δp_b into the equations of Δq_a and Δq_b and these in $\Delta \dot{f}_h$:

$$\Delta \dot{f}_h = K_{\dot{x}_p} \Delta \dot{x}_p + K_{u_v} \Delta u_v + K_{f_h} \Delta f_h \tag{A.54}$$

$$K_{\dot{x}_p} = -{A_p}^2 \beta_e \left(\frac{1}{v_{a\oslash}} + \frac{\alpha^2}{v_{b\oslash}} \right) \tag{A.55}$$

$$K_{u_v} = A_p \beta_e \left(\frac{K_{qa}}{v_{a\oslash}} + \frac{\alpha K_{qb}}{v_{b\oslash}} \right) \tag{A.56}$$

$$K_{f_h} = \frac{-\beta_e}{1+\alpha^3} \left(\frac{K_{ca}}{v_{a\oslash}} - \frac{\alpha^3 K_{cb}}{v_{b\oslash}} \right) \tag{A.57}$$

Checking:

$$\Delta \dot{f}_h = \frac{A_p \beta_e}{v_{a\oslash}} \left(\Delta q_a - A_p \Delta \dot{x}_p \right) - \alpha \frac{A_p \beta_e}{v_{b\oslash}} \left(-\Delta q_b + \alpha A_p \Delta \dot{x}_p \right)$$

$$\Delta \dot{f}_h = \frac{A_p \beta_e}{v_{a\oslash}} \left(K_{qa} \Delta u_v - K_{ca} \Delta p_a - A_p \Delta \dot{x}_p \right) - \alpha \frac{A_p \beta_e}{v_{b\oslash}} \left(-K_{qb} \Delta u_v + K_{cb} \Delta p_b + \alpha A_p \Delta \dot{x}_p \right)$$

$$\Delta \dot{f}_h = \left(\frac{A_p \beta_e K_{qa}}{v_{a\oslash}} + \alpha \frac{A_p \beta_e K_{qb}}{v_{b\oslash}} \right) \Delta u_v - \left(\frac{{A_p}^2 \beta_e}{v_{a\oslash}} + \alpha^2 \frac{{A_p}^2 \beta_e}{v_{b\oslash}} \right) \Delta \dot{x}_p$$

$$- \left(\frac{A_p \beta_e K_{ca}}{v_{a\oslash}} \frac{1}{1+\alpha^3} + \alpha \frac{A_p \beta_e K_{cb}}{v_{b\oslash}} \frac{(-\alpha^2)}{1+\alpha^3} \right) \Delta p_l$$

$$\Delta \dot{f}_h = K_{u_v} \Delta u_v + K_{\dot{x}_p} \Delta \dot{x}_p - \frac{A_p \beta_e}{1+\alpha^3} \left(\frac{K_{ca}}{v_{a\oslash}} - \frac{\alpha^3 K_{cb}}{v_{b\oslash}} \right) \frac{\Delta f_h}{A_p}$$

$$\Delta \dot{f}_h = K_{\dot{x}_p} \Delta \dot{x}_p + K_{u_v} \Delta u_v + K_{f_h} \Delta f_h$$

Equation A.54 can be represented by the block diagram below:

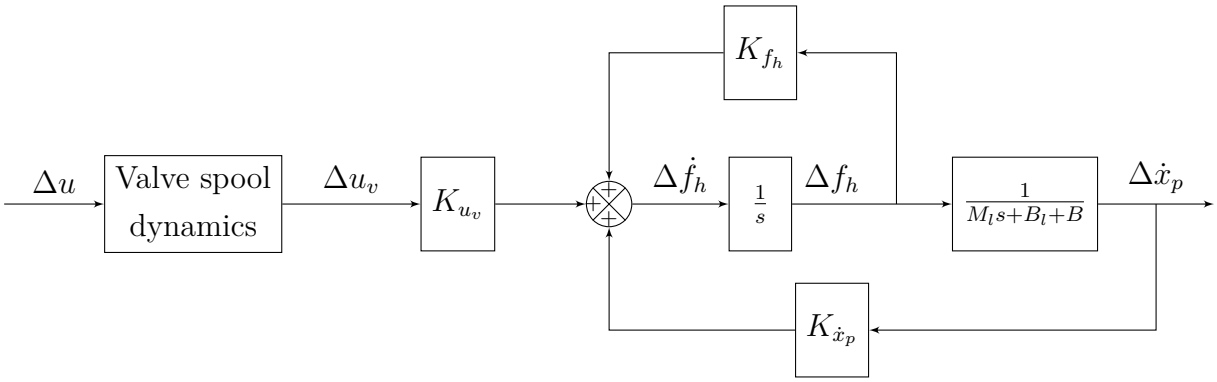

In transfer function form we can write:

$$\frac{\Delta f_h}{\Delta u} = \left(\frac{1}{\frac{1}{\omega_v^2} s^2 + \frac{2D_v}{\omega_v} s + 1} \right) \left(\frac{K_{u_v}(M_l s + B_l + B)}{(s - K_{f_h})(M_l s + B_l + B) - K_{\dot{x}_p}} \right) \tag{A.58}$$

$\Delta f_h \rightarrow$ linearized hydraulic force $[Pa]$;

$\omega_v \rightarrow F_v = \frac{\omega_v}{2\pi}$: valve bandwidth $[Hz]$;

$D_v \rightarrow$ valve spool damping

$\Delta u \rightarrow$ valve control signal $[A]$;

$M_l \rightarrow$ load mass $[kg]$;

$B_l \rightarrow$ load viscous friction coefficient $[Ns/m]$;

$B \rightarrow$ piston viscous friction coefficient $[Ns/m]$;

Note that for the previous case the variable of interest is *hydraulic force*. If the force of interest is the *load force*, the friction of the piston of the system block must be removed:

$$\Delta \dot{f} = \Delta \dot{f}_h - B \Delta \ddot{x}_p \tag{A.59}$$

Equation A.59 can be represented by the block diagram below:

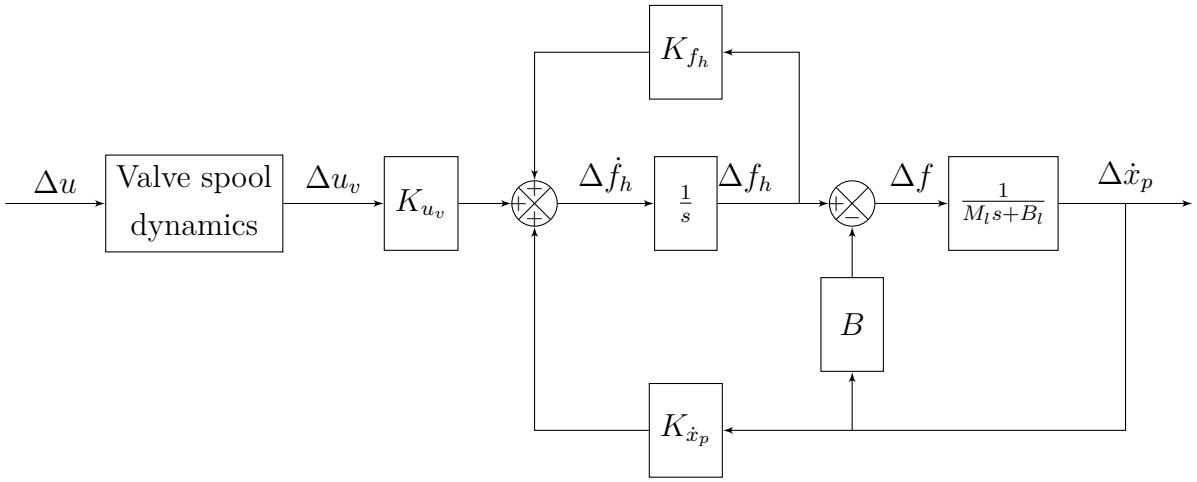

In transfer function form we can write:

$$\frac{\Delta f}{\Delta u} = \left(\frac{1}{\frac{1}{\omega_v^2} s^2 + \frac{2D_v}{\omega_v} s + 1} \right) \left(\frac{K_{u_v}(M_l s + B_l)}{(s - K_{f_h})(M_l s + B_l + B) - K_{\dot{x}_p}} \right) \tag{A.60}$$

A.6 Velocity feedback

When a spring mass system moves, an intrinsic velocity feedback appears in the modeling, which generates performance problems.

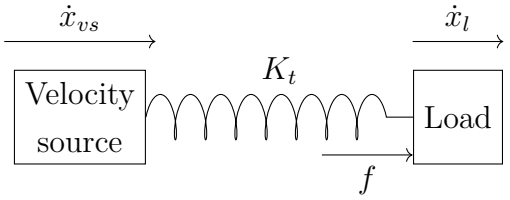

Therefore:

$$\dot{f} = K_t(\dot{x}_{vs} - \dot{x}_l) \tag{A.61}$$

In block diagram form:

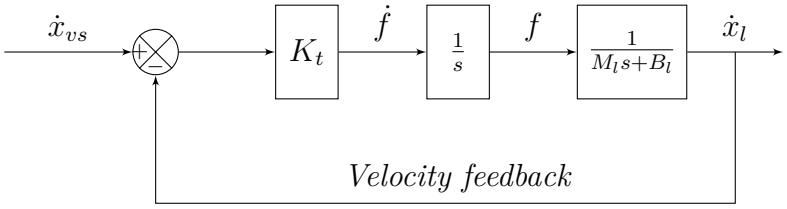

In the form of transfer function:

$$\frac{f}{\dot{x}_{vs}} = \frac{K_t(M_l s + B_l)}{s(M_l s + B_l) + K_t} \tag{A.62}$$

The fact that the load dynamics pole appears as zero in the force dynamics means that the controller gain and system performance are limited to the frequency of this zero. The modeling shown above applies to any system. Below is the application in hydraulic systems.

It is possible to manipulate the hydraulic force dynamics formula (Equation A.31), and replace the terms outside the parentheses with constants called hydraulic transmission stiffness:

$$\dot{f}_h = \frac{A_p \beta_e}{v_a}(q_a - A_p \dot{x}_p) - \alpha \frac{A_p \beta_e}{v_b}(-q_b + \alpha A_p \dot{x}_p) \tag{A.63}$$

$$\dot{f}_h = K_{th_a}(q_a - A_p \dot{x}_p) - K_{th_b}(-q_b + \alpha A_p \dot{x}_p) \tag{A.64}$$

$f_h \rightarrow$ hydraulic force $[Pa]$;

$K_{th_a} \rightarrow$ hydraulic transmission stiffness of cylinder chamber a $[Pa/m]$;

$K_{th_b} \rightarrow$ hydraulic transmission stiffness of cylinder chamber b $[Pa/m]$;

$A_p \rightarrow$ piston area $[m^2]$;

$\beta_e \rightarrow$ oil Bulk Modulus $[Pa]$;

$v_a \rightarrow$ cylinder chamber a volume $[m^3]$;

$v_b \rightarrow$ cylinder chamber b volume $[m^3]$;

$q_a \rightarrow$ cylinder chamber a flow $[m^3/s]$;

$q_b \rightarrow$ cylinder chamber b flow $[m^3/s]$;

$x_p \rightarrow$ piston position $[m]$;

$\alpha \rightarrow$ ratio factor between piston areas.

These hydraulic springs can be simplified to a single equivalent spring. Taking into account that the two chambers act like springs in parallel:

$$K_{th} = K_{th_a} + K_{th_b} \tag{A.65}$$

$$K_{th} = A_p \beta_e \left(\frac{1}{v_a} + \frac{\alpha}{v_b}\right) \tag{A.66}$$

$$\dot{f}_h = K_{th}(q_e - A_e\dot{x}_p) \tag{A.67}$$

$f_h \rightarrow$ hydraulic force $[Pa]$;

$K_{th} \rightarrow$ hydraulic transmission stiffness equivalent $[Pa/m]$;

$K_{th_a} \rightarrow$ hydraulic transmission stiffness of cylinder chamber a $[Pa/m]$;

$K_{th_b} \rightarrow$ hydraulic transmission stiffness of cylinder chamber b $[Pa/m]$;

$A_p \rightarrow$ piston area $[m^2]$;

$\beta_e \rightarrow$ oil Bulk Modulus $[Pa]$;

$v_a \rightarrow$ cylinder chamber a volume $[m^3]$;

$v_b \rightarrow$ cylinder chamber b volume $[m^3]$;

$q_e \rightarrow$ equivalent cylinder flow $[m^3/s]$;

$A_e \rightarrow$ equivalent piston area $[m^2]$;

$x_p \rightarrow$ piston position $[m]$.

The same relationship present in Equation A.61 can be seen in EquationA.67, with the velocity of the load (in this case that of the piston) appearing in the formulation, which will generate feedback of velocity in the system.

$$q_e = \frac{v_b q_a + \alpha v_a q_b}{v_b + \alpha v_a} \tag{A.68}$$

$$A_e = A_p\left(\frac{v_b + \alpha^2 v_a}{v_b + \alpha v_a}\right) \tag{A.69}$$

$A_p \rightarrow$ piston area $[m^2]$;

$v_a \rightarrow$ cylinder chamber a volume $[m^3]$;

$v_b \rightarrow$ cylinder chamber b volume $[m^3]$;

$q_a \rightarrow$ cylinder chamber a flow $[m^3/s]$;

$q_b \rightarrow$ cylinder chamber b flow $[m^3/s]$;

$\alpha \rightarrow$ ratio factor between piston areas.

Linearizing the system:

$$\Delta q_e = K_{qe}\Delta u_v + K_{ce}\Delta p_l \tag{A.70}$$

$$K_{qe} = \frac{v_{b\oslash} K_{qa} + \alpha v_{a\oslash} K_{qb}}{v_{b\oslash} + \alpha v_{a\oslash}} \tag{A.71}$$

$$K_{ce} = \frac{1}{1+\alpha^3} \left(\frac{v_{b\oslash} K_{ca} - \alpha^3 v_{a\oslash} K_{cb}}{v_{b\oslash} + \alpha v_{a\oslash}} \right) \tag{A.72}$$

$$\Delta \dot{f}_h = K_{th\oslash} (\Delta q_e - A_{e\oslash} \Delta \dot{x}_p) \tag{A.73}$$

$\Delta q_e \rightarrow$ linearized equivalent flow $[m^3/s]$;

$\Delta u_v \rightarrow$ position of the spool of the linearized valve $[A]$;

$\Delta p_l \rightarrow$ load pressure linearized $[Pa]$;

$K_{qe} \rightarrow$ *equivalent flow gain* $[m^3 s^{-1} A^{-1}]$;

$K_{ce} \rightarrow$ *equivalent flow-pressure coefficient* $[m^3 s^{-1} Pa^{-1}]$;

K_{qa} and $K_{qb} \rightarrow$ flow gains;

K_{ca} and $K_{cb} \rightarrow$ flow-pressure coefficients;

$v_{a\oslash} \rightarrow$ cylinder chamber a volume at operating point $[m^3]$;

$v_{b\oslash} \rightarrow$ cylinder chamber b volume at operating point $[m^3]$;

$\alpha \rightarrow$ ratio factor between piston areas;

$\Delta f_h \rightarrow$ linearized hydraulic force $[Pa]$;

$K_{th\oslash} \rightarrow$ hydraulic transmission stiffness equivalent at operating point $[Pa/m]$;

$A_{e\oslash} \rightarrow$ equivalent piston area at operating point $[m^2]$;

$\Delta x_p \rightarrow$ linearized piston position $[m]$.

Representing Equation A.73 in the form of a block diagram:

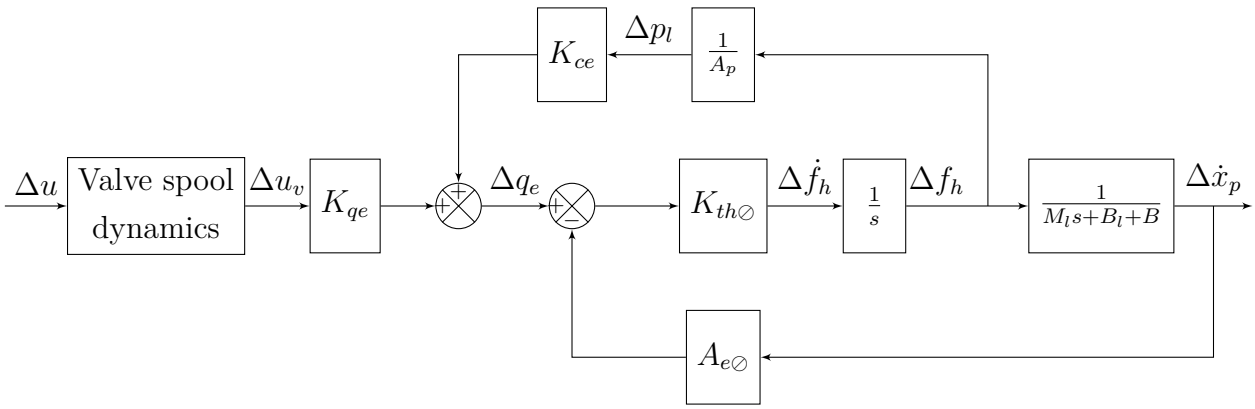

As in the general case, it is possible to see the velocity feedback that appears in the diagram. In transfer function form (ignoring valve dynamics):

$$\frac{\Delta f_h}{\Delta u_v} = \frac{K_{th\oslash} K_{qe}(M_l s + B_l + B)}{(M_l s + B_l + B)\left(s - \frac{K_{th\oslash} K_{ce}}{Ap}\right) + K_{th\oslash} A_{e\oslash}} \tag{A.74}$$

For the load force:

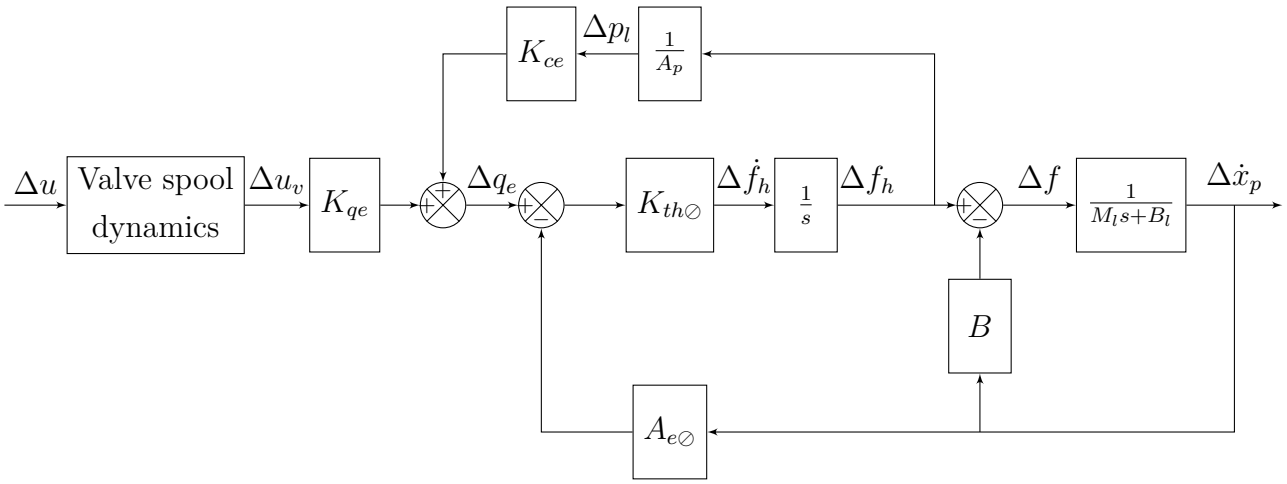

In transfer function form:

$$\frac{\Delta f}{\Delta u_v} = \frac{K_{th\oslash} K_{qe}(M_l s + B_l)}{(M_l s + B_l + B)\left(s - \frac{K_{th\oslash} K_{ce}}{Ap}\right) + K_{th\oslash} A_{e\oslash}} \tag{A.75}$$

A.7 Velocity compensation + PID - Force controller

As seen in Section A.6, velocity feedback is intrinsic to the system and degrades the performance of a controller. Therefore, so that this feedback does not disrupt the system, it is necessary to compensate for it. If we observe Equation A.61 it is possible to see that when providing, with the velocity source, an extra velocity equal to the load velocity, the velocity feedback disappears. That is, making $\dot{x}_{ex} = \dot{x}_l$:

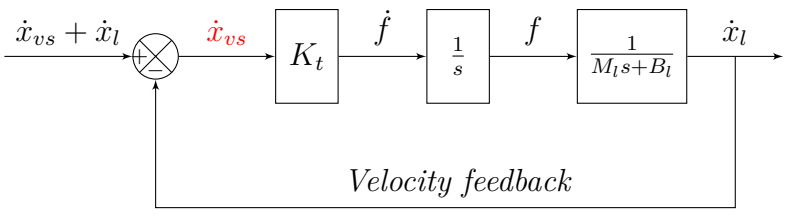

$$\dot{f} = K_t[(\dot{x}_{vs} + \dot{x}_{ex}) - \dot{x}_l] = K_t \dot{x}_{vs} \tag{A.76}$$

Algebraically, this compensation has the effect of canceling the K_t term in the FT denominator, opening the *loop*:

$$\frac{f}{\dot{x}_{vs}} = \frac{K_t(M_l s + B_l)}{s(M_l s + B_l) + K_t} = \frac{K_t}{s} \tag{A.77}$$

In the hydraulic case, the equivalent of generating extra velocity is generating an extra flow proportional to the piston velocity, for this an extra signal must be generated for the valve.

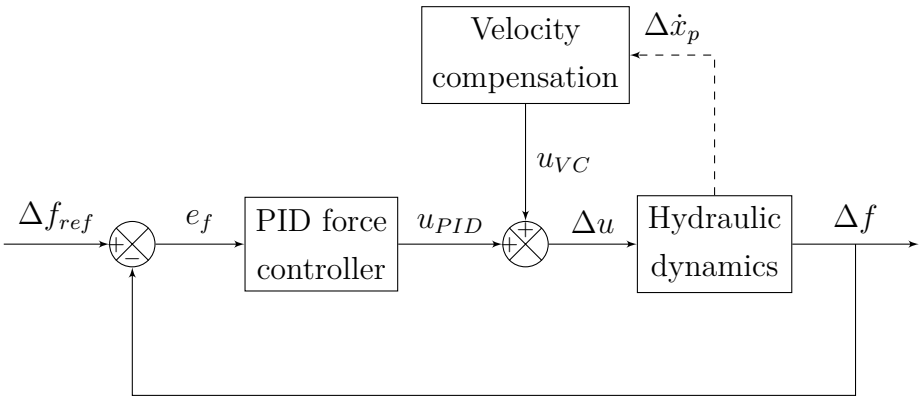

If the variable to be controlled is Δf_h, then:

$$u_{VC} = \frac{A_{e\oslash}\Delta\dot{x}_p}{K_{qe}} \tag{A.78}$$

If it is Δf:

$$u_{VC} = \frac{(A_{e\oslash} - BK_{ce})\Delta\dot{x}_p}{K_{qe}} + \frac{B\Delta\ddot{x}_p}{K_{qe}K_{th\oslash}} \tag{A.79}$$

$u_{VC} \rightarrow$ extra control signal to compensate for velocity feedback;

$A_{e\oslash} \rightarrow$ equivalent piston area at operating point $[m^2]$;

$B \rightarrow$ viscous piston damping;

$K_{qe} \rightarrow$ *equivalent flow gain* $[m^3 s^{-1} A^{-1}]$;

$K_{ce} \rightarrow$ *equivalent flow-pressure coefficient* $[m^3 s^{-1} Pa^{-1}]$;

$K_{th\oslash} \rightarrow$ hidraulic transmission stiffness equivalent at the operating point $[Pa/m]$;

$\Delta x_p \rightarrow$ linearized piston position [m].

Given that accelerations are difficult values to obtain experimentally due to noise, the second term of the previous equation can be neglected without major harm to performance.

A.8 Valve leakage

Considering the following Figure 55, small leaks between the valve chambers can be considered, so the flow rates in the chambers a, b, the return to the tank and the pump supply are described by the equations below:

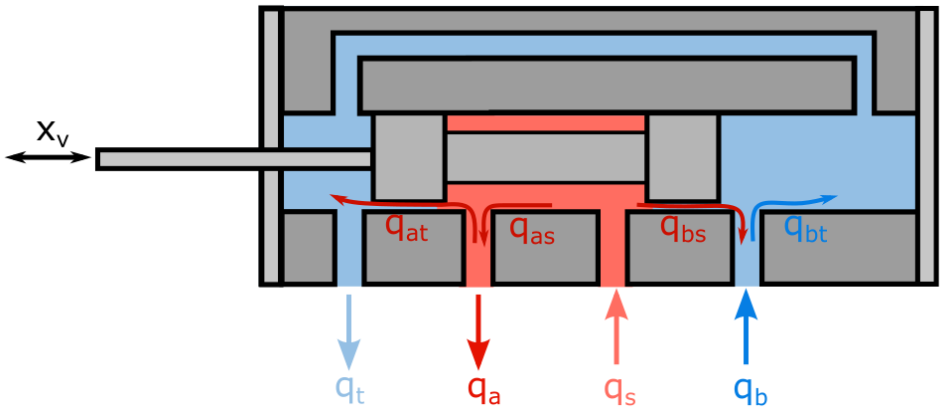

Figure 55 – Valve leakage

$$q_s = q_t + (q_a - q_b) \rightarrow \begin{cases} q_a = q_{as} - q_{at} \\ q_b = q_{bt} - q_{bs} \\ q_s = q_{as} + q_{bs} \\ q_t = q_{as} + q_{bs} \end{cases} \tag{A.80}$$

$q_a \rightarrow$ valve cylinder chamber a port flow $[m^3/s]$;

$q_b \rightarrow$ valve cylinder chamber b port flow $[m^3/s]$;

$q_s \rightarrow$ valve suplly s port flow (pump) $[m^3/s]$;

$q_t \rightarrow$ valve tank t port flow $[m^3/s]$;

$q_{as} \rightarrow$ pump supply flow to cylinder chamber a $[m^3/s]$;

$q_{bs} \rightarrow$ pump supply flow to cylinder chamber b $[m^3/s]$;

$q_{at} \rightarrow$ flow from the cylinder chamber a to the return in the tank $[m^3/s]$;

$q_{bt} \rightarrow$ flow from the cylinder chamber b to the return in the tank $[m^3/s]$;

The difference between this modeling and (BOAVENTURA) are these leaks. The effective flow at each control port involves two distinct flow regimes: orifice flow and leakage. Consider, for example, the flows associated with the chamber a of a servovalve for a positive displacement of the spool, as shown in Figure 55. The flow rate at the supply orifice of this port is given by the orifice equation, as shown in Equation A.82

Orifice equation for an ideal valve:

$$q = K\sqrt{\Delta p}x \tag{A.81}$$

$q \rightarrow$ orifice flow $[m^3/s]$;

$K \rightarrow$ valve gain;

$\Delta p \rightarrow$ pressure drop across the orifice $[Pa]$

$x \rightarrow$ orifice opening $[m]$

$$q_{as} = \begin{cases} K_{as}\sqrt{p_s - p_a}(x_{v0} + x_v), & x_v \geq 0 \\ K_{as}\sqrt{p_s - p_a}\frac{x_{v0}^2}{x_{v0} - k_{as}x_v}, & x_v < 0 \end{cases} \tag{A.82}$$

Where the parameter x_{v0} is responsible for the leak at $x = 0$. Note that x_{v0} is equivalent to a spool offset that would result in the same amount of flow in a non-leaking servo valve as the leak in a leaking servo valve with a centered spool. The flow rate at the chamber tank return orifice a cannot be expressed using a simple orifice flow equation, Equation A.81. Larger positive spool displacements increase the length of the leak flow path to the left of the chamber a, therefore increasing flow resistance. The leak path is the result of the overlap between the valve body and the spool positioning, which forms a small gap ring.

The flow through this ring, however, is only laminar for a new valve and quickly becomes turbulent due to use, as the abrasive materials present in the fluid cause erosion at the edges of the orifice, increasing its contact areas. As leakage resistance increases at larger valve openings, leakage is inversely proportional to spool displacement. The flow rate on the return side of the chamber tank a can therefore be expressed as in Equation A.83.

$$q_{at} = \begin{cases} K_{at}\sqrt{p_a - p_t}\frac{x_{v0}^2}{x_{v0} + k_{at}x_v}, & x_v \geq 0 \\ K_{at}\sqrt{p_a - p_t}(x_{v0} - x_v), & x_v < 0 \end{cases} \tag{A.83}$$

The term x_{v0} is added again to explain the presence of a turbulent leak when the spool displacement is zero. The value of the parameter k_{at} determines the flow resistance in the leak path in the overlapping region as a function of spool displacement.

The above relationships for orifice and leakage flows in the servovalve chambers form the basis of the servovalve flow model. For negative displacements of the spool, the flow relations are changed, as now the leak path is formed on the pump side and the turbulent orifice flow is on the tank side. Applying similar reasoning to each orifice, we obtain the following flow relationships for chamber b:

$$q_{bs} = \begin{cases} K_{bs}\sqrt{p_s - p_b}\frac{x_{v0}^2}{x_{v0}+k_{bs}x_v}, & x_v \geq 0 \\ K_{bs}\sqrt{p_s - p_b}(x_{v0} - x_v), & x_v < 0 \end{cases} \tag{A.84}$$

$$q_{bt} = \begin{cases} K_{bt}\sqrt{p_b - p_t}(x_{v0} + x_v), & x_v \geq 0 \\ K_{bt}\sqrt{p_b - p_t}\frac{x_{v0}^2}{x_{v0}-k_{bt}x_v}, & x_v < 0 \end{cases} \tag{A.85}$$

K_{as} → gain in pump flow to cylinder chamber a $[m^{5/2}/kg^{1/2}]$;

K_{bs} → gain in pump flow to cylinder chamber b $[m^{5/2}/kg^{1/2}]$;

K_{at} → flow gain from the chamber a of the cylinder to the tank $[m^{5/2}/kg^{1/2}]$;

K_{bt} → flow gain from cylinder chamber b to tank $[m^{5/2}/kg^{1/2}]$;

k_{as} → Leakage coefficient for pump flow to cylinder chamber a $[m^{5/2}/kg^{1/2}]$;

k_{bs} → Leakage coefficient for pump flow to cylinder chamber b $[m^{5/2}/kg^{1/2}]$;

k_{at} → Leakage coefficient for flow from cylinder chamber a to tank $[m^{5/2}/kg^{1/2}]$;

k_{bt} → Leakage coefficient for flow from cylinder chamber b to tank $[m^{5/2}/kg^{1/2}]$;

x_v → valve spool position $[m]$;

x_{v0} → equivalent orifice opening $[m]$;

p_a → cylinder chamber a pressure $[Pa]$;

p_b → cylinder chamber b pressure $[Pa]$;

p_s → pump pressure $[Pa]$;

p_t → tank pressure $[Pa]$;

A.8.1 Pressure sensitivity and internal leakage testing

The model above can be validated by comparing the measured and predicted flow characteristics of the servo valve. Among various characterizations, pressure sensitivity and internal leakage tests provide the most relevant information. These tests are among the standard tests performed on servo valves by manufacturers and their data is available in datasheets most of the time.

The pressure sensitivity test measures the variation in load pressure ($p_l = p_a - p_b$), with the chambers blocked ($q_a = q_b = 0$), as the spool moves to complete the cycle around $x_v = 0$. Due to internal leakage, the typical pressure sensitivity curve is shown in Figure 56, you can see the step, but the transition itself is smooth between saturations.

The internal leak test measures the total internal valve flow (q_s) from the pump supply chamber to the tank return chamber with chambers a and b blocked and the spool

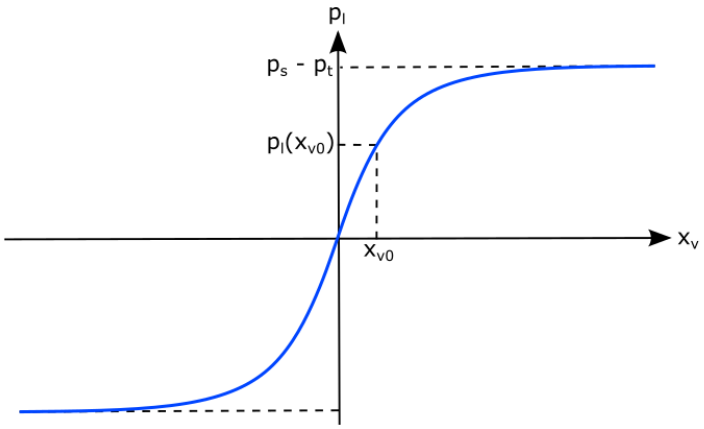

Figure 56 – Pressure sensitivity

position making the complete cycle. A typical leak flow curve shown in Figure 57 has a maximum at the neutral position of the spool and decreases rapidly with valve travel.

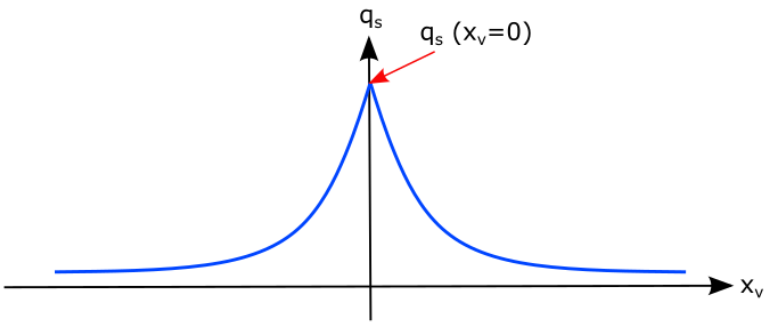

Figure 57 – Leakage flow

Since both tests are performed with the control chambers blocked (i.e. $q_a = q_b = 0$), we have that:

$$q_a = q_b = 0 \rightarrow \begin{cases} q_a = q_{as} - q_{at} = 0 \rightarrow q_{as} = q_{at} \\ q_b = q_{bt} - q_{bs} = 0 \rightarrow q_{bs} = q_{bt} \end{cases} \tag{A.86}$$

Then applying this condition between Equations A.82 and A.83 for the chamber a, and between Equations A.84 and A.85 to chamber b.

$$q_{as} = q_{at} \rightarrow \begin{cases} K_{as}\sqrt{p_s - p_a}(x_{v0} + x_v) = K_{at}\sqrt{p_a - p_t}\frac{x_{v0}^2}{x_{v0}+k_{at}x_v}, & x_v \geq 0 \\ K_{as}\sqrt{p_s - p_a}\frac{x_{v0}^2}{x_{v0}-k_{as}x_v} = K_{at}\sqrt{p_a - p_t}(x_{v0} - x_v), & x_v < 0 \end{cases} \tag{A.87}$$

$$q_{bs} = q_{bt} \rightarrow \begin{cases} K_{bs}\sqrt{p_s - p_b}\frac{x_{v0}^2}{x_{v0}+k_{bs}x_v} = K_{bt}\sqrt{p_b - p_t}(x_{v0} + x_v), & x_v \geq 0 \\ K_{bs}\sqrt{p_s - p_b}(x_{v0} - x_v) = K_{bt}\sqrt{p_b - p_t}\frac{x_{v0}^2}{x_{v0}-k_{bt}x_v}, & x_v < 0 \end{cases} \tag{A.88}$$

Starting with the chamber a, isolating p_a in Equation A.87,

$$\begin{cases} K_{as}^2(p_s - p_a)(x_{v0} + x_v)^2 = K_{at}^2(p_a - p_t)\left(\frac{x_{v0}^2}{x_{v0}+k_{at}x_v}\right)^2, & x_v \geq 0 \\ K_{as}^2(p_s - p_a)\left(\frac{x_{v0}^2}{x_{v0}-k_{as}x_v}\right)^2 = K_{at}^2(p_a - p_t)(x_{v0} - x_v)^2, & x_v < 0 \end{cases} \tag{A.89}$$

To facilitate, we will adopt the following symbolic simplifications:

$$\begin{cases} K_{as}^2(x_{v0} + x_v)^2 = A \\ K_{at}^2\left(\frac{x_{v0}^2}{x_{v0}+k_{at}x_v}\right)^2 = B \\ K_{as}^2\left(\frac{x_{v0}^2}{x_{v0}-k_{as}x_v}\right)^2 = C \\ K_{at}^2(x_{v0} - x_v)^2 = D \end{cases} \tag{A.90}$$

So, substituting Equation A.90 into Equation A.89, we have:

$$\begin{cases} Ap_s - Ap_a = Bp_a - Bp_t, & x_v \geq 0 \\ Cp_s - Cp_a = Dp_a - Dp_t, & x_v < 0 \end{cases} \tag{A.91}$$

Isolating p_a, we have:

$$p_a = \begin{cases} \frac{Ap_s+Bp_t}{A+B} = \frac{\frac{A}{B}p_s+p_t}{1+\frac{A}{B}}, & x_v \geq 0 \\ \frac{Cp_s+Dp_t}{C+D} = \frac{p_s+\frac{D}{C}p_t}{1+\frac{D}{C}}, & x_v < 0 \end{cases} \tag{A.92}$$

Let us us define the ratios as the parameters f_{ap} for the positive part of the spool position and f_{an} for the negative part:

$$f_{ap} = \frac{A}{B} = \frac{K_{as}^2(x_{v0} + x_v)^2}{K_{at}^2\left(\frac{x_{v0}^2}{x_{v0}+k_{at}x_v}\right)^2} = \left(\frac{K_{as}}{K_{at}}\right)^2\left[\left(1 + \frac{x_v}{x_{v0}}\right)\left(1 + \frac{k_{at}x_v}{x_{v0}}\right)\right]^2 \tag{A.93}$$

$$f_{an} = \frac{D}{C} = \frac{K_{at}^2(x_{v0} - x_v)^2}{K_{as}^2\left(\frac{x_{v0}^2}{x_{v0}-k_{as}x_v}\right)^2} = \left(\frac{K_{at}}{K_{as}}\right)^2\left[\left(1 - \frac{x_v}{x_{v0}}\right)\left(1 - \frac{k_{as}x_v}{x_{v0}}\right)\right]^2 \tag{A.94}$$

We then have:

$$p_a = \begin{cases} \frac{f_{ap}p_s+p_t}{1+f_{ap}}, & x_v \geq 0 \\ \frac{p_s+f_{an}p_t}{1+f_{an}}, & x_v < 0 \end{cases} \tag{A.95}$$

Repeating the same process for the chamber b, we then have:

$$p_b = \begin{cases} \frac{p_s + f_{bp} p_t}{1 + f_{bp}}, & x_v \geq 0 \\ \frac{f_{bn} p_s + p_t}{1 + f_{bn}}, & x_v < 0 \end{cases} \tag{A.96}$$

where:

$$f_{bp} = \left(\frac{K_{bt}}{K_{bs}}\right)^2 \left[\left(1 + \frac{x_v}{x_{v0}}\right)\left(1 + \frac{k_{bs} x_v}{x_{v0}}\right)\right]^2 \tag{A.97}$$

$$f_{bn} = \left(\frac{K_{bs}}{K_{bt}}\right)^2 \left[\left(1 - \frac{x_v}{x_{v0}}\right)\left(1 - \frac{k_{bt} x_v}{x_{v0}}\right)\right]^2 \tag{A.98}$$

If we replace Equations A.95 and A.96 in Equations A.87 and A.88, respectively, we have:

$$q_{as} = q_{at} \rightarrow \begin{cases} \frac{K_{as}\sqrt{p_s - p_t}(x_{v0} + x_v)}{\sqrt{1 + f_{ap}}}, & x_v \geq 0 \\ \frac{K_{at}\sqrt{p_s - p_t}(x_{v0} - x_v)}{\sqrt{1 + f_{an}}}, & x_v < 0 \end{cases} \tag{A.99}$$

$$q_{bs} = q_{bt} \rightarrow \begin{cases} \frac{K_{bt}\sqrt{p_s - p_t}(x_{v0} + x_v)}{\sqrt{1 + f_{bp}}}, & x_v \geq 0 \\ \frac{K_{bs}\sqrt{p_s - p_t}(x_{v0} - x_v)}{\sqrt{1 + f_{bn}}}, & x_v < 0 \end{cases} \tag{A.100}$$

For valves with chambers a and b blocked. If the valve is symmetrical, we can assume that the gains are equal, as are the leakage coefficients, that is:

$$K_{as} = K_{at} = K_{bs} = K_{bt} = K \tag{A.101}$$

$$k_{as} = k_{at} = k_{bs} = k_{bt} = k \tag{A.102}$$

Applying the Equations A.101 and A.102 in Equations A.93, A.94, A.97 and A.98, we have that:

$$\begin{aligned} f_{ap} &= f_{bp} \\ f_{an} &= f_{bn} \end{aligned} \tag{A.103}$$

How these relations associate the term $+x$ with positive spool displacements and $-x$ with negative spool displacements in Equations A.93, A.94, A.97 and A.98, they can be combined into a single expression $f(x)$:

$$f(x_v) = \left(1 + \frac{|x_v|}{x_{v0}}\right)^2 \left(1 + k\frac{|x_v|}{x_{v0}}\right)^2 \tag{A.104}$$

which is valid for both ($x_v \geq 0$) and ($x_v < 0$). Because the control chambers are blocked during the internal leakage test, the total feed flow $q_s(x_v)$ actually represents the internal leakage flow. Therefore, from Equation A.104, the internal leakage flow can be expressed as:

$$q_s(x_v) = q_{as} + q_{bs} = \frac{2K\sqrt{p_s - p_t}(x_{v0} + |x_v|)}{\sqrt{1 + f(x_v)}} \tag{A.105}$$

Similarly, using pressure relations Equations A.95 and A.96, an analytical relationship for the head pressure $p_l(x_v)$ can be expressed as:

$$p_l(x_v) = p_a - p_b = \frac{f(x_v) - 1}{f(x_v) + 1}(p_s - p_t)sgn(x_v) \tag{A.106}$$

which is valid during a pressure sensitivity test. Here $sgn(x_v)$ denotes the signal function. With these functions, we can then calculate the three parameters used in modeling (K, x_{v0}, k).

A.8.2 Determination of model parameters

The required data consists of the nominal flow values, the leakage rate for zero flow and the pressure sensitivity curve at a given pump supply pressure. The nominal (maximum) flow q_{max} is the flow obtained when the nominal input current I_{max} is applied at a given valve pressure drop. The nominal flow rate is generally specified for no-load condition ($p_l = 0$). The maximum leakage flow, which occurs at the spool's neutral position, is only a small percentage of the rated flow rate. Additionally, leakage decreases quickly with valve movement because the edges of the spool overlap the valve holes. Therefore, under conditions of nominal flow (q_{max},I_{max}) and no-load flow ($p_l = 0$) in the servovalve chambers, the leakage terms in Equations A.82, A.83, A.84 and A.85 can be ignored. The result is the classic servovalve flow model with the nominal flow values we have:

$$q_{max} = \frac{K}{\sqrt{2}}\sqrt{p_s - p_t}I_{max} \tag{A.107}$$

So the flow gain K is given by:

$$K = \frac{q_{max}\sqrt{2}}{\sqrt{p_s - p_t}I_{max}} \tag{A.108}$$

The equivalent hole opening x_{v0} is calculated using the expression in Equation A.105. Leakage flow rate at $x_v = 0$ it is given by:

$$q_s(x_v = 0) = \sqrt{2}K\sqrt{p_s - p_t}x_{v0} \tag{A.109}$$

We then have:

$$x_{v0} = \frac{q_s(x_v = 0)}{\sqrt{2}K\sqrt{p_s - p_t}} \tag{A.110}$$

Finally, the leakage coefficient k can be obtained from the pressure sensitivity expression, Equation A.106. The value of the pressure curve at $x_v = x_{v0}$ is given by:

$$p_l(x_{v0}) = \frac{4(1+k)^2 - 1}{4(1+k)^2 + 1}(p_s - p_t) \tag{A.111}$$

Solving the above equation we have:

$$k = \frac{1}{2}\sqrt{\frac{p_s - p_t + p_l(x_{v0})}{p_s - p_t - p_l(x_{v0})}} - 1 \tag{A.112}$$

Thus, with the manufacturer's parameters we were able to determine all the necessary parameters.

A.8.3 Final model

$$q_a = \begin{cases} K\left(\sqrt{p_s - p_a}(x_{v0} + x_v) - \sqrt{p_a - p_t}\frac{x_{v0}^2}{x_{v0}+kx_v}\right), & x_v \geq 0 \\ K\left(\sqrt{p_s - p_a}\frac{x_{v0}^2}{x_{v0}-kx_v} - \sqrt{p_a - p_t}(x_{v0} - x_v)\right), & x_v < 0 \end{cases} \tag{A.113}$$

$$q_b = \begin{cases} K\left(\sqrt{p_b - p_t}(x_{v0} + x_v) - \sqrt{p_s - p_b}\frac{x_{v0}^2}{x_{v0}+kx_v}\right), & x_v \geq 0 \\ K\left(\sqrt{p_b - p_t}\frac{x_{v0}^2}{x_{v0}-kx_v} - \sqrt{p_s - p_b}(x_{v0} - x_v)\right), & x_v < 0 \end{cases} \tag{A.114}$$

Linearizing:

$$\Delta q_a = \begin{cases} [K(\sqrt{p_s - p_{a\oslash}} + k\sqrt{p_{a\oslash} - p_t})]\Delta x_v + \left[-\frac{K}{2}\left(\frac{x_{v0}}{\sqrt{p_{a\oslash}-p_t}} + \frac{x_{v0}}{\sqrt{p_s-p_{a\oslash}}}\right)\right]\Delta p_a, & x_v \geq 0 \\ [K(k\sqrt{p_s - p_{a\oslash}} + \sqrt{p_{a\oslash} - p_t})]\Delta x_v + \left[-\frac{K}{2}\left(\frac{x_{v0}}{\sqrt{p_{a\oslash}-p_t}} + \frac{x_{v0}}{\sqrt{p_s-p_{a\oslash}}}\right)\right]\Delta p_a, & x_v < 0 \end{cases} \tag{A.115}$$

APPENDIX B – IDENTIFICATION VALIDATION

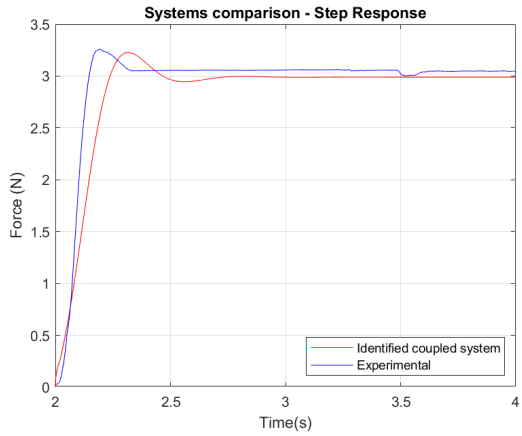

(a) PD

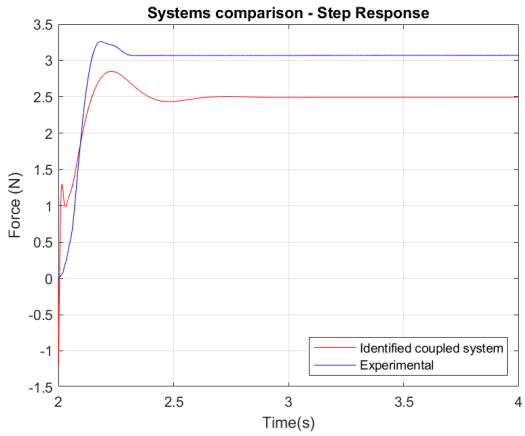

(b) PID

Figure 58 – Step responses validation - DC Motor

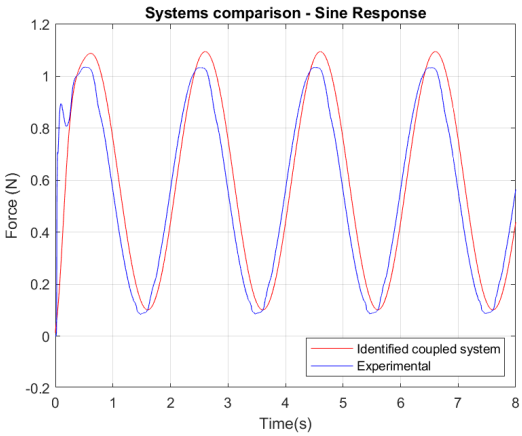

(a) PD

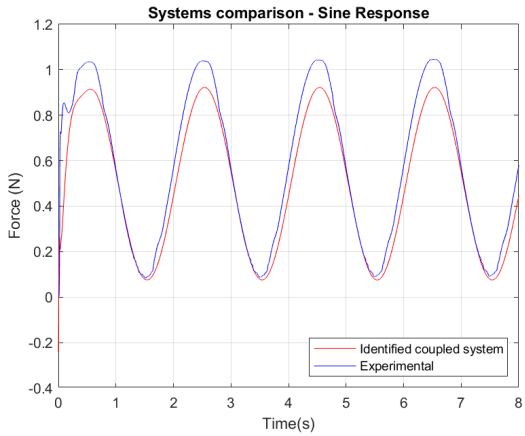

(b) PID

Figure 59 – Sine responses validation - DC Motor

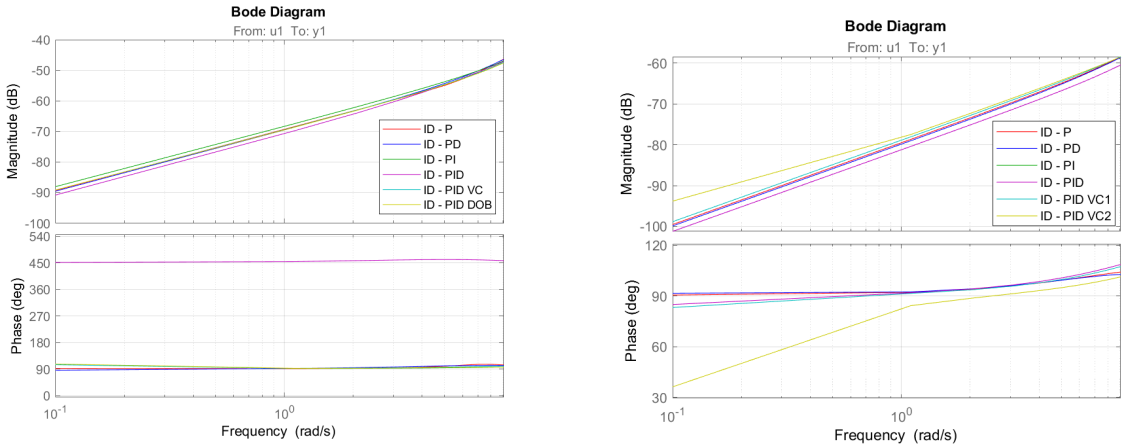

(a) LinMot (b) Hydraulic actuator

Figure 60 – Load identification IC2D experiments

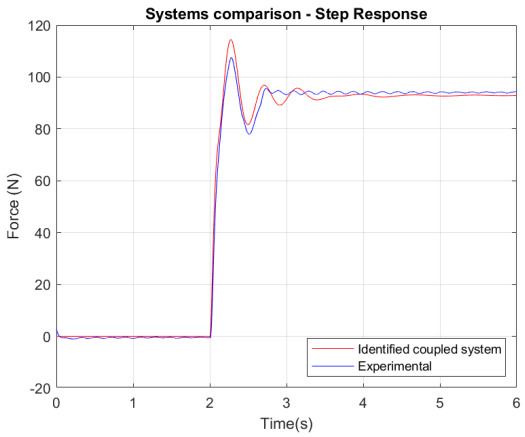

(a) P

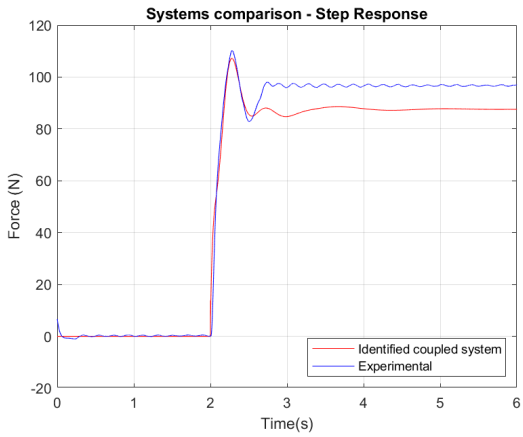

(b) PD

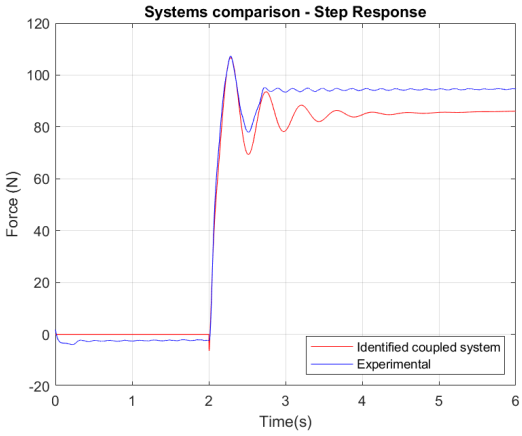

(c) PI

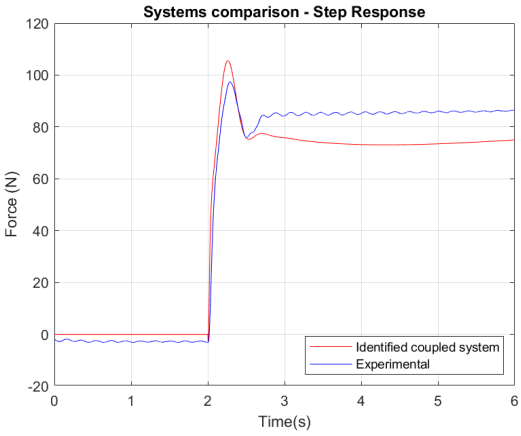

(d) PID

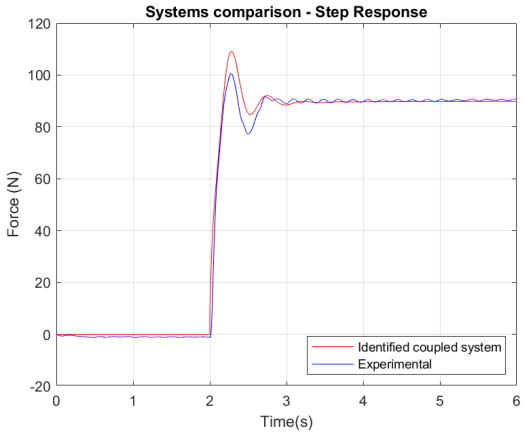

(e) PID + VC

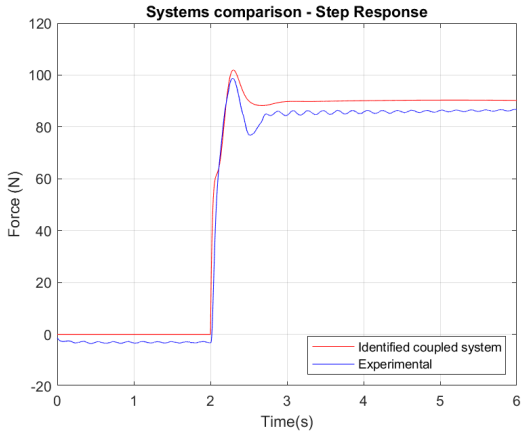

(f) PID + DOB

Figure 61 – Step responses validation - LinMot

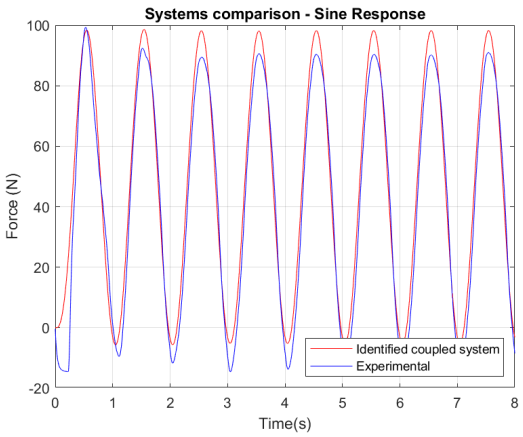

(a) P

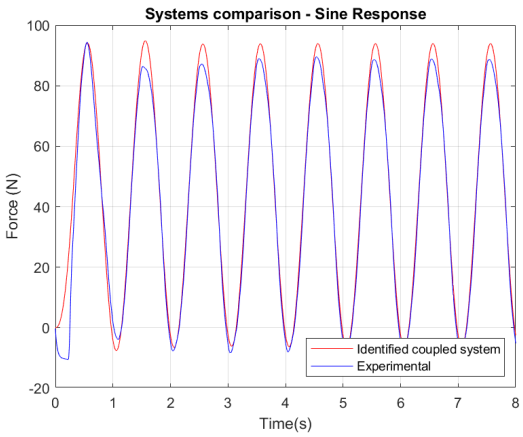

(b) PD

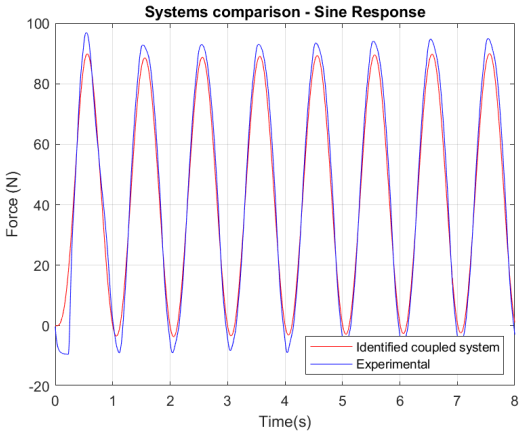

(c) PI

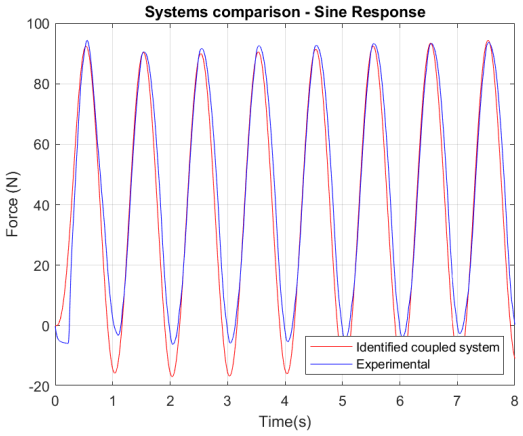

(d) PID

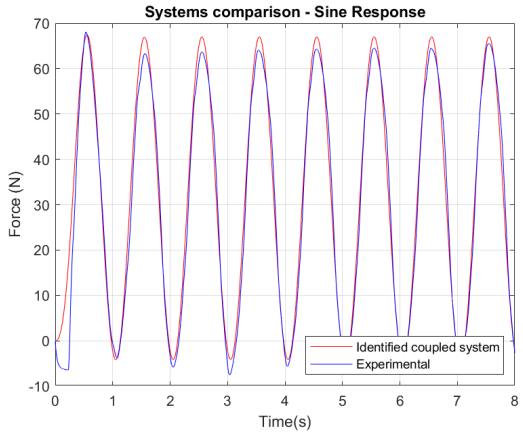

(e) PID + VC

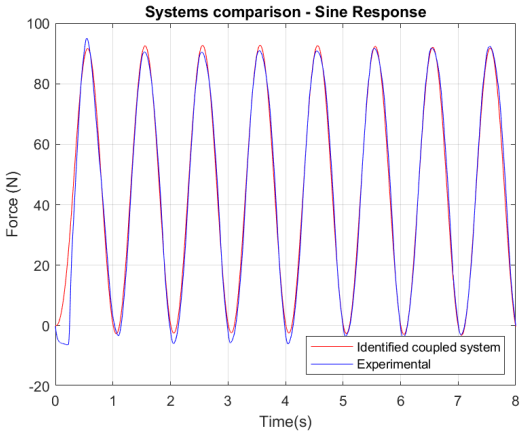

(f) PID + DOB

Figure 62 – Sine responses validation - LinMot

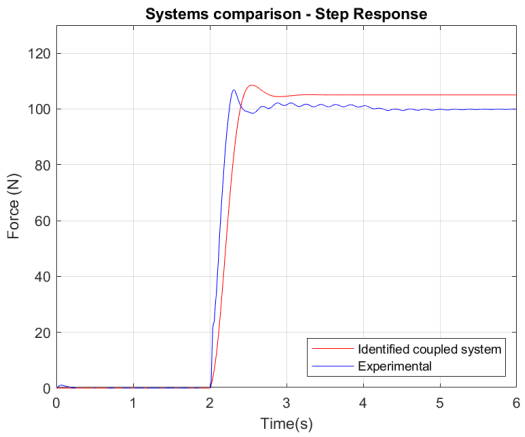

(a) P

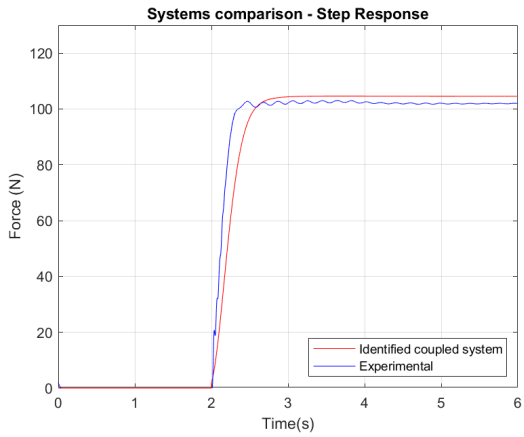

(b) PD

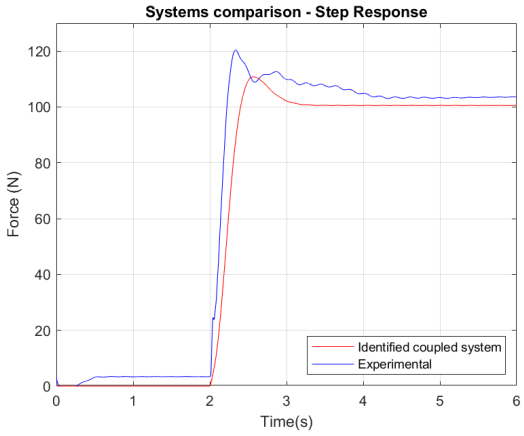

(c) PI

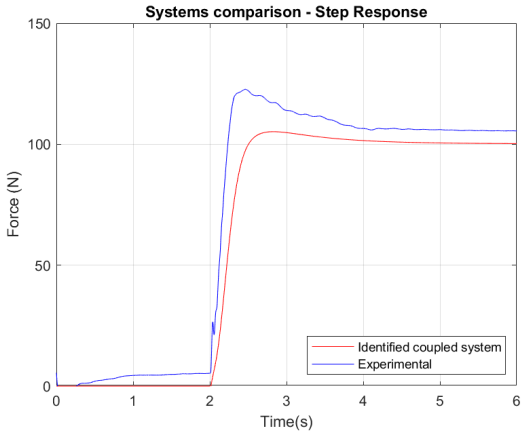

(d) PID

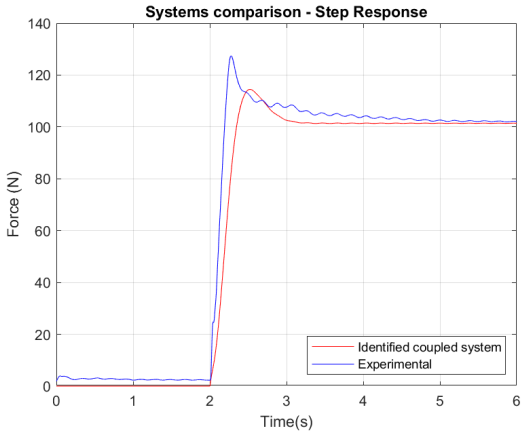

(e) PID + VC1

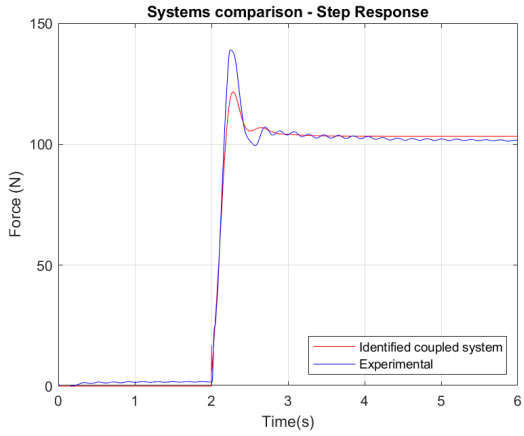

(f) PID + VC2

Figure 63 – Step responses validation - Hydraulic cylinder

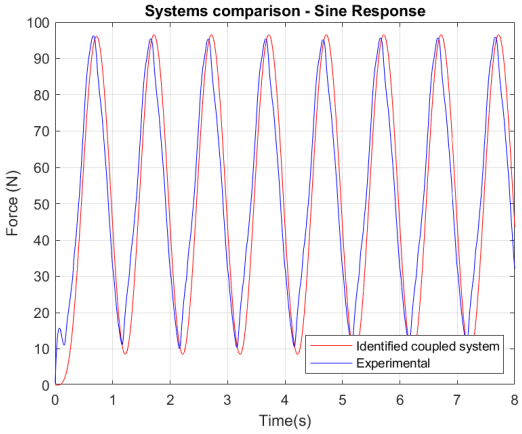

(a) P

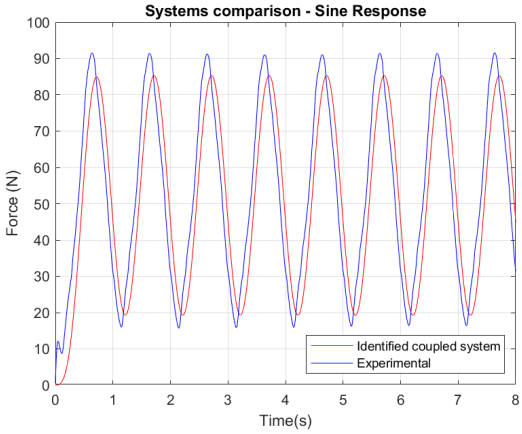

(b) PD

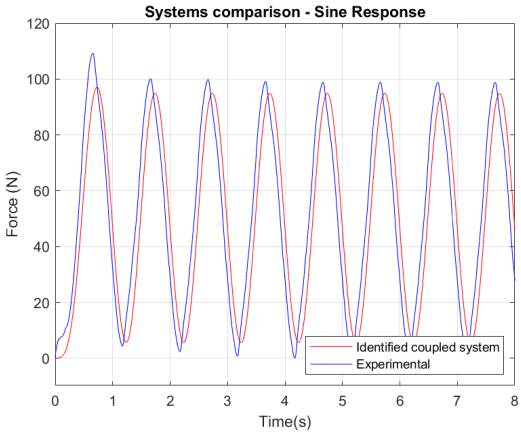

(c) PI

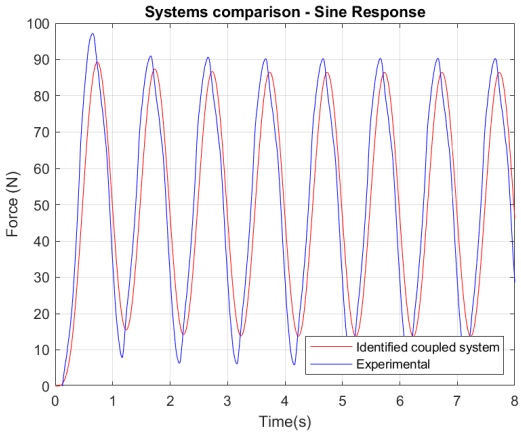

(d) PID

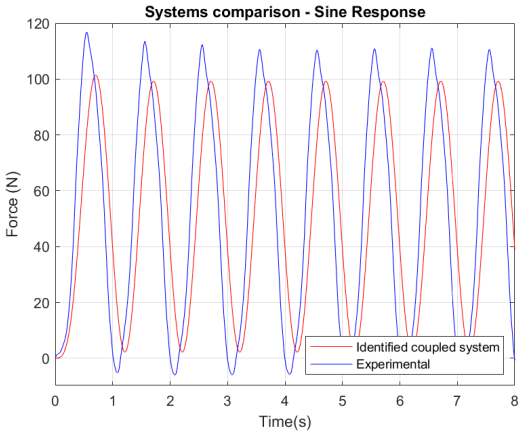

(e) PID + VC1

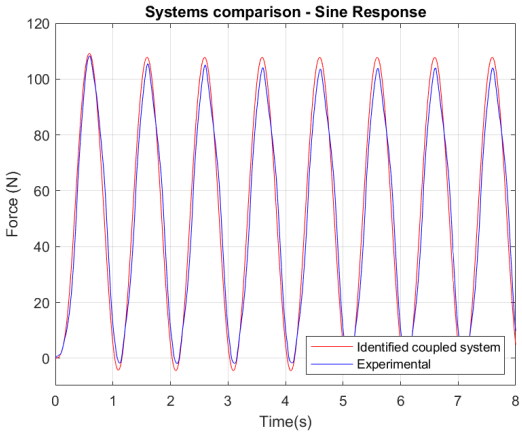

(f) PID + VC2

Figure 64 – Sine responses validation - Hydraulic cylinder


EESC • USP